ABSTRACT

Title of Dissertation: NOVEL STATISTICAL PATTERN RECOGNITION AND 3D MACHINE VISION TECHNOLOGIES FOR AUTOMATED FOOD QUALITY INSPECTION

Bin Zhu, Doctor of Philosophy, 2008

Dissertation Directed By: Professor Yang Tao, the Fischell Department of Bioengineering

Machine vision technologies have received a lot of attention for automated food quality inspection. This dissertation describes three techniques developed to improve the quality inspection of apple and poultry products.

First, a Gabor feature-based kernel principal component analysis (PCA) method was introduced by combining Gabor wavelet representation of apple images and the kernel PCA method for apple quality inspection using near-infrared (NIR) imaging. Gabor wavelet decomposition was employed to extract appropriate Gabor features of whole apple NIR images. Then, the kernel PCA method with polynomial kernels was applied in the Gabor feature space to handle nonlinear separable features. The experimental results showed the effectiveness of the Gabor-based kernel PCA

method. Using the proposed Gabor kernel PCA eliminated the need for local feature segmentation and also resolved the nonlinear separable problem in the Gabor feature space. An overall 90.5% detection rate was achieved.

Second, a novel 3D-based apple near-infrared (NIR) data analysis strategy was utilized so that the apple stem-end/calyx could be identified, and hence differentiated from defects and normal tissue according to their different 3D shapes. Two automated 3D data processing approaches were developed in this research: 1) A 3D quadratic facet model fitting, which employed a small concave 3D patch to fit the 3D apple surface and the best fit could be found around stem-end/calyx area; and 2) A 3D shape enhanced transform (SET), which enhanced the apple stem-end/calyx area and made it easily detectable because of the 3D surface gradient difference between the stem-end/calyx and the apple surface. An overall 92.6% accuracy was achieved.

Third, high resolution on-line laser 3D imaging was investigated for improving the 3D profile recovery for thickness compensation purposes. Parallel processing and memory management were also considered to improve the processing speed of the detection system. Multiple-lane coverage was fulfilled such that a wider conveyor could be used and overall throughput would be increased. To further improve the detection performance of the dual X-ray and laser imaging system, a dynamic thresholding approach was introduced to suppress the errors and noise involved by the imaging system. Unlike the traditional single threshold method, dynamic thresholding monitored the responses of the region of interest under a set of

thresholds to determine the true physical contaminants, making it more tolerant to the noise than the single threshold method. An overall 98.6% detection rate was achieved.

# NOVEL STATISTICAL PATTERN RECOGNITION AND 3D MACHINE VISION TECHNOLOGIES FOR AUTOMATED FOOD QUALITY INSPECTION

By

BIN ZHU

Dissertation submitted to the Faculty of the Graduate School of the
University of Maryland, College Park, in partial fulfillment
of the requirements for the degree of
Doctor of Philosophy
2008

Advisory Committee:
Professor Yang Tao, Chair
Professor Nam Sun Wang
Professor Adel Shirmohammadi
Professor Hubert Montas
Professor Fredrick W. Wheaton

# Acknowledgements

My deepest gratitude goes to my advisor, Dr. Yang Tao, for his guidance during my research and study at University of Maryland. His perpetual energy and enthusiasm in research motivated me to overcome many challenges during my Ph.D. research. His patience and thoughtfulness also made research life smooth and rewarding for me.

I wish to express my warm and sincere thanks to my committee members: Dr. Adel Shirmohammadi, Dr. Fredrick Wheaton, Dr. Hubert Montas, and Dr. Nam Sun Wang for their invaluable guidance and fruitful discussions.

My special thanks go to Ms. Abby Vogel, a really good friend, who helped me a lot to improve my English.

All my lab buddies at the Bio-imaging and machine vision laboratory made it a convivial place to work. In particular, I would like to thank Fenghua Jin, Lei Qin, Hansong Jing, Xin Chen, Xuemei Cheng, Angela Vargas, and Gary Seibel for their friendship and support.

I owe my loving thanks to my wife Lu Jiang, my daughter Sophia, and my parents, because without their unconditional support and enduring love, finishing my thesis wouldn't have been possible.

# Table of Contents

# List of Tables

# List of Figures

# CHAPTER 1 INTRODUCTION

## *1.1 Background and Rationale*

Trillion dollars worth of food products (Plunkett Research Ltd., 2007), including 9.9 billion pounds of apples and 55.2 billion pounds of poultry (USDA, 2007a & b), were consumed last year in the United States. Figure 1 shows the annual consumption of the major fresh fruits in the U.S., among which apples are ranked third. Similarly, the annual consumption of meat products is shown in Figure 2 with poultry meat ranked first. It is important for the food industry to ensure that all food products are effectively and efficiently inspected and processed to meet the stringent federal standards so that safe foods are sold to consumers. For years, machine vision technology has played an important role in the food industry by transforming the traditional labor-intensive manual inspection to automated on-line processing.

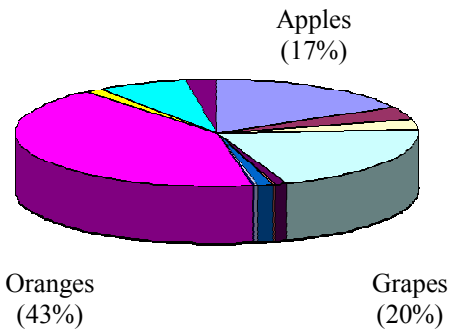


**Figure 1. Annual consumption of fresh fruits in the U.S.**

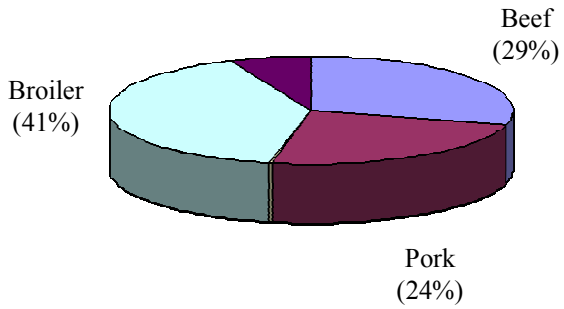


**Figure 2. Annual consumption of meat products in the U.S.**

Automated inspection of apple quality involves computer recognition of blemished apples based on geometric or statistical features derived from images of the fruit. Although pattern recognition techniques are widely used to detect apple defects, most current approaches are based on local information and need local feature segmentation. However, local feature extraction itself remains a very challenging problem in image processing. To overcome this problem, a global feature-based approach seems promising because it eliminates the need for local feature segmentation, and hence improves the effectiveness of the on-line apple sorting machine.

In machine vision-based automated apple grading and sorting systems, it is important to identify apple stem-ends and calyxes in apple images because they often exhibit similar patterns and intensity values to the defects and result in false positives during defect sorting. In addition, stem-end/calyx identification is necessary for estimating the apple firmness, because the location of the stem-end and calyx must be known if an efficient firmness measurement device is to be perfected (Throop, et al., 2001). Currently, 2D near-infrared (NIR) imaging technology is often used to detect apple

defects based on the difference in image intensity of defects from the normal apple tissues. However, the difficulty in accurately differentiating apple stem-ends/calyxes from the true defects due to their similar 2D NIR image patterns presents a major technical challenge to the successful application of this machine vision technology. Although 2D-based information seems insufficient, apple stem-ends and calyxes have special 3D characteristics including bowl-shaped concaves, making the 3D-based analysis a feasible approach for automated apple stem-end/calyx identification.

In the poultry industry, physical contaminants including bone fragments in fillets, metal chips and some other foreign materials are of major concern for the processors because serious health problems can be caused by accidentally swallowing them. Traditional X-ray imaging techniques are often employed to identify foreign contaminants in chicken fillets. However, the uneven thickness of the chicken meat presents a major challenge to accurately identify the physical contaminants by X-ray imaging alone. A combined X-ray and laser range imaging system has proved to be effective because the uneven thickness problem can be eliminated by the laser imaging modality. On the other hand, the throughput as well as the accuracy still needs to be further improved in order to build a viable machine for the real on-line applications.

## *1.2 Objectives*

The general objective of this study is to develop new pattern recognition and machine vision-based technologies for automated food quality inspection, especially for apples and poultry. The proposed approaches should be able to overcome the obstacles

mentioned above and/or to improve the performance of current system/technology. The specific objectives of this research are:

1) To develop a global feature-based apple automated inspection system that can eliminate the conventional local feature extraction during the apple defect detection, and hence improve both the efficiency and effectiveness of the system. The non-linear classification approach will be also explored in order to tackle the complexity of the problems.

2) To develop an apple NIR imaging system through 3D surface reconstruction and analysis for automated apple stem-end/calyx identification. Sample testing will be followed to evaluate the performance of the proposed approach.

3) To develop an improved dual X-ray and laser imaging system including an expandable on-line laser 3D ranging imaging subsystem, and the dynamic thresholding strategy for suppressing the errors and noise produced by the imaging system.

## *1.3 Organization*

This dissertation is laid out in the following order. The literature review on related research areas will be given in Chapter 2. In Chapter 3, the automated machine vision systems for both apple and poultry quality inspection will be introduced. The research with detailed analyses according to the three objectives given above will be discussed

in Chapters 4, 5 and 6, respectively. The conclusion as well as the future work will be presented in Chapter 7.

# CHAPTER 2 LITERATURE REVIEW

## *2.1 Machine vision technologies in the food safety and quality inspection applications*

### 2.1.1 The impact of food safety and quality research to human society

According to the U.S. Department of Agriculture (USDA, 2002), the average American consumes about 46 more pounds of poultry per year than they did in the 1970s, while fruit consumption has risen by 20% since the 1970s. As a result, food safety and quality inspection remains one of the major public health challenges in today's world. Although the food supply in the United States is one of the safest in the world, the U. S. Centers for Disease Control and Prevention (CDC, 2008) still estimates that "76 million people get sick, more than 300,000 are hospitalized, and 5,000 Americans die each year from foodborne illness." In addition to public health, food safety and quality also have large impacts on the economy. Researchers (Hayes et al., 1995; Baker, 1999) found that consumers would be willing to pay more for food with lower risks of disease and lower pesticide residues. Food quality and safety research is required to ensure such high quality food. In addition, to meet the aforementioned demand from the consumers, food industries must pay more and more attention to food safety and quality inspection in order to achieve better customer satisfaction and hence better profits for their business. Today's trend in the food industry for large-scale, global-based food production, preparation, processing

and distribution requires a more strict food safety and quality inspection system to ensure a safer global food supply (WHO, 2008).

### 2.1.2 The machine vision technologies in the food safety area

As one of the most widely used imaging technologies, automated machine vision has recently received more attention in automated food quality and safety inspection applications. Machine vision technologies have many unique characteristics, making them capable of obtaining otherwise unavailable, yet valuable, information from the product, and hence ideal tools for food safety and quality research. The advantages of machine vision technologies include:

*High accuracy* --- Due to the rapid development of optical and mechanical engineering, it is possible for food engineers to build a machine vision system with robustness, high noise resistance, and good signal sensitivity, properties which ensure high accuracy of the system.

*High resolution* --- A state-of-the-art machine vision system is capable of measuring products on the micro-, and even nano-scales. With such high resolution, many invisible clues become apparent.

*High reliability* --- Unlike manual operation systems, which usually suffer from operational variability due to the physical situation and psychological factors, modern machine vision systems have advantages of consistency and less variability. In addition, such systems typically have non-contact detection components, generating minimal wear and tear to those delicate parts, and hence further improving the system's reliability.

*High flexibility* --- A well-designed machine vision system can work smoothly under many harsh environmental conditions such as high humidity, low/high temperatures, and frequent high pressure water jet wash down.

*Cost effectiveness* --- According to Moore's Law, "the number of transistors that can be inexpensively placed on an integrated circuit is increasing exponentially, doubling approximately every two years." (Moore, 1965) As the price of electronic and optical components dropping rapidly, the machine vision system will eventually become more and more cost effective. The cost of employing a machine vision system usually includes one time equipment purchase expense and limited operation and maintenance fees. Compared to the cost of hiring human inspectors consisting of salary, insurance and pension, etc., the advantage of using automated machine vision system is obvious.

The components included in a machine vision system depend on the application, the environment, the budget and sometimes, the availability. The diagram of a typical machine vision system is shown in Figure 3. The following common modules/elements can usually be found in a vision system:

*Image acquisition module* --- The image acquisition module is often composed of one or more analog/digital camera(s) as well as associated optics, such as lighting, filters, etc. Images of subjects to be inspected are generated by this module. Tremendous research efforts have been focused on the development of this module to improve the acquisition speed, suppress noise, extend the spectrum response range, etc.

*Image processing and analysis module* --- Images obtained during the image acquisition stage are further processed by the image processing module to extract the useful information from the input images for detection purposes. Enormous image processing and pattern recognition strategies are explored by researchers and engineers within this module to identify fine clues of potential safety threats. As an intensively studied area, image processing and analysis, which is like the brain of a human inspector, play key roles in the entire machine vision system.

*Rejection and/or visualization module* --- Once safety threats are found during image processing and analysis, a rejection module is required to physically identify defective samples from good ones. In addition, visualization of defective samples as well as associated statistics, such as detection rate, threat conditions, etc., are necessary to better assist human inspectors. A machine vision system can be considered fully automatic only if an auto-rejection module is included in the system.

*Control and synchronization module* --- Because multiple modules need to work together, a control system becomes necessary to synchronize all the working components within a machine vision system. A well-designed control and synchronization subsystem usually has the advantage of high processing efficiency, low component cost, operator friendliness, and improved detection performance.

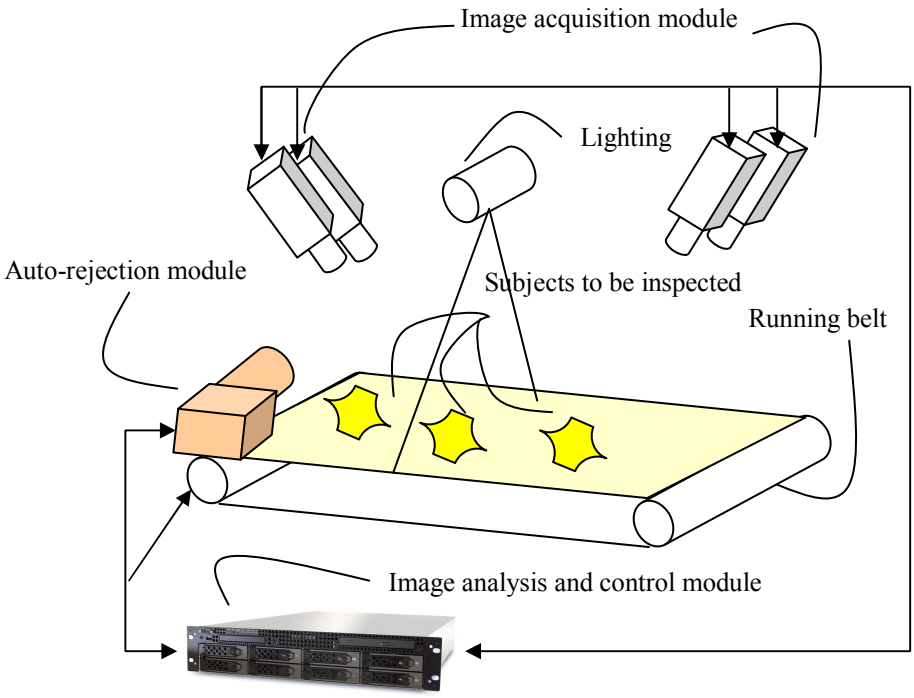


**Figure 3. A typical machine vision system**

### 2.1.3 Near-Infrared technology and its applications

The discovery of near-infrared energy is ascribed to Sir Frederick William Herschel (1738-1822) in the 19th century, who found the light radiation beyond what people know as the visible spectrum when he was trying to find a way to filter heat from a telescope (Herschel, 1800). However, the instruments and technologies using NIR spectroscopy were not well developed until the 1960s with the work of Karl Norris (1964) of the Agricultural Research Service (ARS) at the U.S. Department of Agriculture (USDA). From then on, NIR spectroscopy became well accepted and expanded into many research areas other than agriculture, such as remote sensing, industrial detection, chemical engineering, process control, etc. (Barton, 2002).

NIR spectroscopy is composed of molecular overtone and combination vibrations. Hooke's law is typically used to model the fundamental vibrations for diatomic molecules as the simple two-body harmonic oscillator. The key equation of Hooke's law is given as:

$$v = \frac{1}{2\pi c}\sqrt{\frac{k(m_1 + m_2)}{m_1 m_2}} \tag{2.1}$$

where $v$ is the vibration frequency, $c$ is the speed of light, $k$ is the force constant, and $m_1/m_2$ represents the mass of each molecule. In reality, NIR is mainly due to the combination and overtone bands that are caused by anharmonistic variations within molecules. Such anharmonicity usually increases as the vibration becomes stronger. An example of principle fundamental vibrations within water molecules is shown in Figure 4 (Barton, 2004). Other molecules may have more complicated fundamental vibrations such as rocking, wagging, twisting, etc.

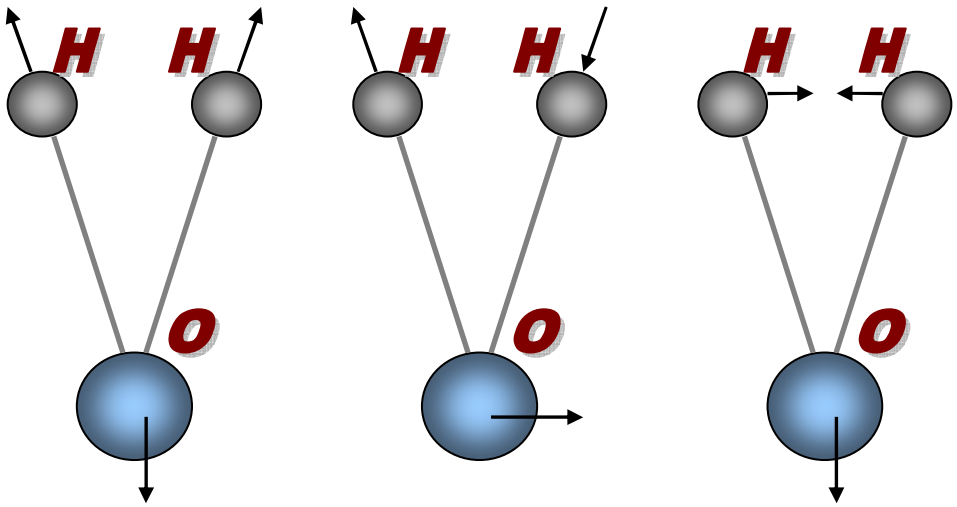


**Figure 4. Principle fundamental vibrations within water molecules**

Because of the band combination effects found in the NIR, Hooke's law is insufficient to describe the NIR phenomenon. To better understand NIR spectroscopy, a semiclassical interpretation based on the original contributions of James Franck (1926) was established. The Franck-Condon principle states that during an electronic transition, a change from one vibrational energy level to another will be more likely to happen if the two vibrational wave functions overlap more significantly, in other words at their minimal nuclear kinetic energies (Wikipedia, 2008a).

In the electromagnetic spectrum, the wavelength of the infrared spectrum is longer than the visible light, ranging from 700 nm to 1 mm. Among the entire infrared spectrum, NIR has unique characteristics and has been widely adopted in many research areas. In astronomy, NIR spectroscopy is used to study the atmospheres of cool stars to analyze the star's spectral type, to investigate molecules in molecular clouds, and to understand the star formation, etc. For industrial applications, NIR is capable of detecting defects, analyzing components, and so on. In the medical area, NIR is employed to determine oxygen and sugar levels in the blood, to assess brain function, to detect skin cancer, etc. In remote sensing, NIR is utilized to investigate soil, plants and environmental factors (Wikipedia, 2008b).

Because most NIR spectra can be explained by assigning bands to combinations and/or overtones of molecular fundamental vibrations involving hydrogenic stretching modes and the hydrogen-based bonds, such as C-H, O-H, etc., are the most important components found in organic molecules, NIR spectroscopy becomes the

ideal tool for the food quality and safety applications. In the quality evaluation of meat and poultry products, Park, et al. (2001) used the NIR reflectance spectra ranging from 1,100 to 2,498 nm with principle component regression to predict beef tenderness and Park, et al. (2008) employed NIR spectroscopy to evaluate the freshness of pork loin. In their study, the NIR absorbance of 0.95-1.65 nm was assessed. The statistic models, such as partial least square regression and principal component regression, were also used to analyze the spectra data. Prieto, et al. (2008) applied NIR reflectance spectroscopy (1,100-2,500 nm) to discriminate between adult steer and young cattle ground meat. Chao, et al. (2003) combined NIR and the visible spectra to analyze the difference among wholesome, septicemia, and cadaver chicken samples. Their in-depth study of NIR/visible spectra showed that chicken samples can be differentiated more finely compared to the traditional methods. With the help of principal components and a linear discriminant function, high quality performance can be achieved. The fusion of NIR and visible spectra was also utilized by Windham, et al. (2003) to evaluate chicken carcasses. The spectrum ranging from 400 nm to 950 nm was considered to detect possible fecal contaminants on chicken skin. In the quality assessment of fresh fruit products, Wen and Tao (2000) developed a novel dual NIR/mid-infrared (MIR) system. NIR imaging was used to detect defects on the apple surface or subsurface, while MIR was employed at the same time to extract apple stem-end/calyx information. By combining MIR imaging, the false positive rate of the detection system was significantly reduced. Aleixos, et al. (2002) developed a multispectral imaging system capable of obtaining both the visible and the NIR spectrum at the same time. With the help of multispectral imaging and

parallel processing, the aforementioned system could inspect the size, color and surface defects of citrus more efficiently than traditional devices. Lu (2001) studied NIR reflectance spectroscopy ranging from 800 nm to 1700 nm for the purpose of estimating the firmness and sugar content of sweet cherries. The partial least square-based statistical models were also introduced to do the prediction. Nagata, et al. (2006) detected compression bruises in Akihime strawberries using NIR hyperspectral imaging. NIR spectra ranging from 650 nm to 1000 nm at 5 nm wavelength intervals were evaluated, and the optimal wavelengths of 825 nm and 980 nm were identified using stepwise linear discriminant analysis. Three classification approaches (linear discriminant analysis, normalized difference and artificial neural network) were further studied for the purpose of automated bruise detection. Other than quality inspection research in the meat and fruit areas, NIR technologies are also extensively used for seafood (Lin, et al., 2003), vegetables (Pedroa, et al., 2007), grains (Sivakumar, et al., 2007), and milk products (Kawasaki, et al., 2008).

### 2.1.4 X-ray technology and its applications

In 1895, when Wilhelm Conrad Röntgen was investigating the external effects from the various types of vacuum tube equipment, he became the first person to detect electromagnetic radiation in a wavelength range from 10 nm to 0.01 nm, known today as X-rays or Röntgen rays. This great discovery earned Dr. Röntgen the first Nobel Prize in Physics in 1901 (Wikipedia, 2008c).

A typical X-ray generator is made with a vacuum tube. An example of a water cooled X-ray tube is illustrated in Figure 5 (Wikipedia, 2008d) where K is the cathode, A is

the anode, C is the water cooling system with continuous water flow $W_{in}$ and $W_{out}$, $U_h$ is cathode heater voltage, and $U_a$ is anode voltage.

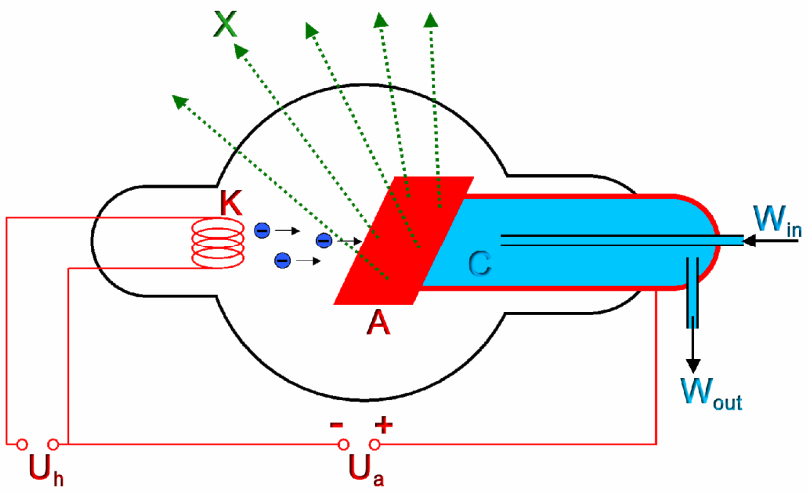


**Figure 5. A classic water cooled X-ray tube**

An X-ray is generated by the following steps:

1) The heated filament or cathode K in the vacuum tube emits electrons by thermionic emission;

2) The emitted electrons are then accelerated by the high anode voltage $U_a$. As a result, the continuous electron flow is established from cathode K to the anode A;

3) When the high energy, high speed electrons collide with a metal target A, X-ray radiation is produced.

Because excessive heat will be generated at the anode side, a cooling unit is necessary to keep the X-ray tube from overheating.

X-rays have shorter wavelengths (10 nm to 0.01 nm) and higher energy compared to the visible light spectrum. Because of its high energy, an X-ray can penetrate many

objects in its path, making it a unique imaging technology to investigate the internal structure of substances. When X-rays pass through an object, their behavior can be described by the following equations:

$$I = I_0 e^{-\mu d} \tag{2.2}$$

where $I_0$ is the incident X-ray photon intensity, $I$ is the transmitted X-ray photon intensity, $\mu$ is the attenuation coefficient, and $d$ is the thickness of the object. The attenuation coefficient can be further expressed as:

$$\mu = \varepsilon\rho \tag{2.3}$$

where $\varepsilon$ is the mass attenuation coefficient and $\rho$ is the density of the object. In general, $\varepsilon$ can be considered as a constant for different materials, and is dependent on incident X-ray energy level. If an object has multiple $n$ components, equation (2.2) can be further illustrated as:

$$I = I_0 e^{-\sum_{i=1}^{n} \varepsilon\rho_i d} \tag{2.4}$$

From equation (2.4), it can be seen that X-ray attenuation is mainly dependent on two major factors: density and thickness of the object.

As one of the most important discoveries in the human history, X-ray technology has been widely used in many areas. The typical applications of X-ray imaging technologies are given in Table 1 (Wikipedia, 2008e).

**Table 1. Typical applications of X-ray technologies**

| Imaging method | Application |
|---|---|
| X-ray diffraction | X-ray crystallography |
| X-ray emission | X-ray astronomy |
| X-ray penetration at low energy level | X-ray microscopic analysis |
| X-ray emission | X-ray fluorescence |
| X-ray penetration at normal or high energy level | Industrial radiography |
| X-ray penetration at normal energy level | Homeland security |

In X-ray crystallography, X-ray scattering is utilized to reveal the internal 3D structure, atom positions and chemical bonds of a crystal. This technology is widely used in chemistry and material science. It is known today that many celestial objects having extreme high temperature generate X-ray radiation. In order to study such celestial objects, X-ray imaging becomes one of the necessary tools in astronomy. X-ray microscopic analysis is similar to traditional X-ray imaging, and the only differences are that X-ray microscopic analysis use low energy X-ray penetration to investigate small objects. X-ray fluorescence utilizes the emission of characteristic X-rays to study the physical or chemical components of materials. Since different elements give different characteristic X-ray emission, X-ray fluorescence becomes an ideal tool for the elemental analysis, and hence has been widely used in geochemistry, archaeology, etc. Industrial detection and homeland security are the two well-known

X-ray applications. Both of them use X-ray transmission imaging to examine the internal structure of objects and reveal possible defects, contaminants, hazard materials, etc. (Wikipedia, 2008e).

Because of its capability of uncovering internal information of the objects, X-rays are also one of the most studied technologies in the food quality and safety inspection area. In the quality evaluation of meat and poultry products, Müller, et al. (2005) developed an X-ray device to analyze the fat content of ground meat. The comparison between their proposed method and the ground truth showed effectiveness of X-ray imaging based meat fat content analysis. Kröger, et al. (2006) confirmed the correlation between preprocessed dual X-ray images and meat tenderness. Their studies showed that dual X-ray imaging was suitable for meat tenderness estimation. However, more detailed analysis on meat properties as well as X-ray imaging technologies was suggested. McFarlane, et al. (2003) utilized X-ray backscatter to detect near-surface bone fragments in chicken meat. Three measurement strategies were employed according to the different energy windows of backscattered X-rays. Backscattered and transmitted X-ray images were compared to show the effectiveness of the proposed method. In the quality assessment of fresh fruit products, Jiang, et al. (2008) used an X-ray imaging system to identify insect infestation for imported fruit inspection. Two image processing algorithms were developed – adaptive image segmentation and unsupervised thresholding – to accurately locate the insect infestation. Selected fresh fruits, such as citrus, peach, guava, etc., were tested under their proposed approaches. Alonso, et al. (2007) investigated the potential quarantine

treatment of clementine oranges against Mediterranean fruit flies by means of exposure to X-ray radiation. Compared to the traditional cold temperature treatment of fruit, their method showed no significant negative effect on fruit quality such as firmness, juice yield, maturity index, internal volatiles, deterioration index, etc. and hence demonstrated effectiveness for the proposed study. Lammertyn, et al. (2003) employed both X-ray computational tomography (CT) and magnetic resonance imaging (MRI) to evaluate the core breakdown in the Conference variety of pears. The relationship between time and core breakdown rate was studied, and a relatively consistent breakdown rate was found among different pears. In the quality evaluation of grain products, Kumar and Bal (2007) investigated the X-ray imaging for crack detection of unhulled rice grain. A Hough transform was employed to process the X-ray images and determine the cracks in the rice grain. Their research has the potential to improve the efficiency of crack detection in the grain industry. Haff and Slaughter (2004) established a high-resolution, low energy, real-time X-ray imaging system to inspect wheat infestation by the granary weevil. A fairly good recognition rate was achieved by their methods. Neethirajan, et al. (2007) evaluated the potential application of a soft X-ray system for sprouted wheat kernel detection. Fifty-five different X-ray image features were extracted and further classified by statistical and neural network algorithms. Other than raw food quality inspection, X-ray imaging technologies have also been used for processed food inspection. Chen, et al. (2008) utilized an X-ray imaging device to detect the contaminants embedded in food packages. Edge detection and edge-constrained region growing was applied to identify small contaminants such as bone fragments and metal silvers. Pournaras, et

al. (2008) applied X-ray microanalysis and electrochemical impedance spectroscopy to inspect metal can discoloration, lacquer adhesion failure and side seam steel corrosion in tin plated cans containing cooked octopus in brine.

### 2.1.5 3D imaging technology and its applications

3D imaging, also known as stereoscopic vision can be traced back to 1838, when Charles Wheatstone (1838) first stated "…the mind perceives an object of three-dimensions by means of the two dissimilar pictures projected by it on the two retina…." It is known that the ultimate goal of 3D imaging is to obtain depth information from objects. Tremendous research efforts have been applied to 3D imaging in order to achieve this goal. The general procedure of 3D imaging is demonstrated in Figure 6.

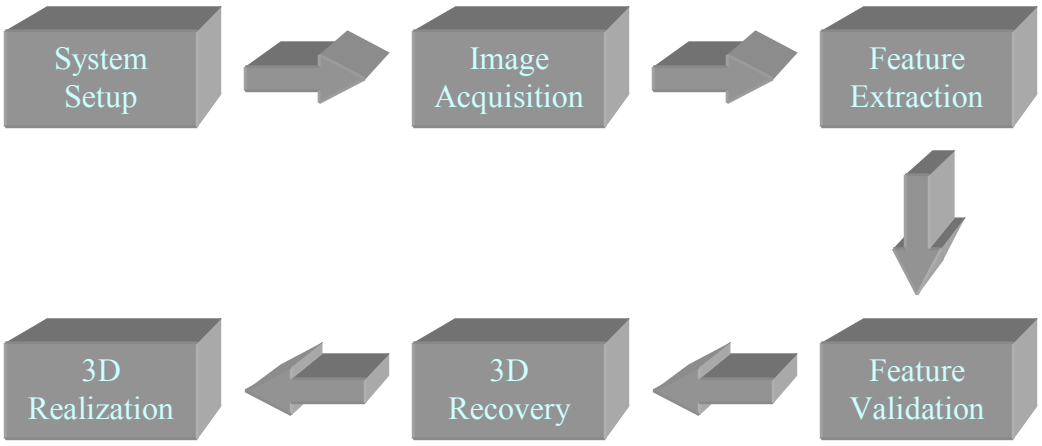


**Figure 6. General procedure of 3D imaging**

For a 3D imaging system setup, in order to get the best 3D imaging output, multiple factors are considered, such as lighting, camera position and scene background if the

environment is controllable. In the uncontrollable environment, only the camera may be adjusted, adding more complexity to the 3D imaging task. Once the system is set up, images can be obtained through data acquisition devices such as cameras. Two or more 2D images will be obtained through this step. In addition, the input images can be either still images or several image sequences that capture the motion of target objects. After image acquisition, feature points or regions of interest need to be extracted for further processing. Although there are tremendous feature extraction algorithms available for this task, extracted features often need to be verified in the feature verification step due to the noises or some other hard-to-control errors created during the image acquisition step. Once the features are validated, 3D information recovery can be achieved accordingly. 3D recovery is the key step during the whole procedure of 3D imaging. The quality of 3D imaging relies on the accuracy of 3D recovery. Given the recovered 3D information, 3D realization can be used for measurement, quality control, display, and other applications.

A simplified relationship between a real 3D scene and its 2D projection through the camera can be described by the following equation:

$$\begin{pmatrix} X_1 \\ X_2 \\ 1 \end{pmatrix} = T \begin{pmatrix} Y_1 \\ Y_2 \\ Y_3 \\ 1 \end{pmatrix}, \quad where \quad T = \begin{pmatrix} c_{11} & c_{12} & c_{13} & c_{14} \\ c_{21} & c_{22} & c_{23} & c_{24} \\ c_{31} & c_{32} & c_{33} & 1 \end{pmatrix} \tag{2.5}$$

From equation (2.5), it is clear that the translation from 3D coordinates $(Y_1, Y_2, Y_3)$ to 2D ones $(X_1, X_2)$ will cause loss of information. In other words, the transformation $T$ is not reversible. Therefore, 3D recovery is generally not a straightforward task, and

often needs reasonable approximation or additional information. Different 3D reconstruction approaches as well as their applications are listed in Table 2.

**Table 2. 3D reconstruction techniques and their applications**

| 3D Imaging method | Application |
|---|---|
| Shape from single view | Computer vision, Object recognition |
| Shape from multiple view | Computer vision, Object recognition |
| Structure from motion | Robotics, Stereo vision |
| Transform-based 3D reconstruction | Medical imaging, such as CT |
| Iterative 3D reconstruction | Medical imaging, such as PET |
| 3D range imaging | Industrial inspection, Quality control |

Shape from single view is a fast, but approximated 3D imaging approach. In such applications, one 2D image is sufficient to recover the 3D information of the object through reasonable assumptions and simplifications. This technology is widely used in computationally time demanding, but accuracy undemanding, applications such as industrial machine vision and object recognition and classification. To improve the shape from single view, more images can be employed to provide more 3D related information, also known as shape from multiple views. With the help of multiple images, the accuracy of 3D recovery data can be improved, but the computation time is increased as well. Other than recovering 3D information through still images,

structure from motion obtains the 3D structure of an object by analyzing its motion over time (Wikipedia, 2008f). The key issue of structure from motion is to accurately extract and track 2D features of the object, such as corner points, contours, edges, etc. In the medical imaging research areas, transform-based 3D reconstruction is widely used. Taking CT imaging as an example, multiple X-ray fan bean projections are first obtained around the human body. An algorithm called filtered back projection (FBP) is then employed to rebuild the cross-section images according to the aforementioned X-ray projections. When multiple reconstructed cross-section images are stacked together, the 3D volumetric data of the human body can be obtained. Iterative reconstruction is another 3D reconstruction approach through 2D projection data. It is also used in many medical imaging applications with less popularity than the FBP method. Compared to FBP, iterative reconstruction requires much more computation time and has less sensitivity to the noise. Range imaging can usually achieve the highest accuracy of recovered 3D data through carefully designed imaging devices, such as lasers. According to the different techniques, range imaging can be obtained through structured light, stereo triangulation, etc. Because of the accuracy of 3D range imaging, it is widely used in many industrial applications, such as defect detection, material inspection, surface evaluation, etc.

3D imaging technologies have been widely applied in many areas. The most well known 3D imagers are the human eyes, which recover 3D depth information from the environment through 2D images obtained by each eye. Wu and Ben-Arie (2007) presented a novel shape-from-shading method for human head 3D reconstruction.

They improved the initial surface estimation by hybrid principal component analysis (HPCA). The multiple-level optimization approach was then followed to recover the head 3D structure from 2D image. Cadavid and Abdel-Mottaleb (2007) developed two 3D ear recognition systems using both shape-from-shading and structure from motion techniques based on video sequence inputs. For the shape-from-shading approach, 3D ear structure was rebuilt by reflectance and illumination properties of the scene. For the structure-from-motion method, salient points were extracted and tracked as feature points. 3D ear data was then reconstructed using a factorization method. Woock, et al. (2007) utilized odometry data of a commercially available passenger car to perform the structure-from-motion task, and evaluated the accuracy of odometry data to see whether it was sufficient for the structure-from-motion application using only one camera. Zamyatin, et al. (2006) proposed a hybrid convolution algorithm for helical cone-beam CT reconstruction. They integrated many available algorithms, including ramp and Hilbert filters to improve the image quality of reconstructed CT images. A comparison between their method and the traditional one was also conducted, and showed the effectiveness of the proposed approach. In the food safety and quality research area, Lim and Barigou (2004) employed X-ray micro-computed tomography technology to analyze the 3D cellular microstructure of a number of food products, such as aerated chocolate, mousse, muffins, etc. They combined image analysis with stereological techniques to obtain multiple parameters related to cellular microstructure, such as cell size distribution, connectivity, voidage, etc. Daley, et al. (2005) introduced a stereo imaging system to accurately locate the cut points of interest on poultry breast meat. They obtained key

cut points from external reference points based on the anatomy of the bird. By improving the accuracy of meat cuts, the yield of the whole cutting system can be increased. Ávila, et al. (2007) performed 3D reconstruction on MRI to analyze the marbling and fat level of dry-cured Iberian pig products. Compared to the traditional marbling analysis, their method made a 3D visualization of fat distribution, and hence provided more information to the experts in food science to analyze marbling. Jiménez, et al. (2000) introduced a laser-based computer vision system for automated spherical fruit detection. Both range and reflectance images were acquired through an infrared laser range finder sensor. 3D position, radius and surface reflectivity of each spherical object could then be obtained using integrated image processing algorithms, and hence applied to an orange harvesting robot.

## *2.2 Automated Apple defects detection*

The rapid development in apple defects detection area can be seen in both hardware and software advances. On the hardware side, researchers have investigated almost all of the light spectra, from short to long wavelengths, and embedded them into different imaging devices for automated apple sorting and grading. Some of the systems such as Merlin® (Good Fruit Growers, 1993) have been successfully used in the industry. Shahin, et al. (2002) used an X-ray line scanner to distinguish different types of bruises on apple surfaces. Yang and Marchant (1996) employed a charge-coupled device (CCD) monochromatic video camera to identify apple defects such as bruises, insect bites and scabs. Leemans, et al. (1999) chose a three CCD color camera to segment apple defects based on a Bayesian classification process. Brown, et al. (1974) showed that in the NIR range between 700 and 2000 nm, there was less

reflectance in bruised areas than unbruised ones on apples. A wide range of approaches based on NIR apple images can be found in the literature (Tao and Wen, 1999; Wen and Tao, 1999; Li, et al., 2002). Furthermore, non-optical hardware-based approaches, such as MRI imaging (Zion, et al., 1995), as well as multi-modality imaging (Wen and Tao, 1998; Wen and Tao, 2000; Ariana, et al., 2006; Throop, et al., 1999) and hyperspectral imaging (Lu, 2003) techniques have also been explored by investigators to seek better automated apple processing. On the software side, tremendous computer-based pattern recognition approaches have been employed or developed for automated apple sorting applications.

On the imaging algorithm side, Leemans, et al. (1999) who applied a Bayesian classifier to segment defects of Jonagold apples based on the color images of bi-color apples. The Bayesian classifier worked well for most Jonagold apple defects; however, misclassification happened between russet and the transition area from ground to blush color. Leemans, et al. (2002) also proposed a six-step process for grading Golden Delicious and Jonagold apples. The proposed method achieved the classification rates of 78% and 72%, for Golden Delicious and Jonagold apples, respectively. However, identifying the apple stem-end and calyx from defects was still a problem because the stem-end/calyx often exhibited similar patterns as the apple defects, such as image intensity and 2D size. Yang and Marchant (1996) employed a flooding algorithm to coarsely segment out apple defects, followed by an active contour model to refine the segmentation so that the localization and size accuracy of the detected blemishes could be improved. However, the parameters used

in the active contour model varied with different kinds of apples as well as the defects, making it difficult to choose a general set of parameters for the active contour model. In addition, stem-ends and calyx could be misclassified as defects when the stem-ends and/or calyx were in view of acquisition cameras. Zion, et al. (1995) developed a fast computerized method to detect bruises from Magnetic resonance imaging (MRI) images of apples. A simple thresholding technique was used and combined with apple geometry information to distinguish between the apple vascular system and bruises. Although the internal 3D structure of an apple could be obtained with MRI imaging technology, the cost of both computation time and the system itself was very high. Nakano (1997) employed two neural networks to color grade Sun Fuji apples. A three-layered neural network with seven input nodes and six output nodes was used to evaluate whether the color of the apple surface was normal red or abnormal red with an overall accuracy about 95%. Another three-layered neural network with eleven input nodes and five output nodes was applied to grade the color of apples into five quality categories with an overall 70% recognition rate. However, the recognition rate for some quality classes was very low (<40%). Wen and Tao (1999) built a rule-based machine vision system to detect apple defects. A binary decision-tree-structured rule base was established by blob feature analysis. Although a relatively high recognition rate for good and defective apples could be achieved by choosing appropriate parameters, the misclassification between stem-end/calyx and defects still existed. Unay and Gosselin (2003) used principal component analysis (PCA) for quality grading of Jonagold apples. The performance of both direct PCA and separate PCA was compared and discussed, and the separate

PCA showed a higher recognition rate. Unay and Gosselin (2005) later applied an artificial neural network (ANN) to segment apple defects by pixel-wise processing. They also tested and compared five supervised classifiers, and the results showed that the adaboost and support vector machine (SVM) were the best two classifiers with above 90% recognition rates. Cheng, et al. (2004) proposed an integrated PCA-FLD (Fisher linear discriminant) method to maximize the representation and classification effects on the extracted feature bands of high-resolution hyperspectral images. An overall recognition rate of 93% was achieved. However, the testing features need to be segmented manually, which makes this approach currently unavailable for the automated industry application.

Although pattern recognition techniques are widely used in automated apple quality inspections, most approaches are based on local information and need local feature segmentation. However, local feature extraction itself remains a very challenging problem in image processing. Global feature based techniques, however, can be found in many other pattern analysis and computer vision fields (e.g., whole facial image based human face recognition (Turk and Pentland, 1991)).

## *2.3 Automated Apple stem-end/calyx identification*

As one of the most research-intensive areas in the food quality and safety, more and more attention has been paid to the apple quality inspection. However, differentiating the stem-end/calyx from true defects is still an open problem because the stem-ends and calyxes exhibit similar patterns and intensity values to the defects in apple images, which often causes an increase in false positives. In addition, stem-end/calyx

identification is necessary not only for on-line sorting and grading, but also for estimating the apple firmness, because the location of the stem-end and calyx must be known if an efficient firmness measurement device is to be perfected (Throop et al., 2001).

Approaches to detect the stem-ends/calyxes and defects have generally fallen into four categories. The first category is to develop a mechanical device in the conveyor system so that the stem-ends/calyxes can be prevented from showing in the camera view. Sarker and Wolfe (1985) designed an orientation device that makes the tomato rest on its stem or blossom end. Throop et al. (2001) tested two conveyors for automatic apple orientation. Both of the conveyors rotated apples into some stable position such that the locations of the stem-ends and calyxes could be determined mechanically. Recently, Bennedsen, et al. (2005) set up an experimental machine vision system to locate apple surface defects while eliminating other non-defect dark areas (such as stem-ends and calyxes) by rotating the apple in front of the camera and tracking the change of dark area among the images. The major drawback of mechanics based approach is the difficulties to design a device having both high detection accuracy and time efficiency.

The second detection category is focused on multi-modality/hyperspectral imaging techniques to differentiate the stem-ends/calyxes from defects. Wen and Tao (1998) proposed a fuzzy method to evaluate the performance of a dual-wavelength vision system for apple sorting. They (Wen and Tao, 2000) also built a dual-camera imaging

system, which incorporates a NIR and a MIR camera, to identify apple stem-ends and calyxes. Ariana, et al. (2006) introduced an integrated approach that employed multi-spectral imaging in reflectance and fluorescence modes to detect various defects on apples. Lu (2003) developed a NIR hyperspectral imaging system to detect both new and old bruises on apples. Although the techniques in this category provide more spectra information to the stem-end/calyx discrimination, and hence the detection accuracy can be improved, the high cost of the imaging device and/or the low image acquisition speed often prevent such approaches from being accepted by the industry.

The third approach can be categorized as 2D information based image processing and pattern recognition techniques. Leemans, et al. (1999) applied a Bayesian classifier to segment defects based on the color images. Unay and Gosselin (2004) developed a two-cascaded-classifier approach to localize stem-ends and calyxes of Jonagold apples. Penman (2001) utilized the blue linear light sources and a standard color video camera to identify the location of stem-end and calyx regions. Yang and Marchant (1996) employed a flooding algorithm followed by an active contour model to segment apple blemishes.

The fourth approach is based on semi-3D pattern recognition and analysis. Yang (1996) used structured lighting to detect stem-ends and calyxes. The limitation of such an approach is that when the stem-end or calyx is oriented to the direction of the stripe light source, the deformation of stripes are not obtainable. Tao (1996)

developed a spherical transform algorithm which converted a 3D problem to a 2D one by compensating for the intensity gradient on curved objects, such as apples.

Because of the similarity in appearance between apple stem-ends/calyxes and defects, it is generally difficult to distinguish them based on their 2D information such as shading and color. However, apple stem-ends and calyxes have special 3D characteristics including bowl-shaped concaves compared to apple defects and normal tissue, making the 3D based analysis a promising approach for the automated apple stem-end/calyx identification.

## *2.4 Automated bone fragments detection in deboned poultry fillets*

Imaging of transmitted X-rays, which is based on projecting ionizing radiation through a sample onto an image detector, has been widely used for physical contaminants detection in the food quality inspection. Ogawa, et al. (1998) applied a medical X-ray CT scanner as a non-destructive inspection method to detect the non-metallic materials embedded in various fluids and food materials. Lin, et al. (2005) employed X-ray imaging in quarantine inspection to prevent propagation of alien insect pests in imported fruits, such as apple, peach, and guava. Kotwaliwale, et al. (2007) developed and calibrated a soft X-ray imaging device for the purpose of biological materials quality determination.

For poultry quality inspection, one persistent problem is how to automatically detect bone fragments and some other foreign materials embedded in the poultry meat. X-ray imaging has been considered a good candidate for this problem due to its

capability of revealing the internal information of the target. However, the major challenge to the X-ray imaging, --- uneven thickness of the poultry meat --- still remains resolved. When the X-ray penetrates an uneven thickness, it is absorbed differently wherever the thickness varies or contaminants exist. As a result, the true contaminants become un-differentiable compared to those thick spots on the poultry meat, and hence, the false alarm rate turns out to be quite high. To overcome this difficulty, the simplest way is to merge the poultry meat in the water. Because it is believed that poultry meat has very similar density as water due to the significant water content in the meat, "water merging" approach can compensate the uneven thickness problem, and hence make the defects detectable under X-ray imaging. However, the simplest method doesn't mean the feasible one for real industrial application. One of the major disadvantages preventing acceptance of this method by the poultry industry is the sanitation problem. In other words, merging large amount of poultry meat in the water will inevitably cause microbial cross-contamination through water flow (Chen, 2003). Another thickness compensation strategy is to physically change the shape of poultry meat into the uniform one, such as press or compress the meat mechanically. A successful industrial application of this approach is ground meat defect detection (Hartman, 2001). However, for poultry products which natural shape needs to be preserved, this method seems inappropriate (Chen, 2003). Other than aforementioned non-imaging based techniques, Tao, et al. (2001) proposed an X-ray imaging based local-thresholding image segmentation approach to do the internal inspection of deboned poultry fillet. The uneven thickness issue was addressed by using the local threshold, which was adapted to uneven thickness

distribution, to segment the true bone fragments from the X-ray images. McFarlane, et al. (2003) utilized the backscattered X-ray radiation to detect the bone fragments of chicken meat. Their method was effective for the near-surface bone detection, however, deep embedded bone fragments will be a big challenge for such X-ray backscattering based approaches. Tao and his colleagues (Chen, et al., 2003; Tao and Ibarra, 2000; Jing, et al., 2003) developed a prototype system of dual X-ray and Laser imaging modalities. The laser range imaging was incorporated into the X-ray imaging to recover the accurate 3D thickness information of the chicken fillet. The thickness variation presented in the X-ray image was then compensated by aforementioned laser 3D information. Gleason, et al. (2002) designed a dual X-ray energy system to detect the bone fragments in the poultry meat. Other than X-ray imaging, Koch and Fowler (1998) invented a fluorescent imaging based bone fragments detection in deboned poultry meat. Two conveyors were employed in their system, one was used to carry poultry samples to be inspected, and another one was designed to press and flatten the meat to make the fluorescent lights underneath the poultry samples transformable. A video camera was also used to acquire the transmitted fluorescent image and hence detect bone fragments. Yoon, et al. (2006) introduced transmittance optical imaging at the visible and near-infrared (VIS/NIR) wavelength range to identify the bone fragments embedded in the chicken fillets. The sample thickness was mechanically controlled to 1 cm for the feasibility test. Multiple imaging modalities were used to ensure the best image quality could be obtained.

# CHAPTER 3 SYSTEM OVERVIEW

Two machine vision systems are introduced in this chapter: apple defect inspection system and automated poultry bone fragments and foreign materials detection system. The apple imaging system is a NIR imaging based equipment, and was used for automated apple defects detection and stem-end/calyx identification research in this dissertation. The poultry bone fragments detection system is a novel fused X-ray and Laser range imaging system, which was developed for the poultry safety in this study.

## *3.1 Automated apple quality inspection system*

The machine vision system (Figure 7) for apple quality inspection was previously developed in Bio-imaging and Machine Vision Lab. It consists of a computer-controlled image grabbing module, a NIR sensing system, a lighting chamber, and a conveyer system with variable speed controller. The NIR sensing system includes a monochromatic CCD camera with a C-mount lens of 16 mm focal length and a 700 nm long-pass interference filter. The NIR images are captured and analyzed by a host computer equipped with an image grabber. The lighting chamber is designed to provide uniform illumination for the infrared sensor (Cheng, et al., 2003). The chamber is made of lattice-patterned sheet metal, and the v-shaped interior surface of the chamber is painted flat white to provide diffuse light reflection and eliminate shadows (Tao, et al., 1995). In order to provide lighting, ten warm-white fluorescent lamps are mounted uniformly around a v-shaped surface right above the conveyor. The NIR imaging sensor is installed inside on the top center of the chamber. A roller conveyor belt is built to hold and move apples in up to six lanes. All apple samples

can be manually placed on the conveyer belt with a random orientation. The apples can be rotating and moving when they pass through the field of view of the NIR camera. The majority of the surface for each apple can be covered by the NIR camera during the apple rotation. A drive controller and speed controller are connected with an optical encoder that provides precise timing signals for both on-line mechanical and electrical synchronization (Cheng, 2004). The schematic of the whole imaging system is shown in Figure 8.

**Figure 7. A snapshot of NIR machine vision system for apple quality inspection and stem-end/calyx identification**

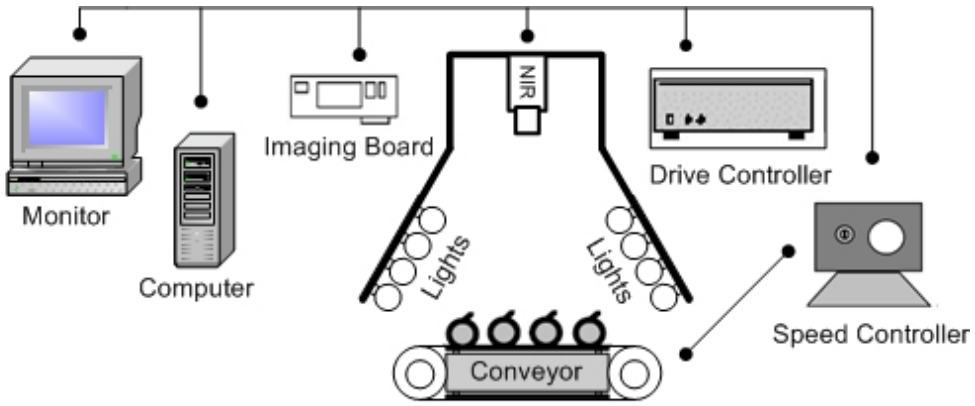


**Figure 8. A schematic representation of NIR machine vision system for apple quality inspection and stem-end/calyx identification**

## *3.2 Dual X-ray/Laser imaging detection system*

An overview of the X-ray and Laser synergetic imaging detection system is shown in Figure 9. The system is composed of one main cabinet and a controlled conveyer belt. The entire enclosure is made of wash-down food grade type-2 polish stainless steel with NEMA-4X (National Electrical Manufacturers Association, 2008) / IP66X (Wikipedia, 2008g) standard sealing, and capable of sustaining water jet up to $1.1 \times 10^4$ kPa. The stainless drum motor controlled conveyer belt has a variable speed setting ranging from 0 – 1.3 km/hr. A stainless steel framed 15" touch screen is located in the middle of front panel of the cabinet. The rejection sub-system is attached at one end of the conveyer belt. This sub-system is synchronized with the whole system to provide accurate rejection signals to a two-way air cylinder to perform the defected sample rejection.

**Figure 9. A snapshot of the x-ray and laser synergetic imaging detection system**

The internal structure of the imaging system is illustrated in Figure 10. Two laser sources are used to provide overlapped lines for the 3D range imaging. The fan beam X-ray is shot from the top. Two pairs of cameras are installed on the top of the cabinet. Each pair (same color) covers one lane (half width of the conveyor belt) and sees different side of testing sample. In this system, chicken fillets coming from a processing line are loaded on to the conveyer and scanned by the system for the X-ray intensity and 3D image. The system is extendable and for a multi-lane system, *2n* optical cameras will be used, where *n* can be one or two currently. The position of the optical devices are carefully arranged to minimize the effect of occlusion, and view areas of the neighboring cameras are overlapped for data integrity.

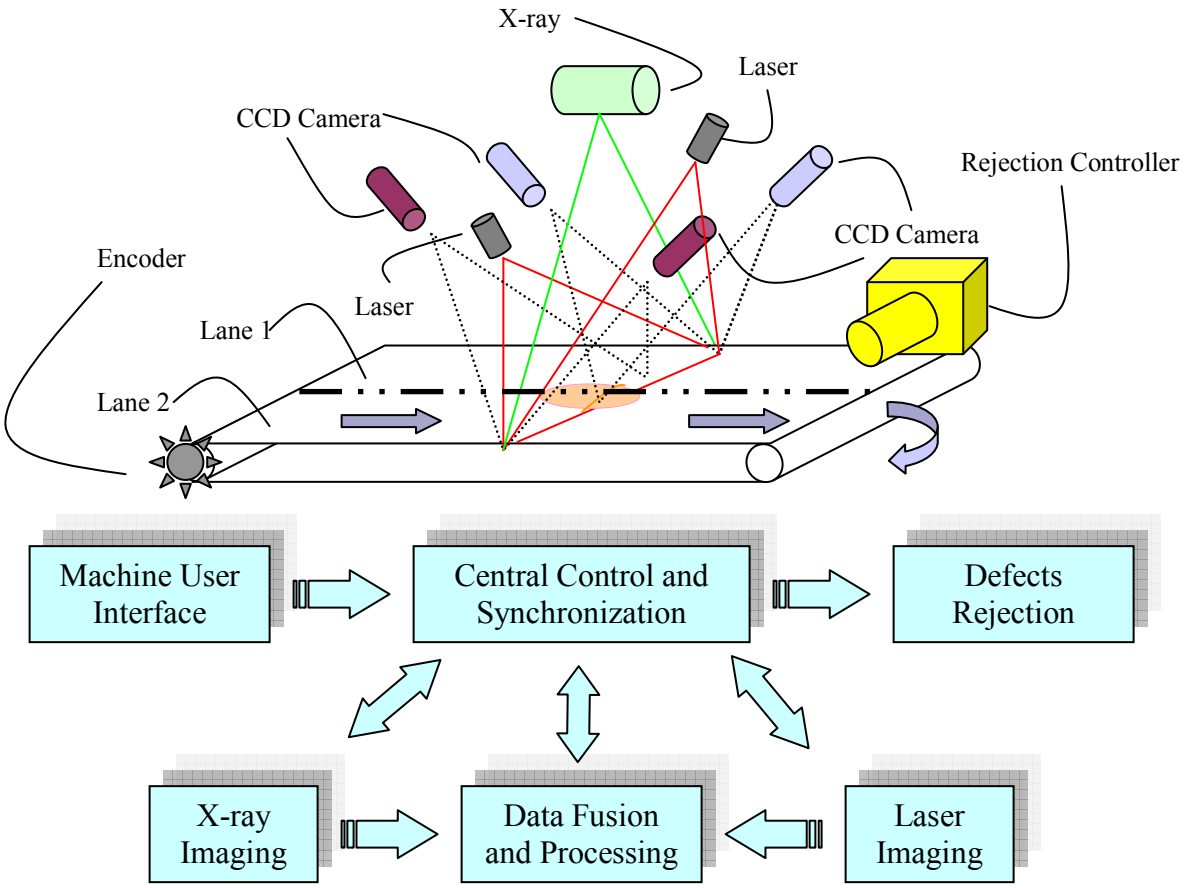


**Figure 10. A schematic representation of the x-ray and laser synergetic imaging detection system**

The general procedure of imaging system is schematically described in Figure 10. The imaging system is composed of six major modules: Machine User Interface (MUI), Central Control and Synchronization (CCS), Defects Rejection (DR), X-ray Imaging (XI), Laser imaging (LI), and Data Fusion and Processing (DFP). The machine operation is originated at the MUI where a human operator can issue the command, adjust settings, and monitor machine behavior. The role of CCS is to control and organize the overall data flow as well as the control signals among all the modules within the whole imaging system. In the XI and LI modules, both X-ray and Laser images are acquired through a high-speed imaging processor once the control

(acquisition) signals are dispatched by CCS. The acquired image data is then sent to CCS through high-speed data flow for the further processing. The DFP processes the image data sent by the CCS. Once the data processing work is done, the results will be sent back to the CCS. The CCS then sends the results and the control signal to the MUI and DR. The role of MUI is to display the results and related statistics on the touch screen, while the DR conducts the rejection mechanism which reject the defective samples according to the control signal sent by CCS. The conveyor direction of motion and running speed of the conveyor belt are also controlled by CCS. All the modules are perfectly controlled and synchronized by the CCS such that high resolution images can be acquired and processed without sacrificing the throughput (running speed) of the imaging system.

# CHAPTER 4 GABOR WAVELET-BASED APPLE QUALITY INSPECTION USING KERNEL PRINCIPAL COMPONENT ANALYSIS

## *4.1 Introduction*

Automated apple defects detection is an important issue to the apple industry. Solving this persistent problem will increase customer satisfaction and increase profits to the apple growers. The objective of this research was to introduce a global feature-based approach that would eliminate the need for image segmentation, and hence became a feasible method for automated high-speed industrial applications. A Gabor-based kernel Principle Component Analysis (PCA) method (Liu, 2004; Shen and Bai, 2004), which combined Gabor wavelet representation of the apple features and the kernel PCA, was used for apple quality inspection based on NIR images. In this Chapter, Gabor wavelet decomposition is introduced in section 4.2.2. In section 4.2.3, kernel PCA and Gabor-based kernel PCA are demonstrated in detail. For comparison purposes, Support vector machine (SVM) is introduced in section 4.2.4. The experimental results and comparisons between five different classification schemes are given in section 4.3 to show the effectiveness of the Gabor-based kernel PCA approach for apple quality inspection.

## *4.2 Materials and Methods*

### 4.2.1 Image acquisition

The dataset grabbed by the imaging system contained a total of 166 NIR Golden Delicious apple images, including ones with and without defects. The testing data was independently evaluated once the optimal parameters were obtained through training data. Apples were refrigerated and stored at 4 $^{0}$C before they were tested. The detailed composition of test data is listed in Table 3. Typical NIR apple images are shown in Figure 11. Numbers surrounding each NIR apple image reflect the actual image pixels.

**Table 3. The composition of Apple NIR dataset**

| | Good Apples | Blemished Apples | Total |
|---|---|---|---|
| Training Dataset | 20 | 20 | 40 |
| Testing Dataset | 58 | 68 | 126 |
| Total | 78 | 88 | 166 |

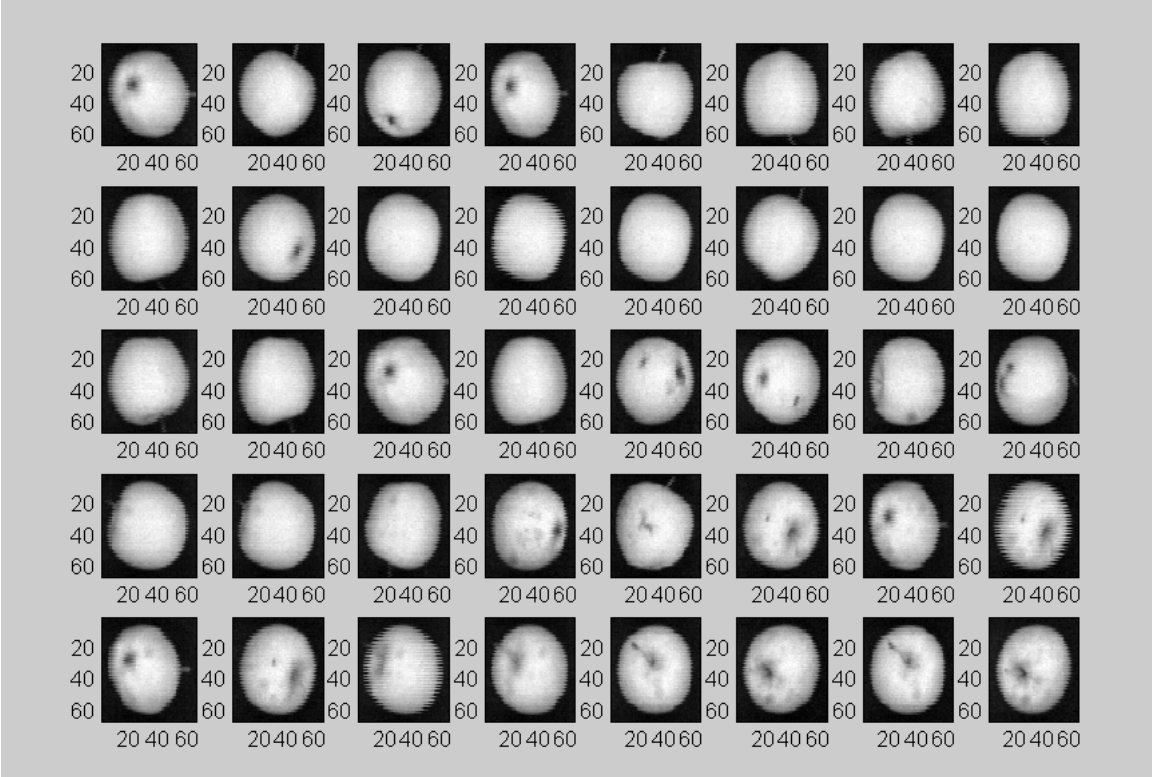

**Figure 11. Example of NIR golden delicious apple image dataset (The values around each apple refer to the number of pixels)**

### 4.2.2 Gabor-wavelet decomposition

Gabor wavelets have successfully modeled the response of brain cells in the visual cortex (Jones and Palmer, 1987) since they optimally represent the textural structure with different locations and orientations. Gabor-based wavelets (Lades, et al., 1993) come from a self-similar family generated from the mother wavelet under groups of translation, rotation and scaling transformations. It has the following general form:

$$\psi_{\vec{k}}(\vec{z}) = \frac{\vec{k}^2}{\sigma^2} e^{(-\vec{k}^2 \vec{z}^2 / 2\sigma^2)} [e^{i\vec{k}\vec{z}} - e^{-\sigma^2/2}] \qquad (4.1)$$

where $\vec{z} = (x, y)$ are the spatial coordinates. The two terms $e^{i\vec{k}\vec{z}}$ and $e^{-\sigma^2/2}$ are the oscillation and DC part of Gabor wavelets, respectively. Generally, $\sigma$ is equal to $2\pi$,

and if the parameter $\sigma$ becomes large enough, the DC term can be ignored (Lades, et al., 1993; Liu and Wechsler, 2002). The parameter $\vec{k}$ controls the wavelength and orientation of the wavelets and is given by:

$$\vec{k} = k_{p,q} = k_q e^{i\phi_p} \tag{4.2}$$

where $k_q = k_{\max} / f^q$, $\phi_p = \pi p / 8$, $k_{\max} = \frac{\pi}{2}$, $f = \sqrt{2}$, and $p \in \{0,...,7\}$ and $q \in \{0,...,4\}$ identify eight orientation directions and five space frequencies, respectively. Figure 12 shows the real part and magnitude of Gabor wavelet kernel under five scalings and eight orientations. (Gabor wavelet, 2008)

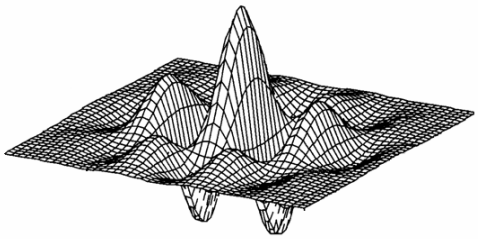

**(a)**

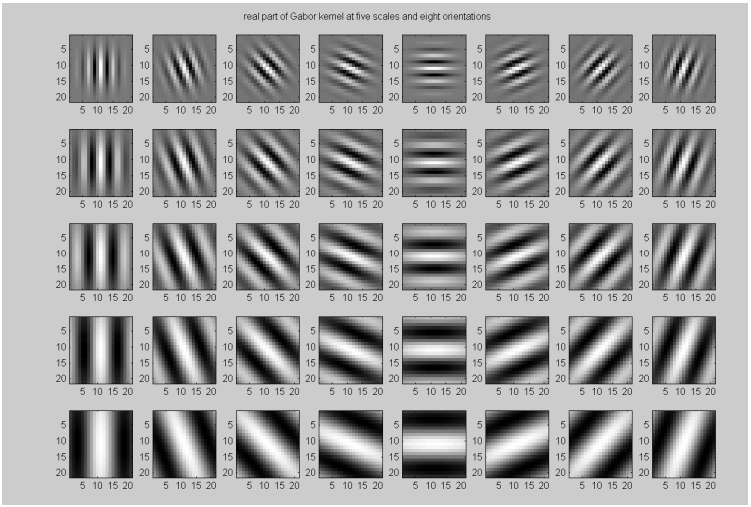


**(b)**

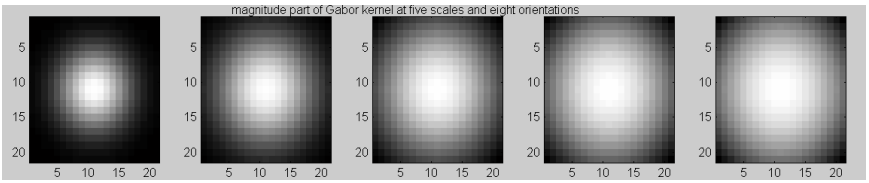


**(b)**

**Figure 12. Gabor wavelet kernels (a) A 3D view of Gabor wavelet. (b) Real part of Gabor wavelet kernel at 5 scales and 8 orientations. (c) Magnitude part of Gabor wavelet kernel at 5 scales and 8 orientations.**

The convolution of an image $I(x,y)$ and Gabor-wavelet $\psi_{\vec{k}}(x,y)$ can be expressed as:

$$F_{\vec{k}}(x,y) = I(x,y) * \psi_{\vec{k}}(x,y) \tag{4.3}$$

In the case of eight orientations and five space frequencies, the Gabor feature vector, $\Psi$, is given by (Liu and Wechsler, 2002):

$$\Psi = (F_{0,0}^t \; F_{0,1}^t \ldots F_{4,7}^t)^t \tag{4.4}$$

where $F_{p,q}$ is the column vector form of $F_{\vec{k}}$, $t$ is the transpose operator, and $\Psi$ is used as the discriminating features in the apple quality classification.

### 4.2.3 Gabor-based Kernel PCA

PCA (Pearson, 1901) has been widely used in many pattern recognition applications, such as face recognition (Turk and Pentland, 1991; Belhumeur, et al., 1997), and remote sensing (Corner, et al., 1999). In this research, PCA was used to define the best subspace such that a set of apple patterns could be sufficiently represented by

that subspace. In other words, the goal was to linearly project the input data onto a subspace that maximized the significant variation among the inputs.

Unlike the traditional PCA approach, where only linear projection is performed to seek a best mapping of the original dataset, the kernel PCA (Schölkopf, et al., 1998) relaxes the linear constraint, and allows arbitrary high-order projections among the input data from low-dimensional to high-dimensional mappings. Kernel PCA linearly represents the nonlinear problem by means of mapping the low-dimensional input space, which is usually nonlinear separable, into a linear separable high-dimensional feature space. More specifically, the underlying principle of kernel PCA is addressed by Cover's theorem (Haykin, 1999). The low- to high- dimensional mapping is defined implicitly by a so-called kernel function, which efficiently computes the inner product as a direct function of the input space. Without explicitly computing the mapping function, the kernel PCA becomes more computationally feasible (Shawe-Taylor and Cristianini, 2004).

Assume the sample set of input space is $\{u_i\}$, $i= 1, \ldots, N$, $u_i \in \Re^n$, and the mean of the sample set is zero. By a nonlinear mapping, $\Phi$, the input space can be mapped into another inner product space $\Gamma$ by:

$$\Phi : \Re^n \to \Gamma, \; u \to U. \tag{4.5}$$

The dataset in mapped feature space is $\{\Phi(u_1), \Phi(u_2), \Phi(u_3), \ldots \Phi(u_N)\}$ and the kernel function is defined as the inner product of the data in feature space:

$$K(u_i, u_j) = < \Phi(u_i), \Phi(u_j) > \tag{4.6}$$

The kernel matrix, $K \in \Re^{N \times N}$ is:

$$K_{ij} = < \Phi(u_i), \Phi(u_j) > \tag{4.7}$$

where $i, j \in \{1, ..., N\}$. Schölkopf, et al. (1998) proved that the PCA in the inner product feature space could be fulfilled by the equation:

$$N\lambda\alpha = K\alpha \tag{4.8}$$

where $K$ is positive semi-definite kernel matrix, $N$ is the number of samples, $\lambda$ is the eigenvalue and $\alpha$ is the corresponding eigenvector. Schölkopf, et al. (1998) also showed the projection of a test point, $\Phi(u_*)$, onto the eigenvectors $V$ in feature space $\Gamma$ could be expressed as:

$$< V, \Phi(u_*) > = \sum_{i=1}^{N} \alpha_i \ < \Phi(u_i), \Phi(u_*) > \tag{4.9}$$

From equations (4.7) and (4.9), the mapped pattern between input space and feature space only needs to be implicitly computed by the inner product.

In general, three kernel functions (Cortes and Vapnik, 1995), which allow computing of the value of the inner product in $\Gamma$ without carrying out the mapping $\Phi$, are frequently used in kernel classifiers. They are shown in Table 4. The basic idea of kernel PCA is illustrated in Figure 13 (Schölkopf, et al., 1998).

**Table 4. Frequently used kernel functions**

| Kernel Name | Kernel Equations |
|---|---|
| Polynomial Kernel | $k(x,y) =< x,\ y >^{d},\quad d \in R.$ |
| Gaussian Kernel | $k(x,y) = \exp(-\frac{\|x-y\|^2}{2\sigma^2}),\ \sigma > 0$ |
| Sigmoid Kernel | $k(x,y) = \tanh(\kappa < x,\ y > +\vartheta),\ \kappa > 0, \vartheta \geq 0$ |

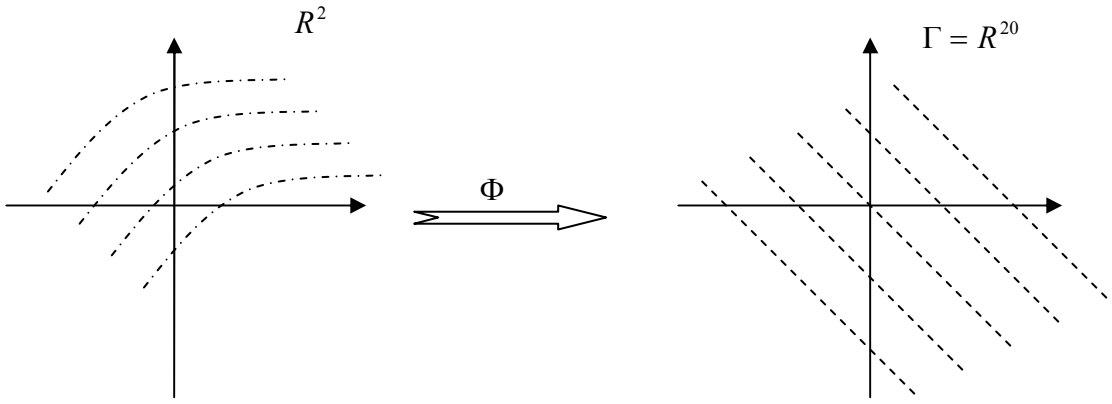


**Figure 13. Illustration of kernel PCA showing nonlinear mapping of the input space ($R^2$) into the $\Gamma$ space ($R^{20}$) with $\Phi$, and then implementing the linear PCA in space $\Gamma$.**

Gabor-based kernel PCA (Liu, 2004) is the combination of Gabor wavelet decomposition for the sample dataset and kernel PCA for pattern recognition. First, Gabor wavelet decomposition is applied to the sample dataset to obtain the Gabor features of the input data. Then the Gabor feature vector $\Psi$ is fed into the kernel PCA algorithm. In other words, the Gabor feature space is regarded as the input space of the kernel PCA. Through the kernel PCA, Gabor feature space is mapped to a high-dimensional feature space $\Gamma$, making the high dimensional features linearly

separable by PCA in that space. Finally, the nearest neighbor classifier is used in the high-dimensional space $\Gamma$, to differentiate quality of apples according to the Euclidean distance metric.

### 4.2.4 Support Vector Machine

SVM (Duda, et al., 2001) is another popular statistical learning algorithm in data mining. It has been widely applied in a large number of applications, such as object recognition (Guo, et al., 2000) and face detection (Osuna, et al., 1997). The key point of this approach is to find the optimal linear hyperplane that can not only properly divide the largest portion of data points, but also maximize the distance of each class from that hyperplane at the same time. Just like the kernel PCA, the input space in SVM can also be mapped into the high-dimensional feature space by kernel function such that the data in the high-dimensional feature space becomes linear separable. However, the classification criterion used in kernel PCA and SVM are different, which makes these two approaches distinctive. For comparison purposes, SVM is also tested in this research. The detection results among different classifiers are given in the next section.

## *4.3 Results and Discussions*

A total of 166 NIR Golden Delicious apple images were tested in the experiment. Typical Gabor features (5 scalings by 8 orientations) of a NIR apple image are illustrated in Figure 14. Seen from the figure, Gabor-wavelet decomposition captures different image information by means of combining different scaling and orientation factors. Given extracted Gabor features, it is important to find an optimal mapping

(kernel function) through Gabor feature space to a high dimensional space such that the classification performance in aforementioned high dimensional space can be maximized. For the proposed Gabor-KPCA approach, three typical kernel functions, e.g. Polynomial kernel, Gaussian kernel and Sigmoid kernel, were evaluated in the experiment. The relationship between recognition rate and different kernel functions is plotted in Figure 15.

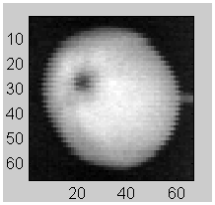


**(a)**

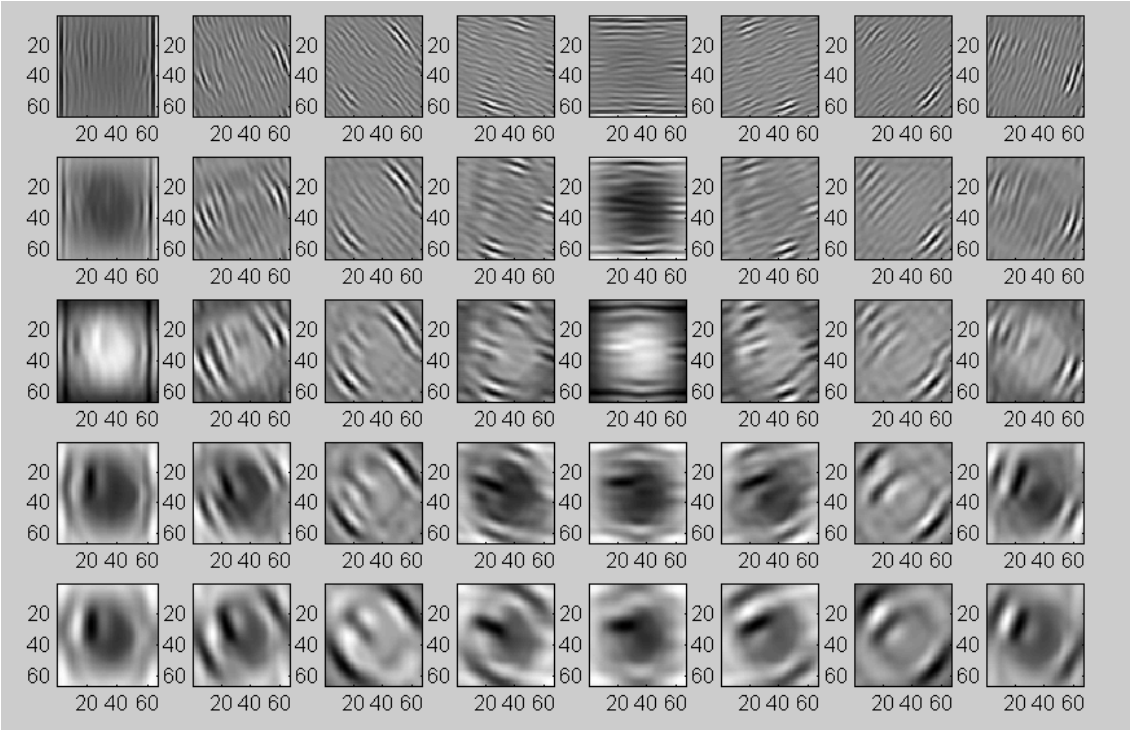


**(b)**

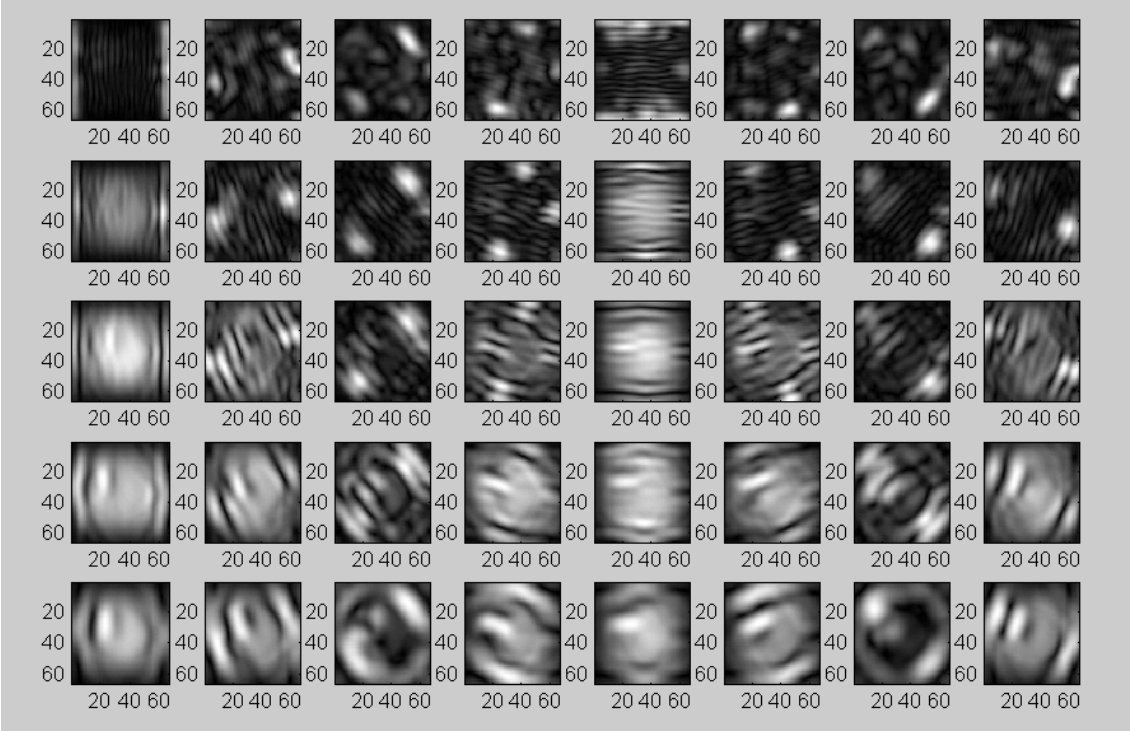

**(c)**

**Figure 14. Gabor wavelet decomposition for a NIR apple image (a) Original apple NIR image. (b) Real part of Gabor wavelet decomposition. (c) Magnitude of Gabor wavelet decomposition.**

As seen in Figure 15, the polynomial kernels have the best classification performance among all three kernel types. The recognition rate increases as the degree of freedom increases, and achieves its optimal by 90.5% when the degree of freedom equals 7. The experimental results demonstrate that the high order polynomial mapping from Gabor feature space makes the mapped data more linearly separable in the high dimensional space. In other words, the Gabor-KPCA method can linearly solve the nonlinear problem through a high order polynomial mapping. As a result, the polynomial kernel with $7^{th}$ order was chosen for proposed Gabor-KPCA approach. Table 5 shows the confusion matrix of Gabor-KPCA method.

**Table 5. Confusion matrix of proposed Gabor-KPCA method**

| True Labels | Estimated Labels | | Total |
|---|---|---|---|
| | Good Apple | Blemished Apple | |
| Good Apple | 50 | 8 | 58 |
| Blemished Apple | 4 | 64 | 68 |
| Total | 54 | 72 | 126 |

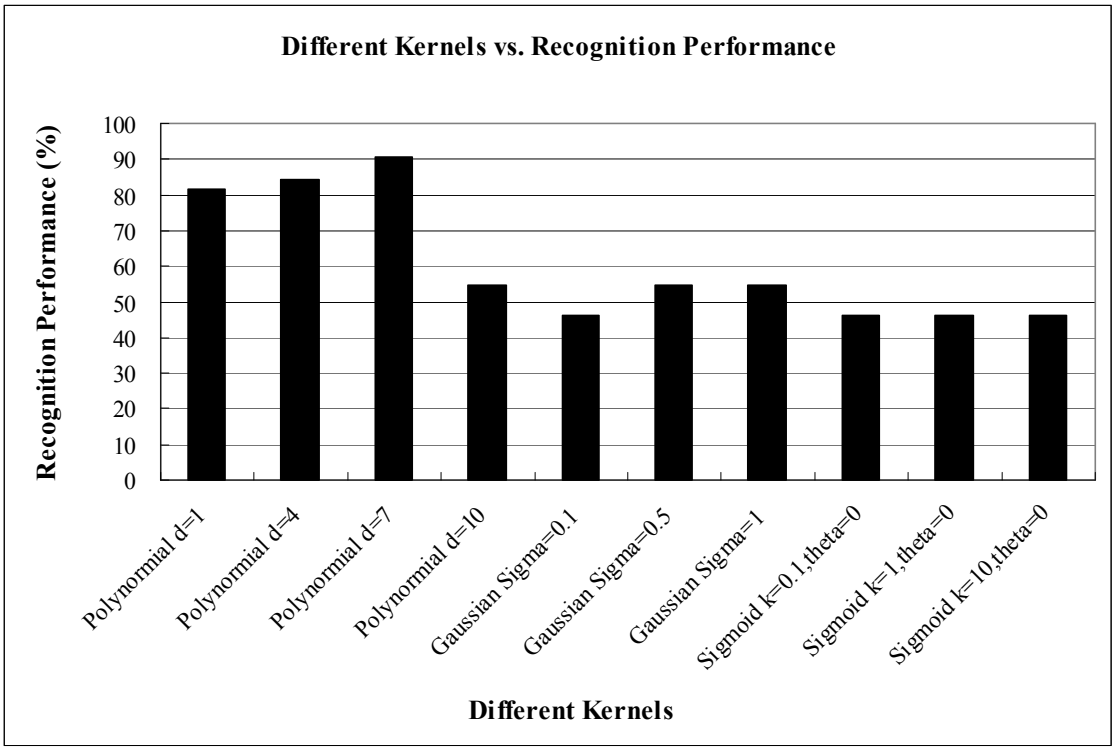


**Figure 15. The relationship between recognition rate and the typical kernel functions with different parameters**

To further evaluate the proposed Gabor-KPCA approach, the performances of five methods were assessed in the experiment: PCA, Gabor wavelet-based PCA, kernel PCA with polynomial kernels, Gabor based kernel PCA with polynomial kernels, and

SVM with polynomial kernels. A total of 40 NIR apple images were used as training samples, and 126 apple images were tested in this research. The dataset was divided into two categories: good or blemished. The recognition rates of each method are given in Table 6. The proposed Gabor-KPCA method had the highest recognition rate compared to other approaches. Note that the recognition rates of Gabor PCA and kernel PCA were lower than PCA, while the combination of them was higher. This shows that more information can be reserved (meaning better classification performance) through linear representation in original NIR image space rather than in the Gabor feature space. PCA had a higher recognition rate than kernel PCA, illustrating that the nonlinear mapping through the polynomial kernel function from the original input space (apple NIR image space), not the Gabor feature space, didn't make the mapped data more linear separable than the original inputs. This fact can also be found in SVM, since SVM has the same kernel function as kernel PCA. However, when Gabor feature space and the nonlinear mapping through the polynomial kernel function are combined together, the recognition performance can be significantly improved. In other words, although Gabor feature space reserves less information under linear representation than the original input space, when it is mapped to a high-dimensional space through the polynomial kernel function, the mapped space becomes linear separable.

**Table 6. Data sets and recognition rates**

| Approach | Recognition rate |
|---|---|
| Gabor-Kernel PCA | 90.5% |
| PCA * | 84.9% |
| SVM | 83.3% |
| Gabor PCA | 81.8% |
| Kernel PCA | 81.0% |

*** Note: Although both the recognition rate of individual Gabor PCA and kernel PCA are lower than PCA, the combination of them is higher.**

Both type I and type II errors (Lyman, 2001) were considered in the study to evaluate the performance of the proposed approach. Type I error was calculated as the number of misclassified samples (i.e. defected apple images) divided by the total number of samples, while type II error was computed as the number of false classified samples over the total number of samples. The error rates for good and blemished apples are given in Figure 16 and 17, respectively. For good apples, Gabor kernel PCA has the lowest type II error, and second lowest type I error. Although the type I error of the Gabor kernel PCA is slightly higher than PCA, the overall error rate of this approach is still the lowest. Note that PCA has the second highest type II error rate of 20.7%. The same phenomenon can be observed in the blemished apple category. The Gabor kernel PCA has the lowest type I error and second lowest type II error, but it has the best performance in terms of overall error rate. The average computational time is 19 ms/apple image under a moderate PC configuration, which includes a Intel Core Duo 2.0GHz CPU and 2.0 GB of RAM. According to the experimental results, the Gabor kernel PCA shows its feasibility to do the apple quality inspection without local feature segmentation.

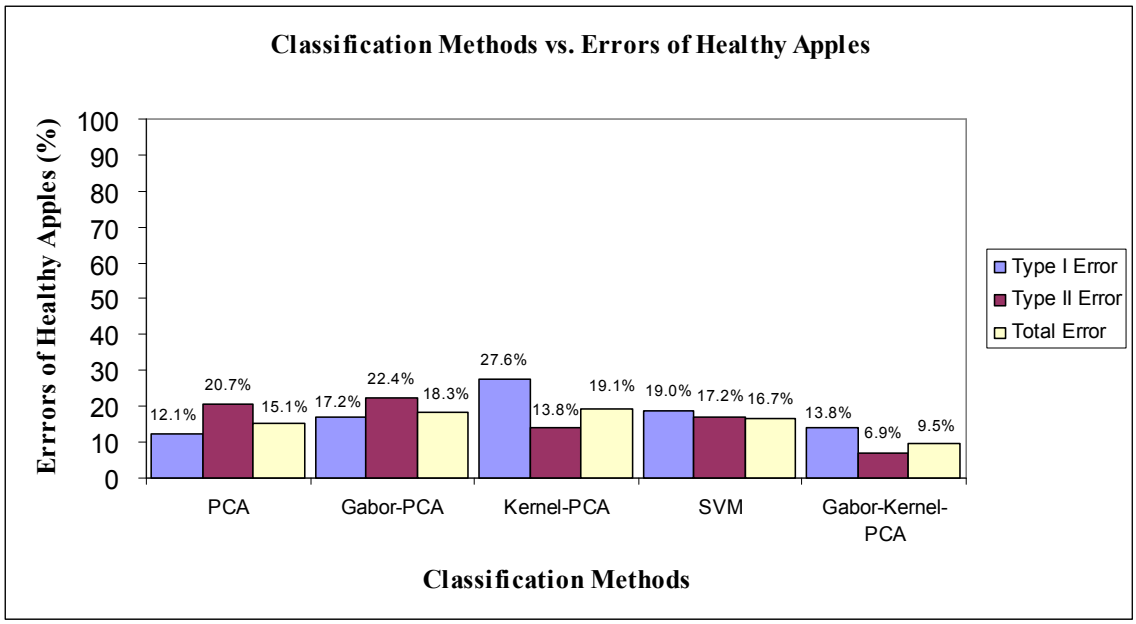


**Figure 16. Error rate for good apples based on five classification approaches**

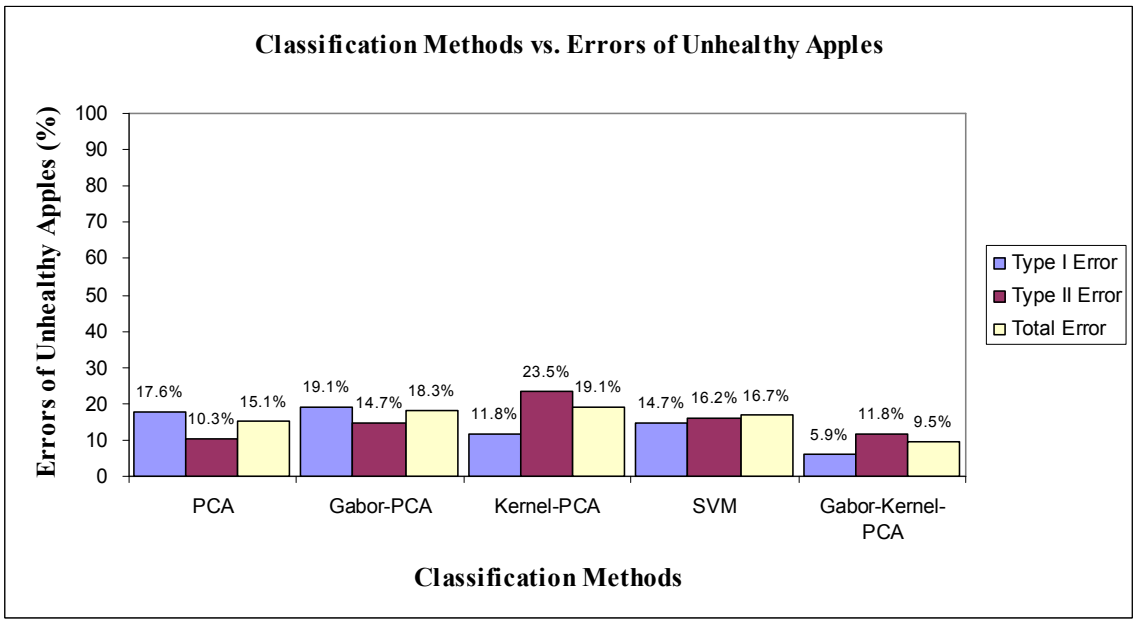


**Figure 17. Error rate for blemished apples based on five classification approaches**

As a summary, the basic procedure of proposed approach can be illustrated as the following three steps:

1) Gabor feature extraction using whole apple NIR image;

2) Data mapping from Gabor feature space to a high-dimensional space through the polynomial kernel function;

3) Linear representation using PCA and classification using nearest neighborhood approach.

## *4.4 Conclusions*

This Chapter introduced a Gabor feature-based kernel PCA approach to inspect the quality of apples. This approach showed many advantages. First, it eliminated the need of local feature segmentation by means of Gabor feature decomposition for the whole apple NIR images. It also sought a better high-dimensional space through the polynomial kernel function, which mapped Gabor feature space to high-dimensional space, and made the nonlinear separable problem in the Gabor feature space linear separable in that high-dimensional space. The comparison among five different classifiers was also conducted to evaluate the performance of those classifiers, and the experimental results showed that the proposed Gabor kernel PCA had the highest recognition rate among the five classifiers. Based on 166 NIR golden delicious apple images, an overall 90.5% detection rate was achieved with this method.

# CHAPTER 5 3D RECONSTRUCTION AND ANALYSIS FOR AUTOMATED APPLE STEM-END/CALYX IDENTIFICATION

## *5.1 Introduction*

As one of the most widely used imaging technologies, automated machine vision plays an important role in the apple industry by transforming the traditional apple-by-apple visual inspection to automated on-line sorting and grading. Currently most machine vision techniques used in apple automated processing are 2-D or 2½-D based approaches, which usually have difficulties to accurately identify apple stem-end/calyx on the surface. On the other hand, as one of the persistent problems, apple stem-end/calyx identification must be solved not only for the accurate defect inspection, but for efficient firmness measurement purposes.

To solve the aforementioned problem, a novel 3D based apple near-infrared (NIR) data analysis strategy was developed so that the apple stem-end/calyx could be identified, and hence differentiated from defect and normal tissue according to their different 3D shapes. Two automated 3D data processing approaches were presented in this research:

1). 3D quadratic facet model fitting, which employed a small concaved 3D patch to fit 3D apple surface, and the best fit could be found around stem-end/calyx area; and

2). 3D shape enhanced transform (SET), which enhanced the apple stem-end/calyx area, and made it easily detectable, according to the 3D surface gradient difference between the stem-end/calyx and the apple surface.

Apple 3D surface was reconstructed from 2-D NIR images according to Shape-From-Shading (SFS) method. Unlike 2½-D approach, the SFS took advantage of the whole image information, which meant a more detailed apple 3D description could be obtained. The proposed 3D approaches did not depend on the location of the stem-end/calyx on the apple surface, making it more suitable for apples orientated randomly. There was also no additional light source required in the imaging system: normal visible white light plus a NIR filter was enough. In addition, the proposed 3D approaches were found to be robust to the noise and incomplete image data. In this Chapter, 3D apple surface reconstruction is introduced in section 5.2.1. In section 5.2.5, two automated 3D data processing approaches are described in detail. The experimental results as well as the discussion are given in section 5.3 followed by conclusions in section 5.4.

## *5.2 Materials and Methods*

The dataset grabbed by the imaging system contained a total of 203 NIR Golden Delicious apple images, which included ones with and without stem-end/calyx. Blemished apples were also included in the data set. The detailed composition of the dataset is shown in Table 7.

**Table 7. Detailed composition of test samples**

| Sample Labels | Number of Samples |
|---|---|
| Apple NIR images with Stem-end/Calyx | 140 |
| Apple NIR images without Stem-end/Calyx | 63 |
| Total | 203 |

### 5.2.1 3D apple surface reconstruction

#### *5.2.1.1 Preprocessing*

The original NIR apple image is shown in Figure 18 (a). The intensity of the background varies and is relatively darker than the apples. In order to perform the 3D reconstruction approach, the non-uniform background must be removed. In addition, each different apple is a region of interest (ROI) and needs to be extracted individually. Based on the experimental data, a single threshold $T_1$ was used to coarsely segment apples from the background. Because some dark areas within apples might also be removed during the thresholding, a 2-step morphological operation was then employed to refine the segmentation:

1). Hole-fill operation, which fills the "holes" in the image. A hole is an area of background pixels surrounded by foreground pixels. In our case, it refers to those removed dark areas within apples, such as defects, stem-ends and calyxes, which need to be preserved in later processing.

2). Area open operation based on pixel counts, which removes the small foreground "objects" with $T_2$ pixels or less. $T_2$ is a pre-determined threshold. In other words, this operation discards those brighter pixels that do not belong to apples but background. The discarded pixels come from the false segmentation due to the intensity variation of background.

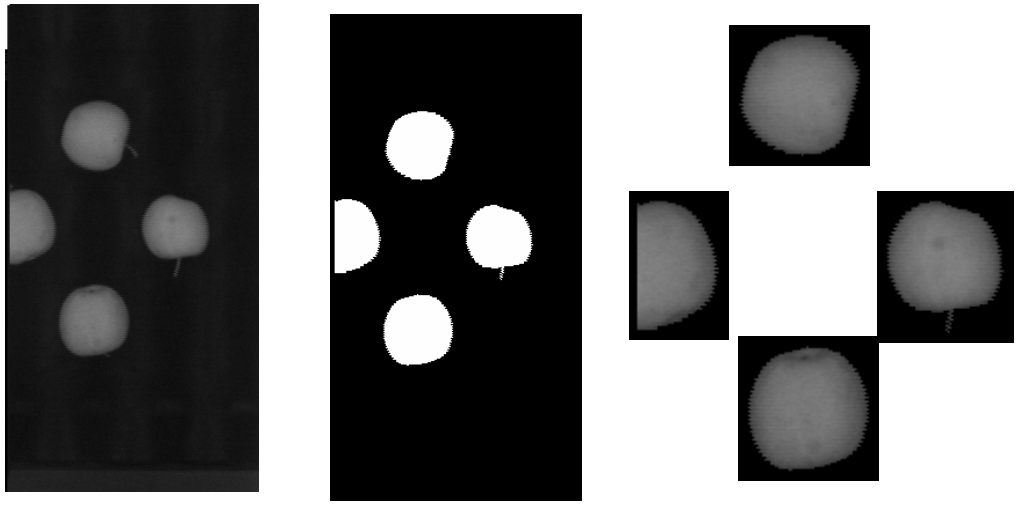

(a) (b) (c)

**Figure 18. Typical NIR images (a) Original NIR image. (b) Refined segmentation. (c) Extracted individual apple image.**

Each apple in a single image also needed to be extracted individually. To achieve this goal, the boundary of each apple was first obtained according to the refined segmentation. Then, coordinates of the circumscribed rectangle of each apple could be easily determined using the boundary information. The segmented images as well as individual apple images are given in Figure 18 (b) and (c), respectively.

*5.2.1.2 Lambertian reflectance model*

In the real world, object surfaces vary according to physical characteristics. In general, surface can be categorized as pure Lambertian, pure specular, hybrid, or more sophisticated models (Zhang, et al., 1999). An apple NIR image was essentially formed under multiple optical effects, i.e. part of the light source were directly reflected by the apple surface, while others entered the sub-surface, scattered and then reflected back to the camera. Specifically, apple surfaces might not be an ideal Lambertian surface; however, based on the experimental results, the net result of an apple surface reflectance under NIR spectroscopy demonstrated a good approximation to the Lambertian model.

A Lambertian surface is a perfectly diffusing/matte surface, which means it adheres to Lambert's cosine law. In this model, the amount of reflected energy is constant in any one direction, i.e., the reflected intensity is not dependent on the viewing angle, but on the light source's orientation relative to the surface. Therefore, the Lambertian surface can be modeled as the product of the light source intensity $I_0$, the surface albedo $\rho$, and the cosine of the angle $\cos\theta$, between source direction $S = (s_x, s_y, s_z)$ and surface normal $N = (n_x, n_y, n_z)$, shown in Figure 19:

$$I = I_0 \rho \cos\theta \tag{5.1}$$

where $I$ is the reflected intensity. Equation (5.1) can be written in vector format when the surface normal and light source directions are both unit vectors:

$$I = I_0 \rho N \cdot S \tag{5.2}$$

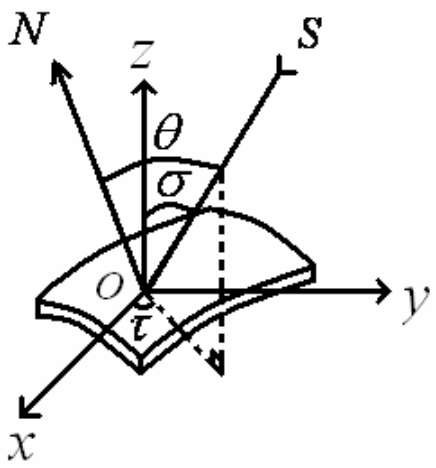


**Figure 19. Illustration of Lambertian model**

*5.2.1.3 Estimation of pseudo illuminant direction*

In this research, although multiple warm-white fluorescent lamps were used to provide uniform lighting, one equivalent (pseudo) light source needed to be determined in order to perform the 3D surface reconstruction. The direction of such pseudo light source was estimated according to the shading information, i.e. 2D image intensity (Pentland, 1982). Given any particular 8-neighborhood direction in the image plane, the following relationship can be obtained:

$$\begin{pmatrix} d\overline{I_1} \\ d\overline{I_2} \\ \vdots \\ d\overline{I_N} \end{pmatrix} = \begin{pmatrix} dx_1 & dy_1 \\ dx_2 & dy_2 \\ \vdots & \vdots \\ dx_N & dy_N \end{pmatrix} \begin{pmatrix} X \\ Y \end{pmatrix} \tag{5.3}$$

where $d\overline{I_i}$ is the average image intensity change along the *ith* direction $(dx_i, dy_i)$, *(X,Y)* is the estimation of *x* and *y* components of the tilt angle $\tau$ (the angle the image plane component of the light source vector makes with the x-axis), and *N* is the total

number of directions considered. $N$ was set to 8 in this study by considering the balance between performance and computational time. Define $D$ as the direction matrix in Equation (5.3), it is easy to get:

$$\begin{pmatrix} X \\ Y \end{pmatrix} = (D^T D)^{-1} D^T \begin{pmatrix} d\overline{I_1} \\ d\overline{I_2} \\ \vdots \\ d\overline{I_N} \end{pmatrix}, \qquad D = \begin{pmatrix} dx_1 & dy_1 \\ dx_2 & dy_2 \\ \vdots & \vdots \\ dx_N & dy_N \end{pmatrix} \tag{5.4}$$

Then, the tilt angle $\tau$ can be determined by:

$$\tau = \arctan\left(\frac{Y}{X}\right) \tag{5.5}$$

and the slant angle $\sigma$ (the angle the illuminant vector makes with the z-axis) is calculated as:

$$\sigma = \begin{cases} \arccos(\sqrt{1-(X^2+Y^2)/K^2}) & if\ X^2+Y^2 \le K^2 \\ 0 & otherwise \end{cases} \tag{5.6}$$

where

$$K = \sqrt{E\{dI^2\} - (E\{dI\})^2} \tag{5.7}$$

The relationship among tilt $\tau$, slant $\sigma$, surface normal $N$ and light source direction $S$ is schematically illustrated in Figure 19. Notice that the light settings of the apple automatic imaging system are always fixed, and don't change during the on-line inspection. Therefore, the illuminant direction needs to be calculated only once, which can be done offline before the system is running. In this study, ten uniformly arranged warm white fluorescent lamps were used to provide a uniform lighting condition, which meant even the hardware configuration was known, the calculation

of light source was still necessary in order to determine the pseudo light source direction, and hence provided the tilt and slant angle for the SFS approach. Given the Lambertian model as well as the light source information, the Shape-from-shading method could be used to retrieve the apple 3D shape based on its 2D data.

*5.2.1.4 Shape-from-Shading model*

Shape-From-Shading techniques can be traced back to the early 1970s (Horn, 1970), and are still widely studied by researchers (Prados, et al., 2002; Kimmel and Sethian, 2001; Prados and Faugeras, 2003; Crouzil, et al., 2003; Tankus, et al., 2004). The basic idea of this approach is to derive a 3D scene description from 2D information, such as a 2D image intensity map. In this research, the Pentland's SFS method (Pentland, 1989) was chosen for the apple 3D surface recovery.

In order to introduce the SFS algorithm, it is useful to rewrite light source and surface normal vectors in the following forms:

$$S = (s_x, s_y, s_z) = (\cos\tau \sin\sigma, \sin\tau \sin\sigma, \cos\sigma) \tag{5.8}$$

and:

$$N = (n_x, n_y, n_z) = \frac{(P, Q, 1)}{\sqrt{P^2 + Q^2 + 1}} \tag{5.9}$$

$$P = \frac{\partial z(x,y)}{\partial x}, \qquad Q = \frac{\partial z(x,y)}{\partial y} \tag{5.10}$$

Based on the Lambertian model in Equation (5.2), and Taylor series expansion up to the first order, the following relationship can be obtained:

$$I(x,y) = \cos\sigma + P\cos\tau\sin\sigma + Q\sin\tau\sin\sigma \tag{5.11}$$

By taking the Fourier Transform of both sides of Equation (5.11), taking off the DC component, and rearranging the equation, it is easy to get:

$$F_z(f_1, f_2) = \frac{1}{2\pi i} \frac{F_I}{f_1 \cos\tau\sin\sigma + f_2 \sin\tau\sin\sigma} \tag{5.12}$$

where $F_z(f_1, f_2)$ is the 2D Fourier Transform of the apple depth map $Z(x,y)$, and hence,

$$Z(x,y) = IFT\{F_z(f_1, f_2)\} \tag{5.13}$$

Since both 2D fast Fourier and inverse Fourier Transforms are available, the solution can be calculated very quickly.

### 5.2.2 3D analysis for apple stem-end/calyx identification

#### *5.2.2.1 3D Shape-Enhanced-Transform (SET)*

Given a recovered apple 3D surface, stem-ends/calyxes can be identified from defects according to their different 3D shapes. An example is given in Figure 20. Generally, apple stem-ends/calyxes have a deep concave shape (Figure 20(a)), while apple defects exhibit small indentations (Figure 20(b)), which are much shallower and flatter in their 3D shape than the stem-ends and calyxes.

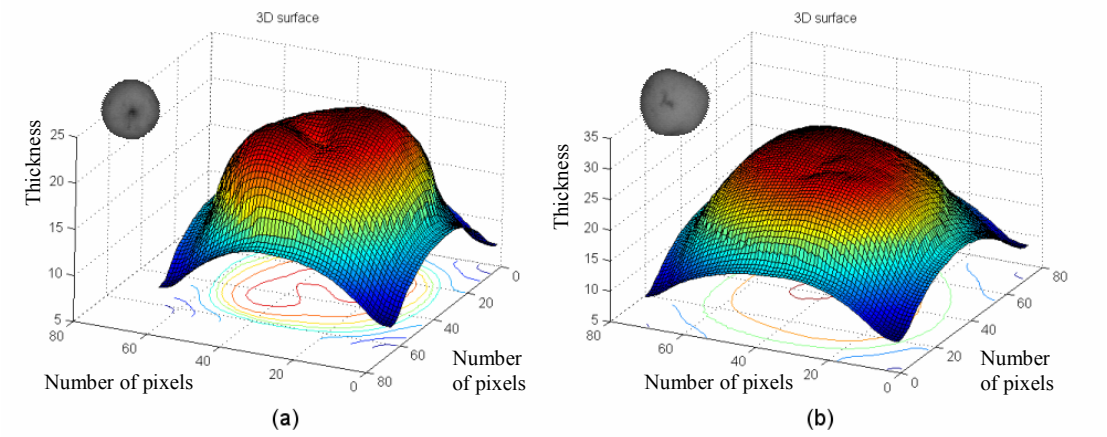


**Figure 20. Recovered apple 3D surface (a) Apple with calyx. (b) Apple with defect.**

It is obvious that the deep concave shape, i.e. apple stem-end/calyx area, has a higher surface gradient in most directions than any other apple surface areas including defects. Given the apple surface gradient $G = <P, Q>$, $P$ can be rewritten as Equation (5.14) according to Equation (5.10) and (5.13):

$$P = \frac{\partial z(x,y)}{\partial x} = \frac{\partial IFT\{F_z(f_1,f_2)\}}{\partial x} = \frac{\partial(\int_{-\infty-\infty}^{+\infty+\infty} F_z(f_1,f_2)e^{i2\pi(f_1x+f_2y)}df_1df_2)}{\partial x} \tag{5.14}$$

where,

$$F_z(f_1,f_2) = \frac{-iF_I(f_1,f_2)}{2\pi(f_1\cos\tau\sin\sigma + f_2\sin\tau\sin\sigma)} \tag{5.15}$$

and

$$F_I(f_1,f_2) = \int_{-\infty-\infty}^{+\infty+\infty} I(x,y)e^{-i2\pi(f_1x+f_2y)}dxdy \tag{5.16}$$

Noticing $F_z(f_1, f_2)$ is not the function of $x$ and $y$, Equation (5.14) can be further written as:

$$P = \int_{-\infty-\infty}^{+\infty+\infty} F_z(f_1, f_2) \frac{\partial e^{i2\pi(f_1 x + f_2 y)}}{\partial x} df_1 df_2 = 2\pi i \int_{-\infty-\infty}^{+\infty+\infty} f_1 F_z(f_1, f_2) e^{i2\pi(f_1 x + f_2 y)} df_1 df_2 \quad (5.17)$$

Substituting Equation (5.15) into (5.17):

$$P = \int_{-\infty-\infty}^{+\infty+\infty} \frac{f_1 F_I(f_1, f_2)}{(f_1 \cos\tau \sin\sigma + f_2 \sin\tau \sin\sigma)} e^{i2\pi(f_1 x + f_2 y)} df_1 df_2 \quad (5.18)$$

Similarly, Q can be expressed as:

$$Q = \int_{-\infty-\infty}^{+\infty+\infty} \frac{f_2 F_I(f_1, f_2)}{(f_1 \cos\tau \sin\sigma + f_2 \sin\tau \sin\sigma)} e^{i2\pi(f_1 x + f_2 y)} df_1 df_2 \quad (5.19)$$

Defining Direction Vector as:

$$D_i = \left\langle \cos\frac{2\pi i}{n}, \sin\frac{2\pi i}{n} \right\rangle, \ i = 1,2,...,n \ . \quad (5.20)$$

The average absolute value of the directional derivative of any point on the apple 3D surface, $I_E(x,y)$ is expressed as the following equation:

$$I_E(x, y) = \begin{cases} 0, & if \ P = Q = 0 \\ \frac{1}{n} \sum_{i=1}^{n} |G \cdot D_i|, & otherwise \end{cases} \quad (5.21)$$

Since the 3D shape of apple stem-ends/calyxes always has a higher surface gradient in most directions than any other surface area, it has a higher average absolute value of the directional derivative as well. In other words, the apple surface within the stem-end/calyx area has a higher $I_E$ value compared to those low gradient areas. In addition, the $I_E$ value doesn't depend on the position of apple stem-end/calyx, but

only relates to the gradient of the stem-end and calyx, which make the SET suitable for various apple orientations. By subtracting the apple original image from the computed $I_E$ image, a shape enhanced image is obtained by:

$$E_I(x,y) = I_E(x,y) - I(x,y) \tag{5.22}$$

Based on SET, the concave surface area, i.e. apple stem-end/calyx, is enhanced greatly compared to the normal apple NIR image, in other words, the "contrast" between apple stem-end/calyx and other surface areas including defects is enlarged, which makes it feasible to use a single threshold to extract the stem-end and calyx. In order to choose the optimal threshold, multiple tests were performed according to the different thresholds. The relationship between error rate and threshold is plotted in Figure 21.

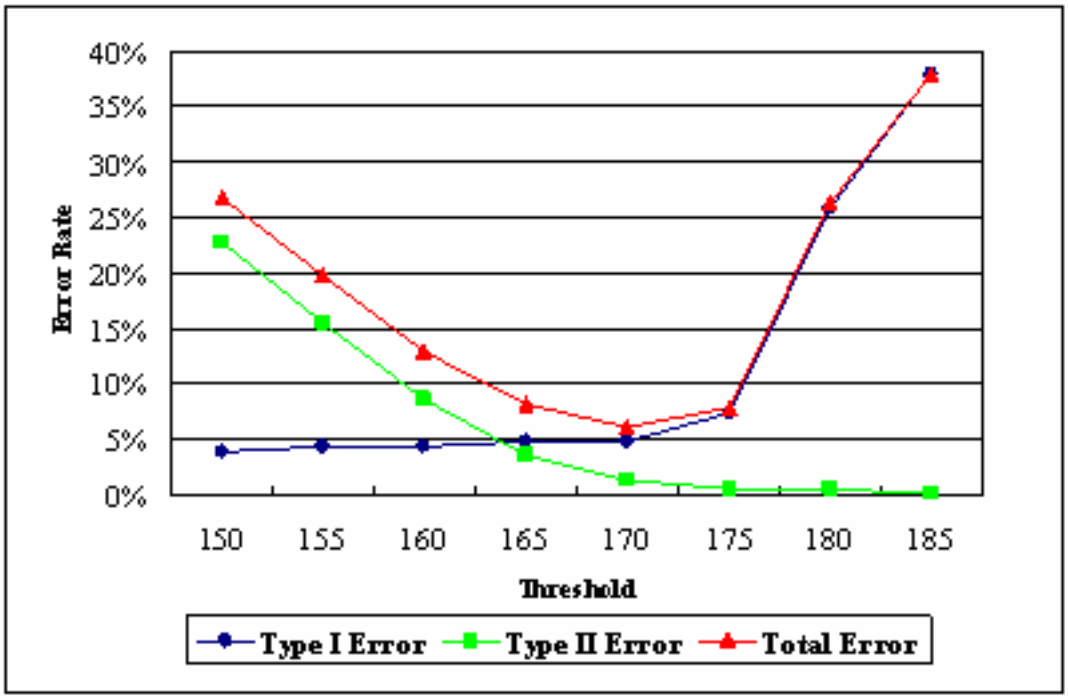


**Figure 21. The choice of optimal threshold**

As shown in Figure 21, the type I error (the line with round marks) increases as the threshold increases, which is expected because higher threshold means stricter on picking the enhanced area. Those areas which are not enhanced "enough" will be dropped by a higher threshold. Similarly, the type II error (the line with square marks) goes down as the threshold increases. This is because under a higher threshold, the algorithm becomes more and more "picky" on choosing the enhanced area, and the chance of falsely identifying a stem-end/calyx becomes smaller and smaller, and even goes to zero sometimes (under threshold 185). Although a very low type I error rate can be achieved under a low threshold, and a very low type II error rate can be gotten under a high threshold, when both error rates are taken into account, the overall error rate (the line with triangle marks) reaches its minimum under threshold 170, which was selected as the optimal threshold during the experiment. Because the SET approach differentiates apple stem-ends/calyxes from defects based on their different 3D shapes, it gives a better performance than the classification methods which solely use 2D information such as image intensity and shape.

*5.2.2.2 The quadratic facet model for stem-end/calyx convex 3D shape fitting*

The principle underlying the facet model is to view the spatial domain of an image as the combination of connected surface pieces, so called facets, each of which satisfies certain shape constraints. In Haralick and Watson's (1981) paper, a sloped/degree-one facet model was employed to fit the test images through least-square estimation. The fitting results were good except some details on the images were lost, which was expected because only a first order polynomial function was used in this paper. Other 3D shape fitting approaches including high order facet models were also applied by

many researchers in the area of image processing, such as edge detection (Haralick, 1983; Haralick, 1984; Ji and Haralick, 2002), image segmentation (Besl and Jain, 1988; Lukács, et al., 1998), object recognition (Hebert, et al., 1995; Blane, et al., 2000), image registration (Scott, et al., 1995; Jiang, et al., 1992; Wyngaerd and Gool, 2002), etc. In this research, the idea of a facet model is extended to do the 3D depth data fitting instead of traditional image intensity fitting to improve apple stem-end/calyx identification.

Because of the apple convex shape (concave in stem-end/calyx) and its smooth surface, it is reasonable to assume that the 3D depth value of a small neighborhood on the apple surface can be approximated by a bivariate quadratic function *g*, and the canonical form of *g* can be given by:

$$Z(x,y) \approx g(x,y) = k_1 + k_2 x + k_3 y + k_4 x^2 + k_5 xy + k_6 y^2 \tag{5.23}$$

The above equation can be rewritten based on a set of discrete orthogonal polynomial basis:

$$g(x,y) = \sum_{i=1}^{6} K_i h_i(x,y) \tag{5.24}$$

where $h_i(x,y) = \{1, x, y, x^2-2, xy, y^2-2\}$, is a set of orthogonal polynomials, and $x = \{-W, .., 1, 0, 1, .., W\}$, $y = \{-W, .., 1, 0, 1, .., W\}$ within the small neighborhood. Here $2W+1$ refers to the windows size of the neighborhood. By comparing Equation (5.23) with (5.24), it is obvious that

$$\begin{cases} k_1 = K_1 - 2K_4 - 2K_6 \\ k_i = K_i, \ \ i = 2,3,..,6 \end{cases} \tag{5.25}$$

The fitting coefficients $K_i$ can be obtained by projecting apple 3D surface map onto the orthogonal polynomial basis:

$$K_i = \frac{\sum_{x,y} h_i(x,y)Z(x,y)}{\sum_{x,y} h_i^2(x,y)} = Z \otimes w_i \tag{5.26}$$

where,

$$w_i = \frac{\sum_{x,y} h_i(x,y)}{\sum_{x,y} h_i^2(x,y)} \tag{5.27}$$

The fitting coefficient $K_i$ is computed by convolving 3D surface map with the corresponding weight kernel $w_i$, which makes the computations much easier than calculating the $k_i$'s from the Equation (5.23) directly (Ji and Haralick, 2002). Among computed fitting coefficients, only $K_4$ and $K_6$ are needed to describe the shape of a quadratic surface of a given type, while others are used to control the orientation and translation of the surface (Besl and Jain, 1985). Some typical quadric shapes affected by coefficient $K_4$ and $K_6$ are illustrated in Figure 22.

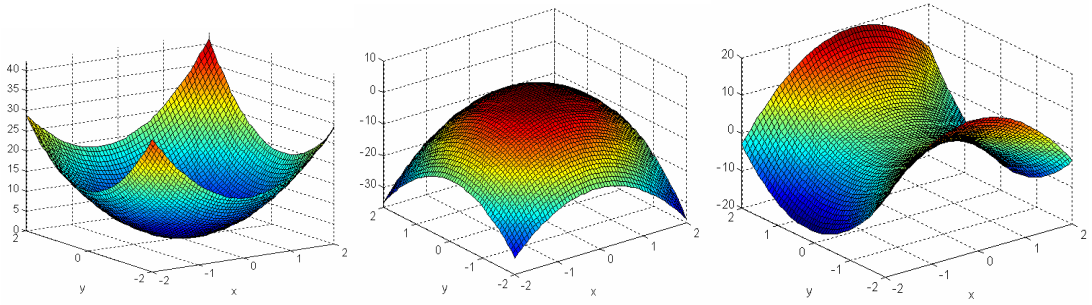

**$K_4 > 0$ & $K_6 > 0$** **$K_4 < 0$ & $K_6 < 0$** **$K_4 < 0$ & $K_6 > 0$**

**Figure 22. Surface shape affected by $K_4$ and $K_6$**

In this study, because the orientation of small piece of facet was negligible compared to the shape itself, plus the translation of the facet had already been considered during the aforementioned convolving, identification of concave shape on the convex apple surface was achieved by simply checking coefficients $K_4$ and $K_6$ according to a pre-determined threshold.

## *5.3 Results and Discussions*

Typical examples of apple 3D surfaces recovered from 2D NIR images (shown on the top-left corner of each image) are presented in Figure 23. Given insufficient image data, such as (a) and (g), the 3D map can still be restored without any visible distortion. Different 3D shape properties among apple normal surface, stem-ends/calyxes and defects can be observed from (c) to (h). Generally, a normal apple surface has the convex 3D shape, while the defects exhibit small indentations, which are much shallower and flatter in their 3D depth than the concave shape of the stem-ends and calyxes. The deep concave shape of stem-ends/calyxes makes it possible for further 3D depth based analysis to detect their correct positions on the apple surface. Corrupted image data are also tested to show the robustness of the algorithm. Relatively good results can be achieved as shown in (i) and (j).

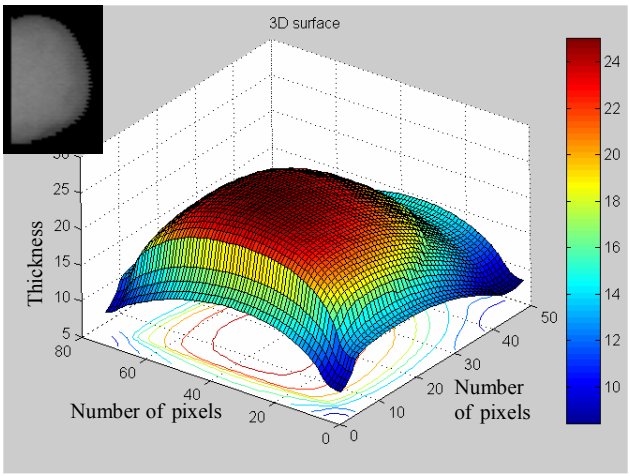


**(a) Normal half apple**

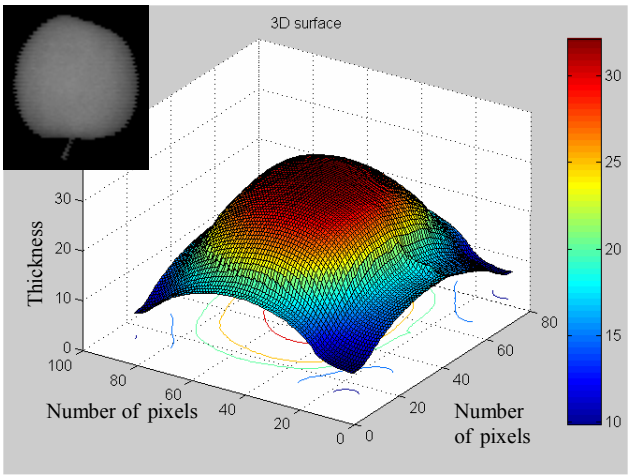


**(b) Normal whole apple**

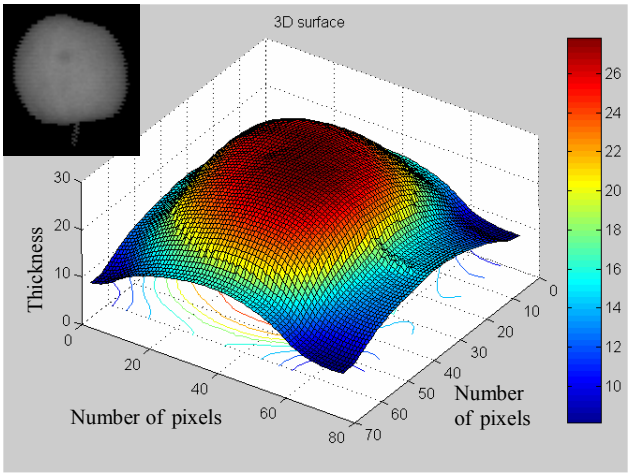


**(c) Apple with single defect**

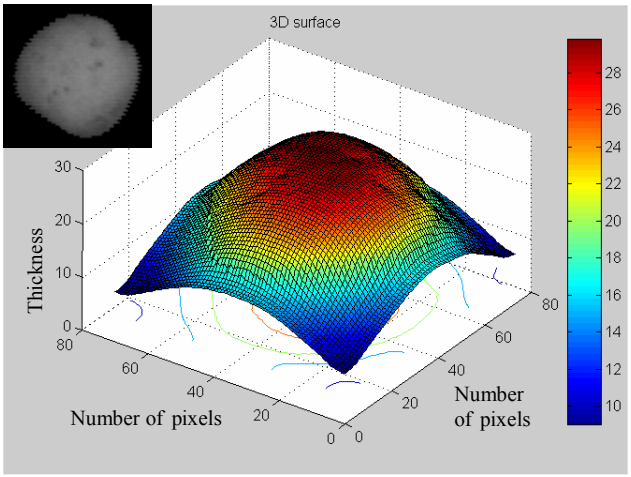


**(d) Apple with multiple defects**

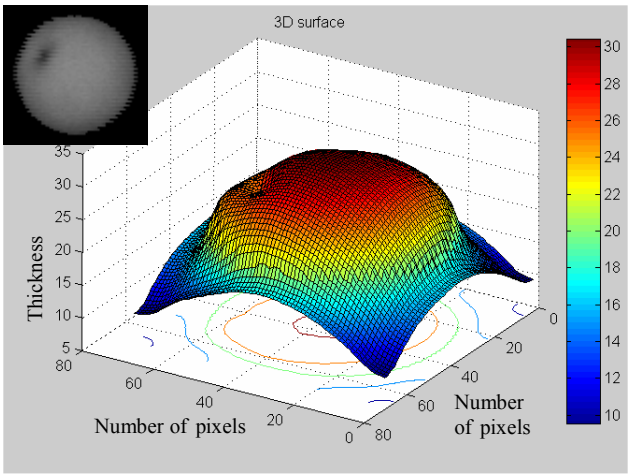


**(e) Apple with calyx**

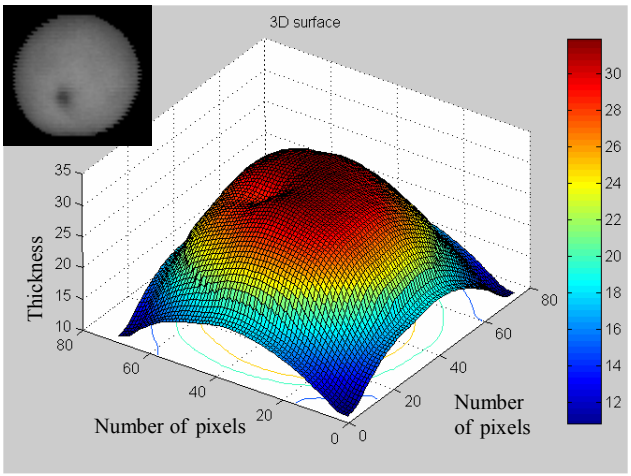


**(f) Apple with calyx**

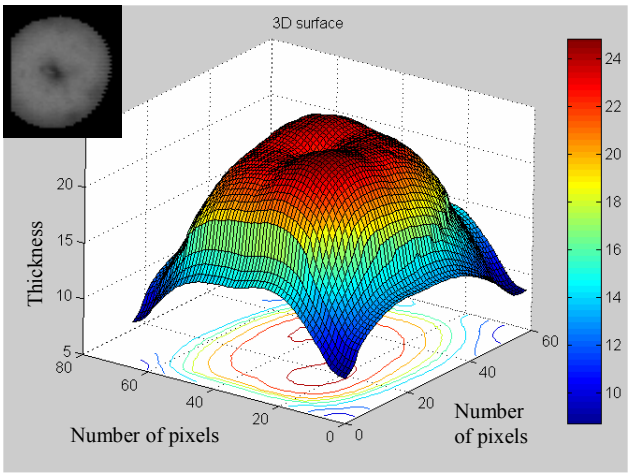


**(g) Apple with stem/calyx and defects**

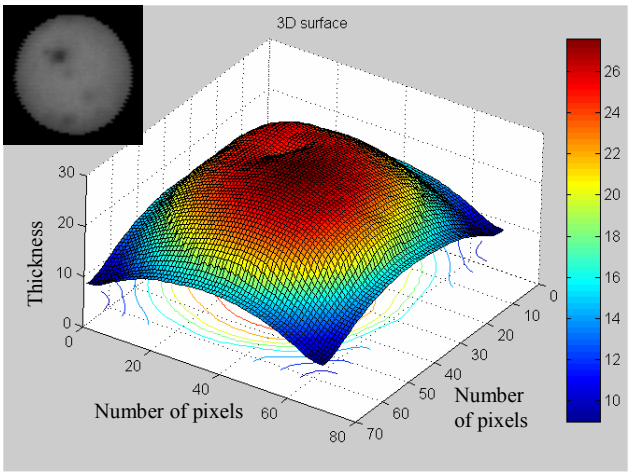


**(h) Apple with stem/calyx and defects**

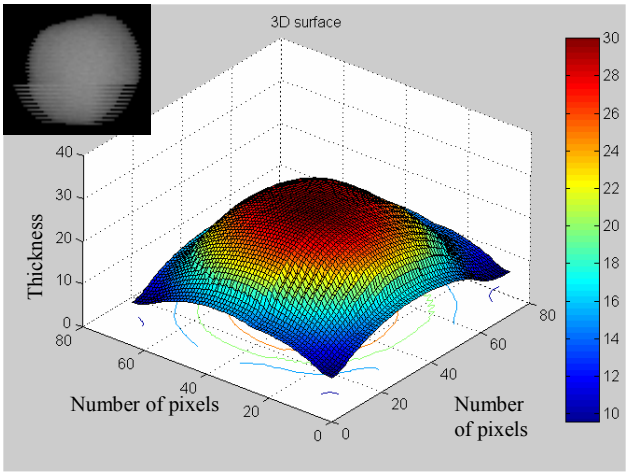


**(i) Corrupted image data (normal apple)**

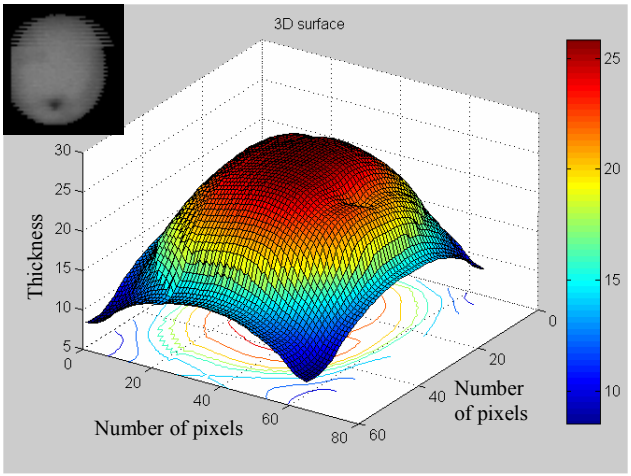


**(j) Corrupted image data (apple with calyx)**

**Figure 23. Reconstructed 3D surface maps of five groups of golden delicious apples (two images/group) based on different apple/image conditions.**

Some typical detection results are given in Figure 24, including (a) apples without defects and stem-ends/calyxes, (b) apples with stem-ends/calyxes only, (c) apples with defects only, and (d) apples with both stem-ends/calyxes and defects. All the apple stem-ends/calyxes were successfully recognized. The apple boundaries were added intentionally to show the accuracy of automated segmentation. All the results

including the added boundaries were obtained automatically by the processing computer using the proposed approaches. As shown in Figure 24, four categories, which are grouped based on different sample quality conditions, are presented from (a) to (d). Figure 24 (a) includes the good apple samples without any stem-ends/calyxes and defects facing to the camera. Figure 24 (b) illustrates the samples only with stem-ends/calyxes showing on the images. All stem-ends/calyxes in Figure 24 (b) were successfully identified regardless of their relative location to the apple surface. Although the defects in Figure 24 (c) varied in size, intensity, quantity and position relative to the apple surface, none of them were detected by the proposed approach. Even though there were not only stem-ends/calyxes but also defects present in the apples in Figure 24 (d), our method correctly differentiated the stem-ends/calyxes from various defects. Given incomplete image data (the last apple in each row), the proposed method still correctly identified the stem-ends/calyxes. In addition, noisy image data, which was caused by alternate scanning of the camera, (sixth image in each row) were also tested to show the robustness of the algorithm.

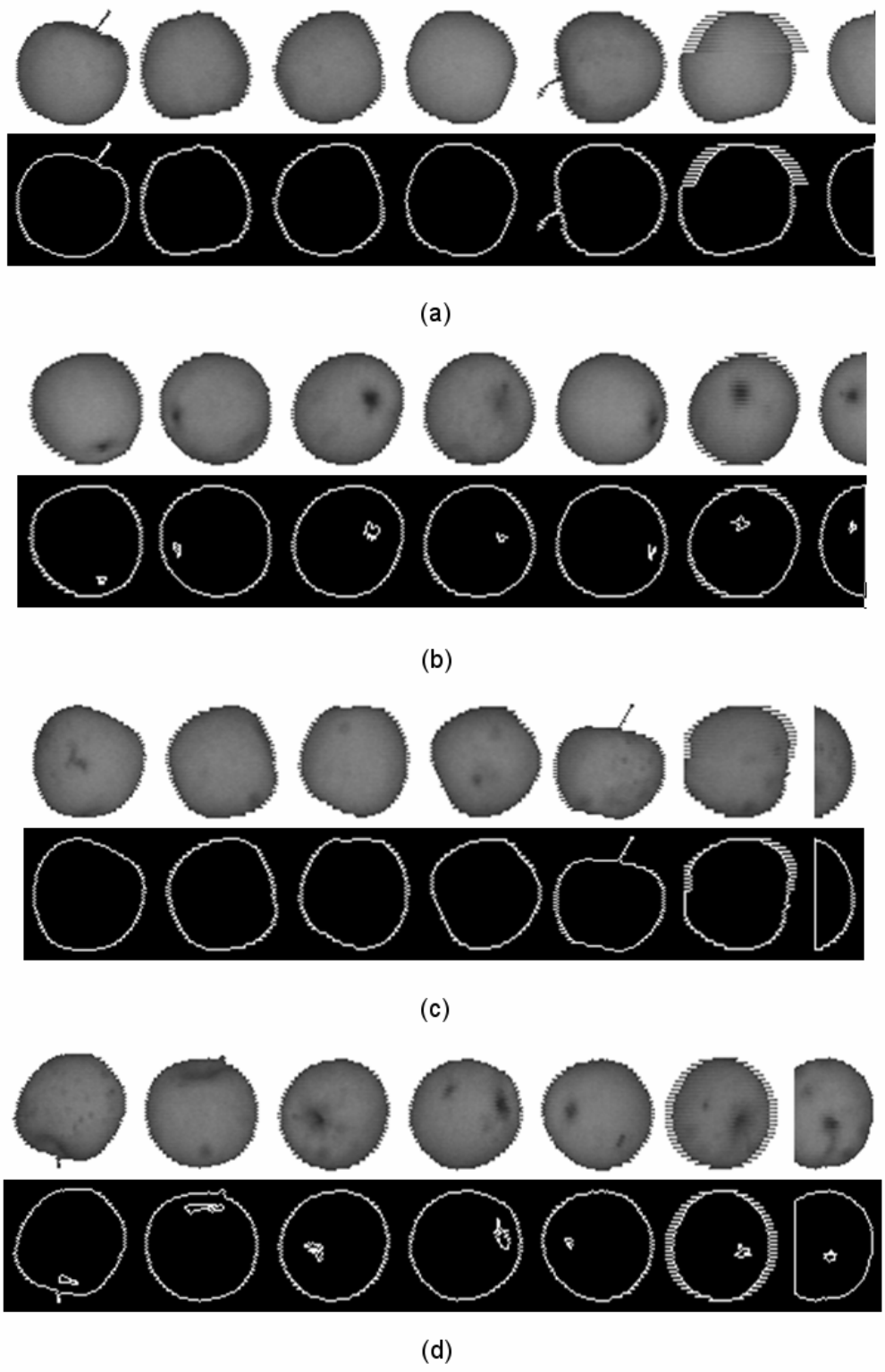

**Figure 24. Typical detection results based on proposed approach under different sample conditions**

The statistics for the detection results based on 203 sample images are shown in Figure 25. Given three different test criteria, consistent detection rates were obtained by both 3D SET and Facet Model Fitting approach. For 3D SET method, an overall 93% detection rate was achieved. For Facet Model Fitting approach, the detection rate was slightly lower than the 3D SET method, but all the results were greater than or equal to 90%.

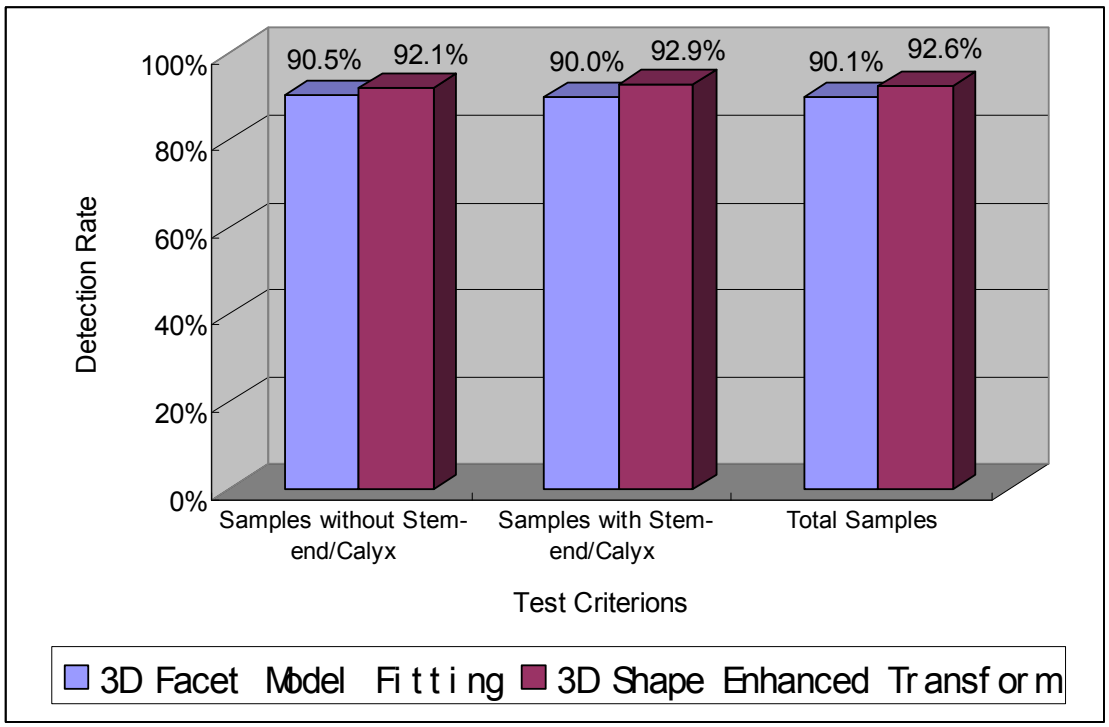


**Figure 25. Detection rate based on three different criterions**

The type I, II and overall error are also plotted in Figure 26. Similarly, both proposed 3D analysis approaches had a low overall error rate, and the performance of 3D SET approach was slightly better than the Facet Model Fitting approach. The average computational time is 50 ms/apple image under a moderate PC configuration, which includes a Intel Core Duo 2.0 GHz CPU and 2.0 GB of RAM.

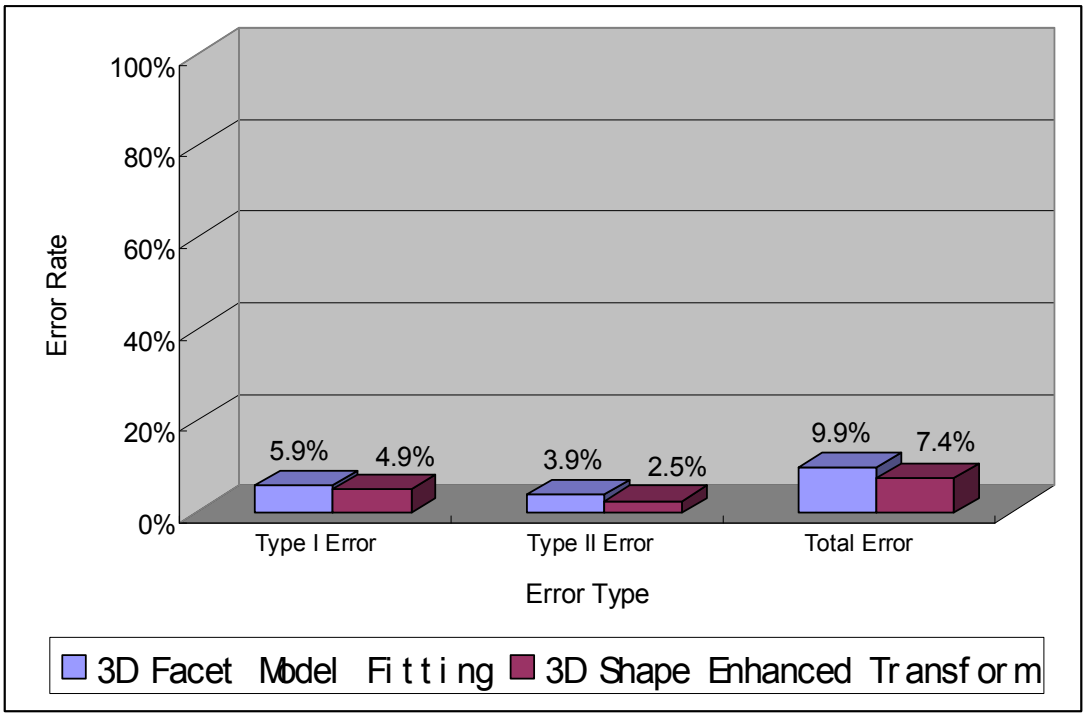


**Figure 26. Detection error rate**

To further evaluate the effectiveness of 3D apple surface reconstruction, the recovered 3D apple surface data was substituted by 2D image intensity value for the comparison purposes. The test results of proposed 3D vs. traditional 2D approaches are shown in Figure 27. The first row of Figure 27 gives the original NIR images, the second row shows the stem-end/calyx identification results using 2D intensity data as the inputs, and the third row represents the identification results using recovered 3D depth as the inputs. Figure 27 (a) is a good apple sample, but one false alarm is generated by 2D method. One calyx in Figure 27 (b) is misidentified by the traditional method, and a false alarm can be found at the same time. In addition, many apple defects are misclassified as stem-end/calyx by the traditional 2D method, which

can be seen from Figure 27 (c) to Figure 27 (d). For all the five examples in Figure 27, the method present in our study gives the correct identification results.

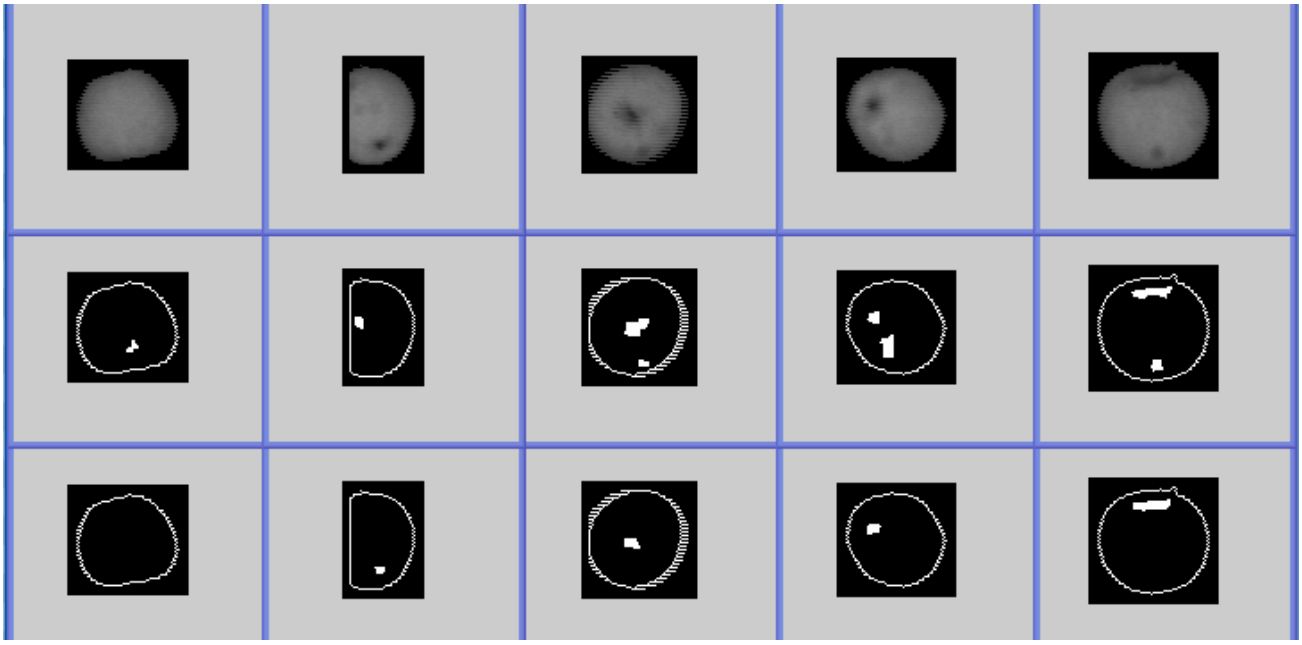


**Figure 27. Comparison on fitting results between using 3D depth (third row) and original image intensity (second row)**

Corresponding statistical analysis between aforementioned two approaches is also demonstrated in Figure 28. Although the type I error of the proposed 3D method is slightly lower than the traditional 2D approach, a much lower type II error can be obtained by the former method than the latter one. As a result, the overall error rate is reduced significantly (from 41.38% to 9.85%) by using proposed 3D based analysis, which shows the effectiveness of 3D apple surface reconstruction.

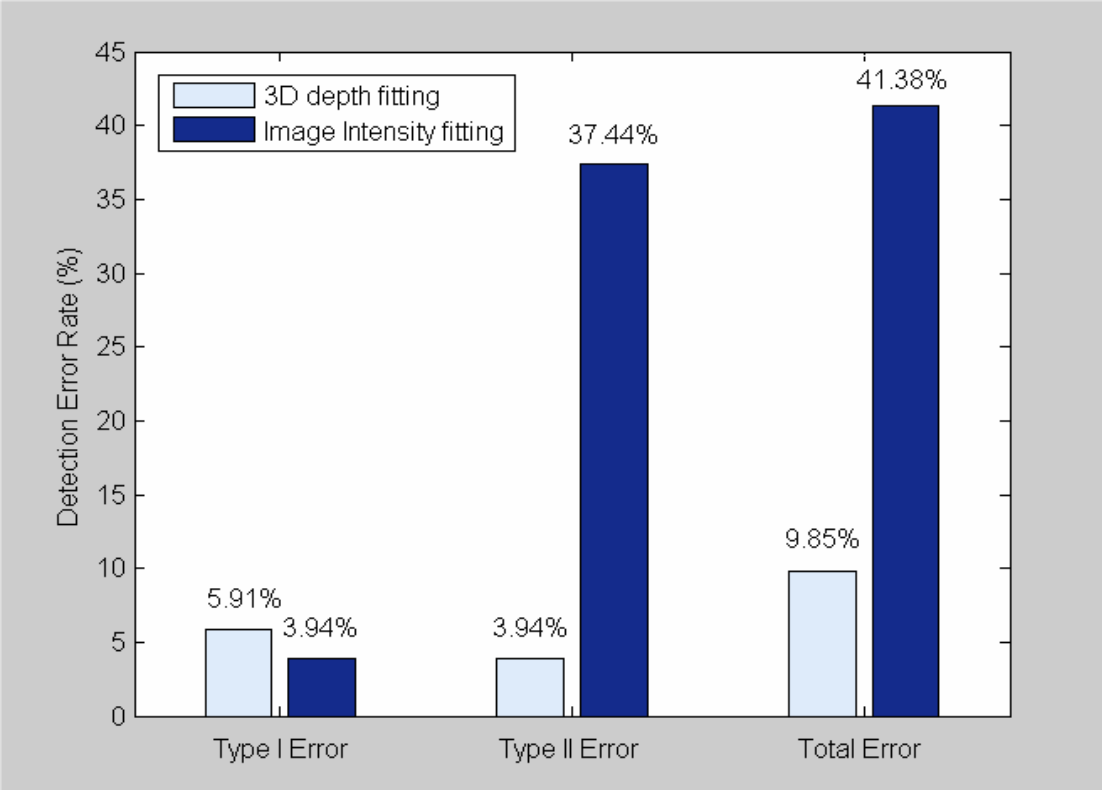


**Figure 28. Comparison between proposed 3D approach and traditional 2D method**

## *5.4 Conclusions*

A novel automated 3D enhancement/analysis approach was developed to identify stem-ends/calyxes on an apple sorting and grading system. The 3D surface of the apple was first recovered based on an SFS algorithm. Unlike structured light range imaging, which only uses partial information of the apple surface, the SFS approach took advantage of the full image information. Every pixel value contributed to the reconstructed 3D map, which meant a more detailed 3D description was obtained. There was no additional light source required in the system: normal visible white light plus a NIR filter was enough. Given successfully recovered 3D depth data, two 3D processing approaches were presented to identify the apple stem-end/calyx based

on their unique 3D properties. Both algorithms were stem-end/calyx position independent, which made them suitable for different apple orientations. They were also robust to noisy data caused by alternate scanning of the camera, and even incomplete data. A total of 203 golden delicious apple images were tested in this research and an overall detection rate above 90% were achieved by both methods.

# CHAPTER 6 IMPROVED 3D RANGE IMAGING AND DYNAMIC THRESHOLDING FOR POULTRY QUALITY INSPECTION

## *6.1 Introduction*

Although X-ray imaging detection has been intensively applied in the poultry industry, this traditional imaging technology has significant difficulties in detecting some contaminations, such as bone fragments, with high accuracy because of thickness variations in poultry fillets. This problem is mainly due to fundamental limitations of X-ray, which always confuses object density and thickness signals in the output X-ray images. A simplified example is given in Figure 29.

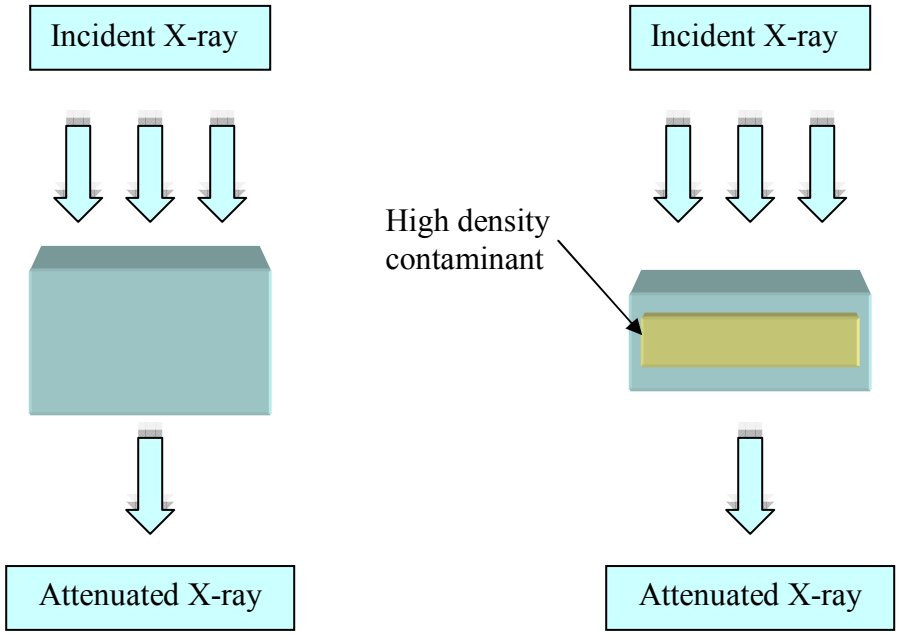


**Figure 29. Thickness and density confusion in X-ray imaging**

Given the same incident X-ray energy level, the X-ray attenuation can be the same between a uniform object and the same object with thinner thickness but a denser contaminant. To solve this problem, a combined X-ray and laser 3D imaging system was developed by employing a laser 3D range imaging sub-system to obtain the thickness variation of poultry fillet, and compensate uneven thickness problem of X-ray imaging. By doing so, X-ray differentiation power for density variation in objects has been significantly improved. The objective of this study was to develop an improved laser 3D-ranging imaging sub-system as well as a novel dynamic thresholding algorithm for the automated bone fragments detection in chicken fillet.

## *6.2 Materials and Methods*

Typical chicken breast samples as well as the bone fragments are shown in Figure 30. Most chicken breasts sold on the market are deboned with fat and skin trimmed out as shown in the first two images in Figure 30. Although they are called "boneless", bone fragments are frequently found in the meat due to human error. Typical bone fragments include small pieces of pulley bones, rib bones, and sometimes fan bones, shown in the third image of Figure 30. Other foreign materials, such as metal chip, are also occasionally found in the chicken meat.

**Figure 30. Chicken breast samples and bone fragments**

In this study, a total 220 pieces of fresh cut chicken boneless breast were tested. All the samples were obtained from a national leading poultry processor, and were assessed at their most fresh condition in order to mimic the real industrial environment of the processing lines. Bone fragments were extracted from the same chicken body with the same freshness. The detailed composition of testing samples is shown in Table 8.

**Table 8. Detailed composition of test chicken samples**

| Sample Labels | Number of Samples |
|---|---|
| Chicken breast fillet with embedded bone fragment | 110 |
| Chicken breast fillet without embedded bone fragment | 110 |
| Total | 220 |

Three typical bone sizes were tested including large, medium, and small or less calcified bones. The detailed composition of bone fragments are given in Table 9.

**Table 9. Detailed composition of bone fragments**

| Bone type | Bone size | Number of Samples |
|---|---|---|
| Large bones | Between 6 and 12 mm | 32 |
| Medium bones | Between 3 and 6 mm | 40 |
| Small bones | Less than 3 mm or Less calcified fan bone | 38 |
| Total | | 110 |

### 6.2.1 Laser 3D range imaging

#### *6.2.1.1 3D reconstruction*

The 3D profile of chicken breast sample was obtained through a structured light beam generated by a laser pattern generator. Given acquired profile points on the camera and the known laser baseline (the line generated with sample on it), the corresponding real world thickness of each point on a laser line could be computed by triangular geometry. Once the thickness of a laser profile was obtained, the 3D profile of a chicken sample was recovered by continuously projecting the laser line onto the moving object, and calculating each associated laser line. A simplified triangular geometry of 3D laser range imaging is illustrated in Figure 31.

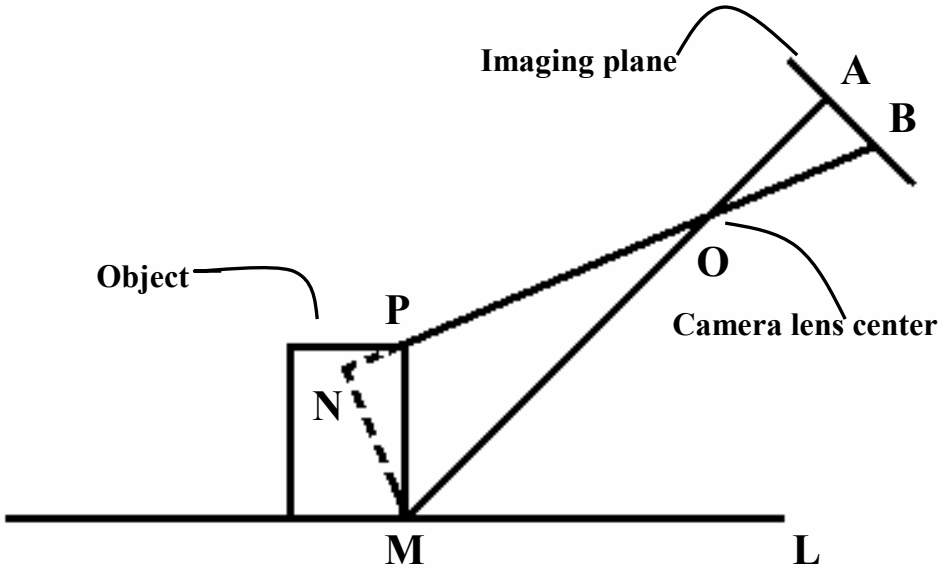


**Figure 31. The schematic of Laser 3D ranging imaging setup**

In Figure 31, both $\angle OAB$ and $\angle PNM$ are right angles and $OA$ equals the focal length of the camera. In addition, AB, OM, $\angle OML$ and $\angle AOB$ can be determined according to the system setup. Therefore, the following relationship can be established:

$$MN = \frac{OM \cdot AB}{\sqrt{AB^2 + OA^2}} \tag{6.1}$$

And

$$\cos \angle PMN = \cos(\left|\angle OML - \angle AOB\right|) = \frac{MN}{PM} \tag{6.2}$$

Consequently, the thickness $PM$ of the object can be obtained by combining Equation (6.1) and (6.2):

$$PM = \frac{OM \cdot AB}{\sqrt{AB^2 + OA^2} \cdot \cos\left|\angle OML - \angle AOB\right|} \tag{6.3}$$

In order to obtain sub-pixel accuracy laser profile extraction, a penalized centroid approach was presented. The traditional centroid method can be expressed as:

$$C(x,y) = \frac{\sum_{(x,y)\in R} K(x,y) \times M(x,y)}{\sum_{(x,y)\in R} M(x,y)} \tag{6.4}$$

Where *K(x,y)* represents the coordinates of image pixels, *M(x,y)* refers to the image intensity, *C(x,y)* is the central point, and *R* is the area where Equation (6.4) is applied. In the ideal situation where only reflectance is present after the incident light hit the object surface, Equation (6.4) can be used to calculate the central point, which is equivalent to the peak point, of the projected laser profile. However, biological materials, such as a chicken meat surface has a much more complicated light reflectance pattern such that the traditional centroid method is usually insufficient to determine the real projected central points. An example is demonstrated in Figure 32 (Jing, et al., 2005; Jing, 2003). In Figure 32, when the incident light ray hits the surface of medium 2, absorption and scattering occurs within that medium, some scattered light will travel back to the medium 1, and eventually reflects back to the image plane through more than one position. Assuming medium 2 is isotropic, which is reasonable for chicken meat, the scatter A and B are at positions symmetrical to the incident light. However, because the distances from scatter A and B to their corresponding image $I_a$ and $I_b$ are different, the reflected image on the image plane

will not have a symmetric shape. To deal with this asymmetric problem, a penalty term was added to the Equation (6.4). Considering 1D case, we have:

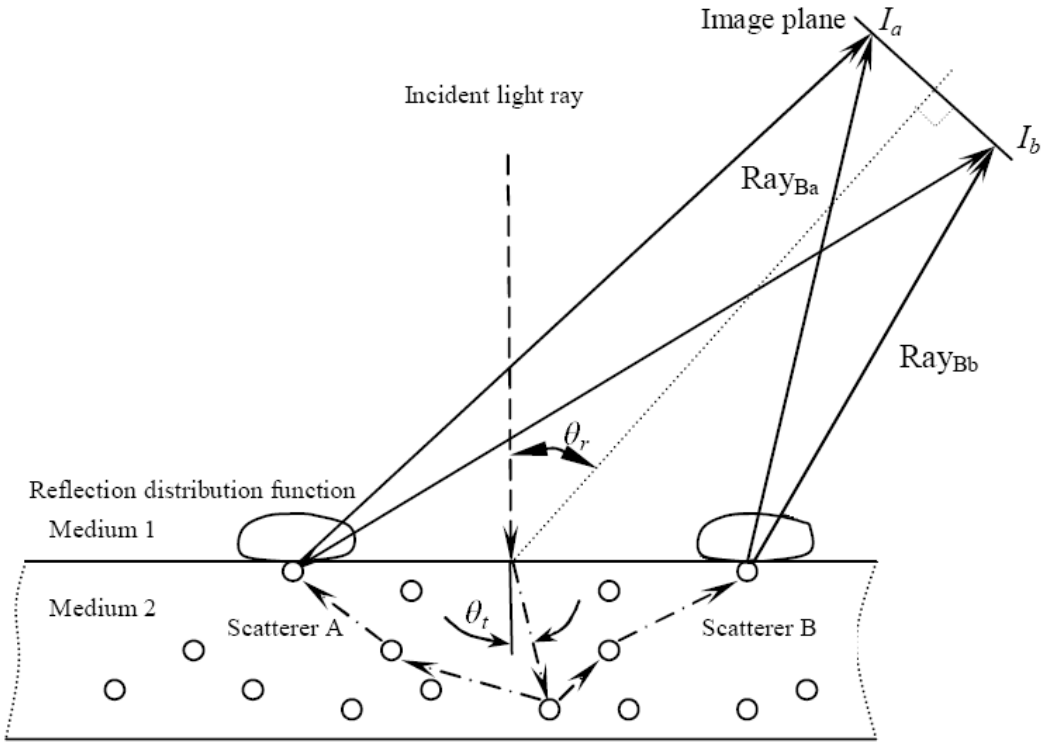


**Figure 32. An example of biological materials surface reflectance pattern**

$$C_P(x) = C(x) + \sigma(x, \theta_r) \tag{6.5}$$

And

$$\sigma(\theta_r, x) = k \frac{\sum_{x<P} S(x, \theta_r) - \sum_{x>P} S(x, \theta_r)}{\sum_{x<P} S(x, \theta_r) + \sum_{x>P} S(x, \theta_r)} \tag{6.6}$$

Where $S$ is the reflected light radiance, $\theta_r$ is the angle between incident and reflected light, which is shown in Figure 32, $P$ is the real peak point of the profile, and $K$ is a constant. It is obvious that if when a symmetric profile is reflected to the image plane,

the penalty term in Equation (6.6) becomes zero, and hence Equation (6.5) turns into the traditional centroid equation (6.4).

*6.2.1.2 System design*

Originally, the fused X-ray and Laser detection system was designed with single-lane coverage. Single-lane coverage referred to the maximum area covered by one pair of cameras used for Laser 3D range imaging. Two cameras were used in order to remove the occlusion (Jing, 2003) caused by irregular shape of samples. It was obvious that increasing the coverage area could increase the throughput if the processing time remained the same. Therefore, another pair of cameras was added into the imaging system for extended coverage. However, system extension brought more data flow and complexity of control and synchronization into the system. In addition, because the coverage of the X-ray imaging system in the original design was twice that of the single-lane Laser 3D range imaging, the extra burden incurred by system extension mainly came from the extension of the Laser sub-system. As a result, how to carefully design the Laser multi-lane imaging sub-system became an important factor in improving the overall system performance.

*Multi-threaded programming*: The traditional and straightforward task processing approach is single-threaded sequential processing, which is the only available approach in some of the early operating systems, such as DOS, and is still widely used in many applications today. Although it has many advantages including easy design and implementation, less complexity, modest resource consumption, etc., one major drawback of sequential processing is low time efficiency because the processor

can only process one specific task at any given time in a single-threaded system. If an application generates a large number of tasks within a short time period, the waiting time to finish such application will be extremely long. One way to overcome this problem is multi-threaded programming, which fully utilizes the system resources and keeps the time delay between tasks to a minimum.

*Memory management:* In the aforementioned multi-threaded system, some data buffers were accessed by every thread. In order to prevent data from being lost or corrupted, memory access had to be carefully managed and synchronized. In the case where frequent read and write operations would be executed on the same memory block, a ring buffer was employed to improve the efficiency of data fetching. In the ring buffer design, two pointers are used for data reading and writing, and they are not pointed to the same memory block. By doing so, both writing and reading operations can be performed simultaneously as long as the data reading speed is equal to or faster than the writing speed. A ring buffer usually has *n* memory blocks, and once the block *Bn* is filled with data, *B1* will be the next block to be written. This can also be called launch-and-forget mode where the control of the program will be returned to the main thread once the data writing command is issued, and no waiting is necessary for the actual writing operation. The ring buffer mode is more time efficient than the traditional lock-and-release memory access mode where waiting is needed for writing operation.

### 6.2.2 Thickness compensated X-ray imaging

*6.2.2.1 Combined X-ray and Laser image*

Once the 3D profile of chicken samples was obtained, the thickness variation of the X-ray image could be compensated using the Laser 3D image. The basic idea of such compensation is shown in Figure 33 (Tao and Ibarra, 2000):

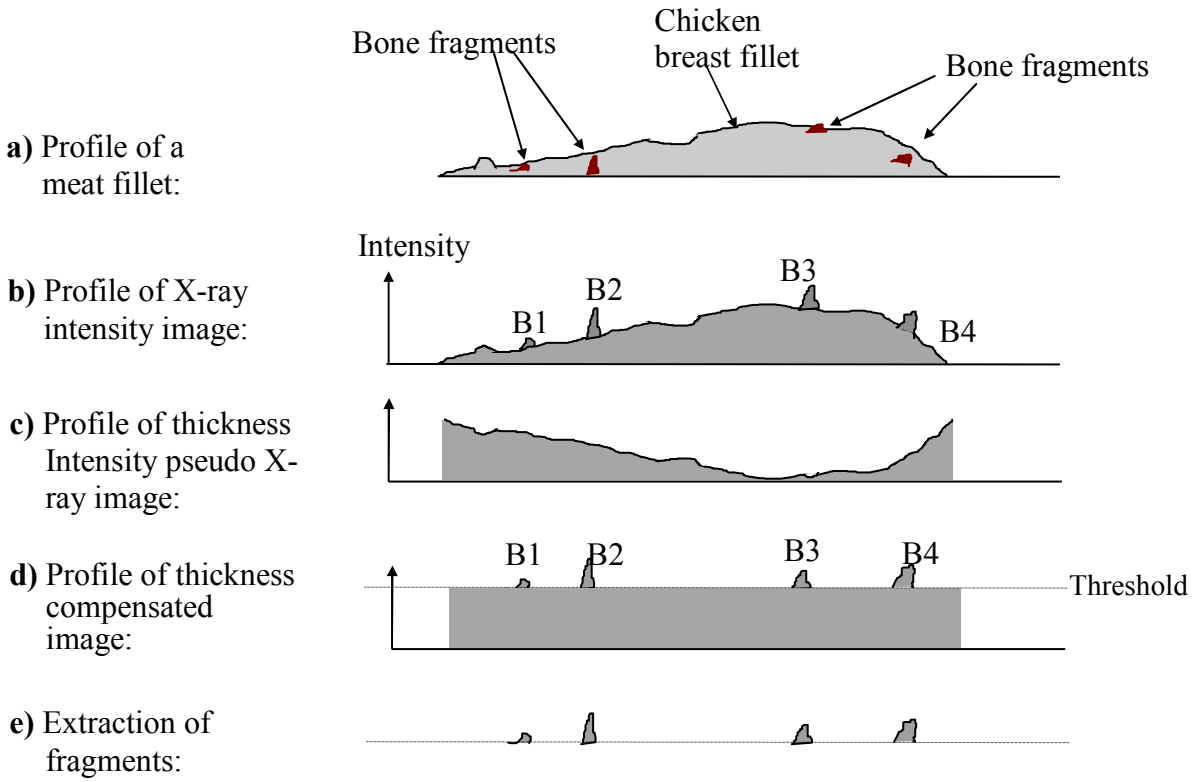


**Figure 33. Thickness compensation using Laser 3D profile**

Given a chicken breast sample with embedded bone fragments in Figure 33 (a), the corresponding X-ray intensity map will look like Figure 33 (b). Due to the uneven thickness, it is impossible to identify all the bone fragments from *B1* to *B4* using a single threshold. More specifically, the intensity of bone fragment *B1* is less than the one of chicken meat around *B3* area, and hence confused with thickness variation of

the fillet. However, if the Laser 3D profile is obtained as in Figure 33 (c), and used to compensate the original X-ray image 33 (b), The thickness compensated image can be obtained in Figure 33 (d). It is obvious that once the thickness variation is removed by the Laser 3D image, all the bone fragments can be easily extracted through a single threshold shown in Figure 33 (d) and (e).

*6.2.2.2 Dynamic Thresholding Algorithm*

According to Figure 33, once the 3D profile of a chicken fillet is obtained, such 3D information is mapped to a pseudo X-ray image, which will then be combined with the original X-ray image. By doing so, ideally, the uneven thickness of the sample can be eliminated, making the foreign materials embedded in the chicken sample easily detectable through a single threshold. However, in the real world situation, noise will be inevitably present during the entire procedure of contaminants detection. The sources of noise include thermal noise from the imaging devices such as cameras and the X-ray detector, electronic noise caused by electronic components, etc. Furthermore, computation errors also exist during 3D reconstruction, X-ray/Laser calibration, etc. Because it is quite challenging, sometimes even impossible to give an accurate description for such noise and error models, the thickness information in the X-ray image can not always be perfectly compensated by the Laser 3D depth. Therefore, using a single threshold can cause potential problems in some cases. This can be illustrated in Figure 34.

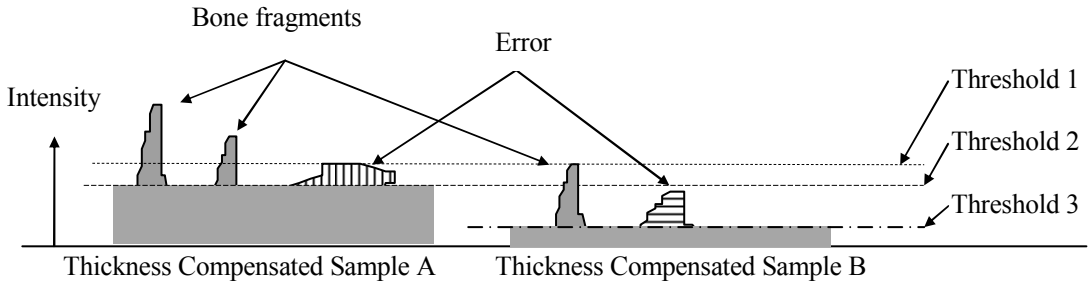


**Figure 34. The disadvantage of single threshold method**

When thickness compensated images are obtained, the bone fragments in sample A can be identified by threshold 1. Similarly, the bones in sample B are extractable through threshold 3. However, it is impossible to identify all the bone fragments without any false alarm by only using a single threshold. Any single threshold choice, such as threshold 2, will cost at least one false alarm – the region filled with vertical lines, and/or one missing bone fragment – the region filled with horizontal lines. To address this problem, the dynamic threshold approach was developed to segment the true bone fragments while keeping the false alarm rate to a minimum. Given a set of consecutive thresholds:

$$T = \{t_0, t_1, \ldots t_N\} \tag{6.7}$$

where $t_0 < t_1 < \ldots < t_N$ and $N$ is the number of thresholds in the set. Let:

$$F(I_0(x,y), t_i) = \begin{cases} 1, & when\ I_0(x,y) \geq t_i \\ 0, & when\ I_0(x,y) < t_i \end{cases} \tag{6.8}$$

where $F$ is the thresholding function and $I_0\,(x,y)$ is the image. Further define:

$$a_{ij} = \sum_{(x,y)\in\Lambda_8(x,y)} F(x, y, t_i), \quad j = 0, \ldots R \tag{6.9}$$

where $R$ refers to the total number of regions of interest under threshold $t_i$ and $\Lambda_8(x, y)$ is the region of connected pixels with 8-adjacency. According to equation ( 6.9), a feature matrix can be obtained as the following:

$$A = \begin{bmatrix} a_{00} & \cdots & a_{0R} \\ \vdots & \ddots & \vdots \\ a_{N0} & \cdots & a_{NR} \end{bmatrix} = [\alpha_{1,}\alpha_{2,}...,\alpha_R] \tag{6.10}$$

where α is the column vector of matrix $A$. Let:

$$dA = [d\alpha_{1,}d\alpha_{2,}...,d\alpha_R]_{,} \quad d\alpha_j = \frac{a_{i+1,j}}{a_{ij}}, \quad i = 0,...,N-1 \tag{6.11}$$

Defining the classification criterion:

$$C_j = DIST\left|d\alpha_j - d\alpha_k\right| \quad j,k = 0,...,R, j \neq k \tag{6.12}$$

where *DIST* is a Euclidean distance between any pair of feature vectors (Hence, $C_j$ is a scalar), the foreign materials and normal tissue classification can be fulfilled through the following equation:

$$if \quad \begin{cases} C_j \leq \varepsilon, & class\ 1 \\ otherwise, & class\ 2 \end{cases} \tag{6.13}$$

## *6.3 Results and Discussions*

### 6.3.1 3D Laser range imaging

A laser 3D imaging subsystem was developed and can be either used as an independent utility software for the testing and/or diagnosing purposes, or integrated with the X-ray imaging system to build the dual X-ray/Laser imaging detector. Some reconstructed 3D images of chicken fillets are shown in Figure 35:

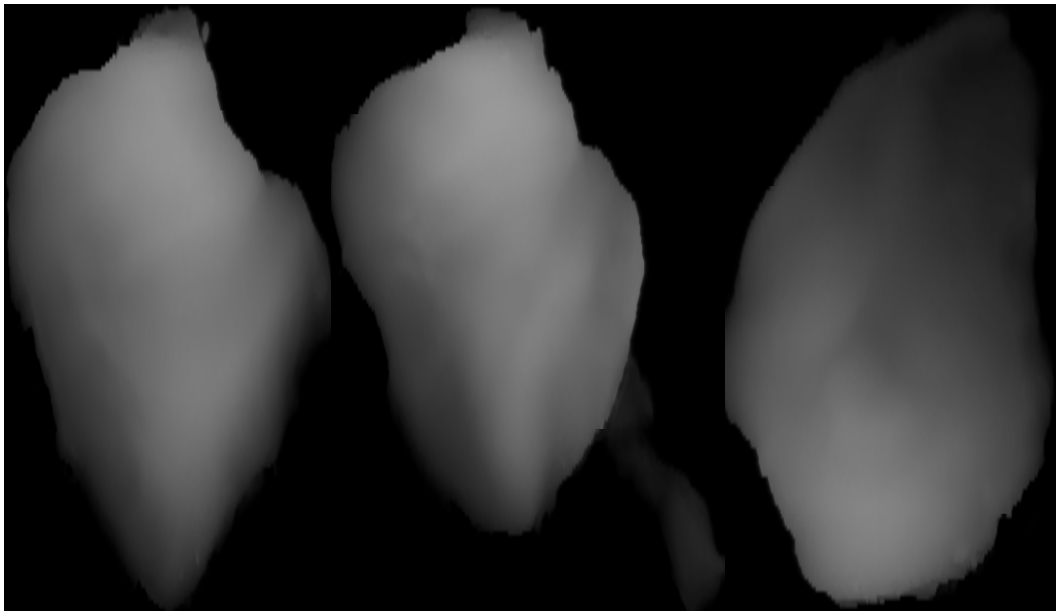

**Figure 35. Examples of reconstructed 3D data from chicken fillets**

The overall 3D range imaging system structure was designed according to the requirement for a high-speed, high-resolution imaging system as seen in Figure 36. The image frame data acquired by each high-speed camera is first sent to an onboard memory by the frame grabber. A total of four ring buffers are used with respect to each camera. Once the minimum process-able memory block is ready, a working thread (*Th*) is notified for data processing. A total of four threads are utilized, and

they are working alternatively in order to avoid the possible data corruption. Each thread applies the proposed 3D reconstruction algorithm to build the 3D profile of the chicken sample, and put such 3D data into a shared memory for further processing. The Message-passing based communication strategy were also designed and integrated into the 3D range imaging system. The text box with light green background shows the messages communicated between Task Manager and working thread.

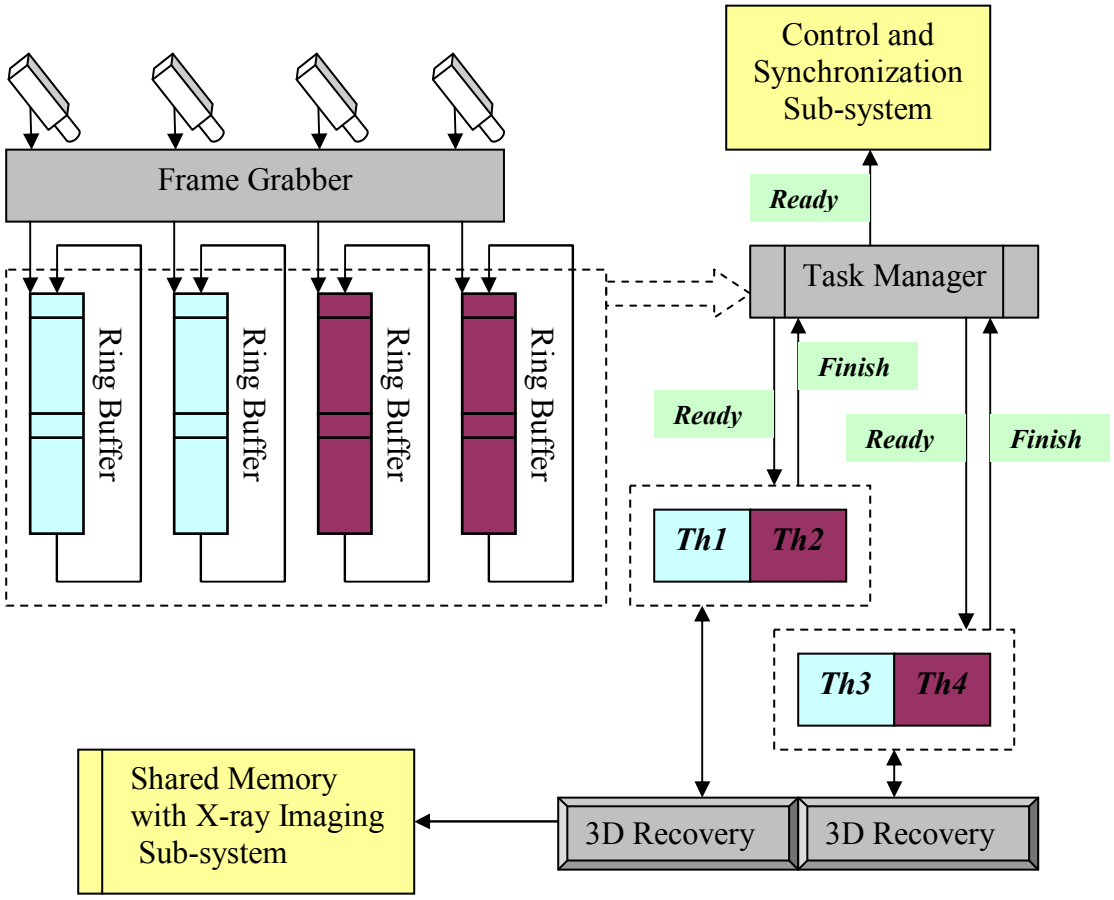


**Figure 36. System structure design and Message communication**

A more detailed 3D profile reconstruction flow chart is given in Figure 37. In this design, both temporal information, such as profile history and the spatial information

like neighboring data are considered to narrow down the search range of the current laser profile. By doing so, the computational time can be significantly reduced.

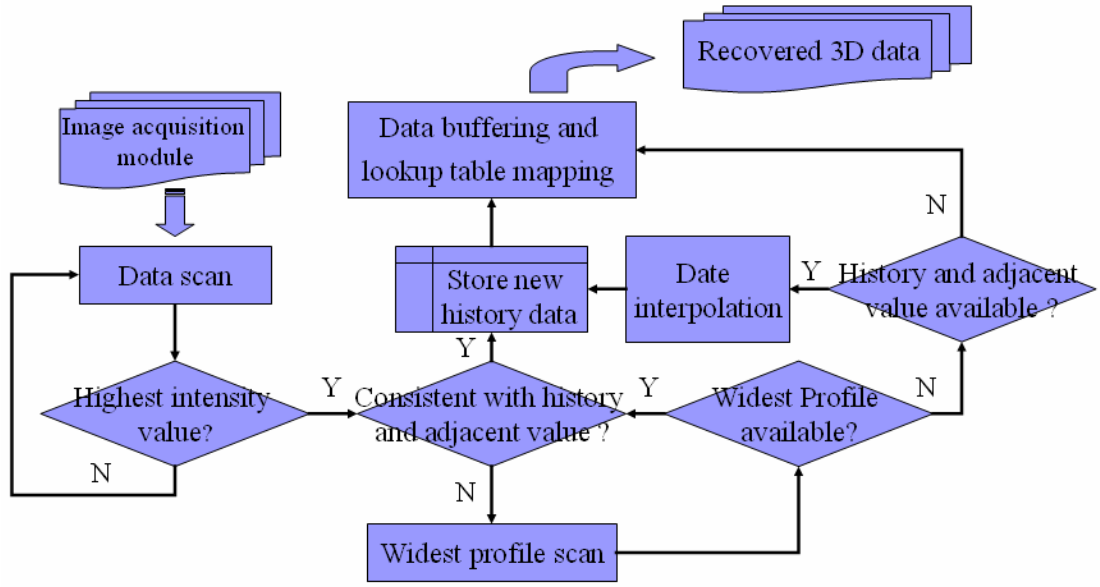


**Figure 37. Flow chart of 3D profile reconstruction**

A quantitative evaluation of the improvement of the two-lane system over the single-lane system is shown in Table 10:

**Table 10. The performance data of current Laser 3D range imaging system**

| | Single-Lane system | Two-Lane system | Improvement |
|---|---|---|---|
| 3D data resolution | 0.8 mm × 0.4 mm × 0.4 mm | 0.4 mm × 0.4 mm × 0.4 mm | 50% |
| Computation time | 5.25 ms/image | 1.31 ms/image | 75% |
| Cover range | 0.3 m | 0.6 m | 100% |

### 6.3.2 Fused X-ray and Laser imaging system

Given reconstructed Laser 3D depth information, the thickness variation in the X-ray image can be removed, and hence the bone fragments embedded in the chicken meat can be easily extracted as shown in Figure 33. Some examples are illustrated below:

In Figure 38 (b), a very detailed 3D profile, including some bumpy area indicated by the dotted circle, is recovered. With the help of laser 3D imaging, the uneven thickness problem can almost be eliminated, and leave the foreign material "stand up", as seen in Figure 38 (c).

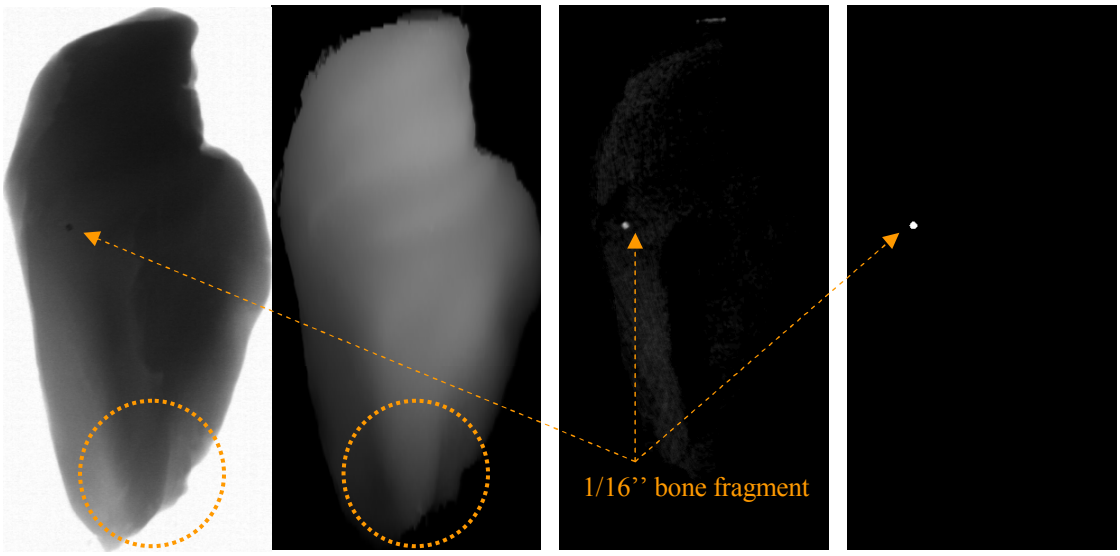


**(a)** **(b)** **(c)** **(d)**

**Figure 38. Bone fragment detection using fused X-ray/Laser imaging (a) X-ray image, (b) Laser 3D image, (c) Combined image, (d) Detection result.**

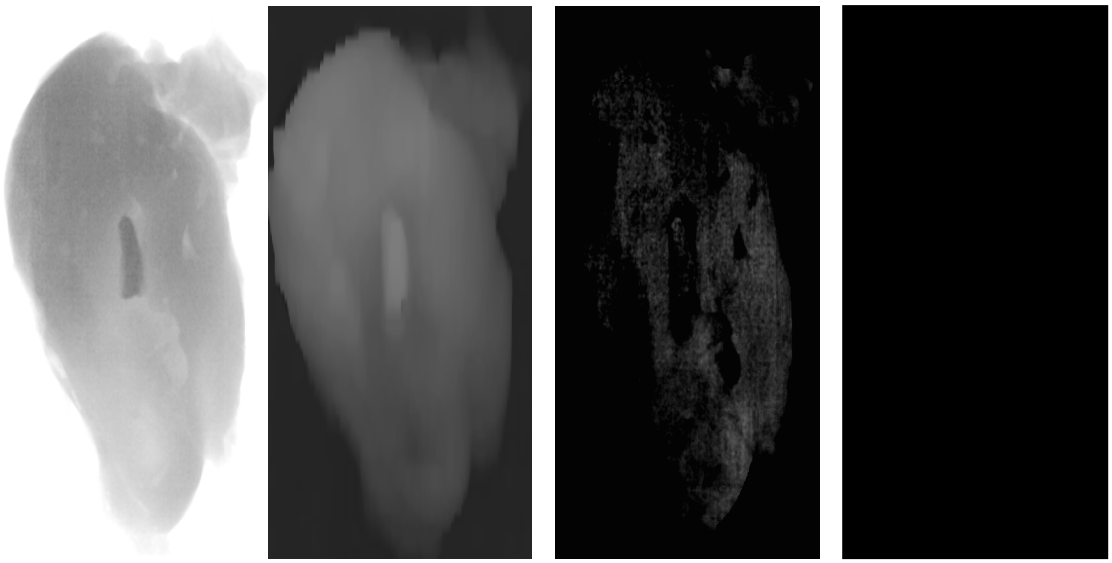

(a) (b) (c) (d)

**Figure 39. Thickness compensation by Laser 3D information (a) X-ray image, (b) Laser 3D image, (c) Combined image, (d) Detection result.**

In Figure 39 (a), a highly suspicious area, which shows a higher intensity value than the surrounding region, can be observed. If only the X-ray image is used, this suspicious area will be considered as a high density foreign material even under eyes of a trained X-ray imaging scientist. However, if Laser 3D image is provided in Figure 39 (b), it is quite clear that the suspicious area also has very high depth value. When the Laser image is combined with X-ray image, the thickness variation is totally cancelled out. As a result, there are no high density foreign materials found in the sample as seen in Figure 39 (d). Previous two examples show the effectiveness of Laser 3D image in the thickness compensation of X-ray image.

In order to quantitatively evaluate the performance of fused X-ray and Laser imaging system, a total of 220 chicken breast fillets were tested, and the overall detection rate

was computed. The overall detection rate was defined as the total number of false detected samples divided by entire sample size, which is 220. A 95% overall detection rate is achieved by dual X-ray/Laser imaging detection. Type I and type II errors are 2.27% and 2.73%, respectively. These results show the effectiveness of aforementioned thickness compensation approaches. However, as discussed in section 6.2.2.2, a single threshold method has disadvantages when noise is included in the combined images due to the inaccuracy of reconstruction, calibration, etc. Such a disadvantage can be illustrated in the following example:

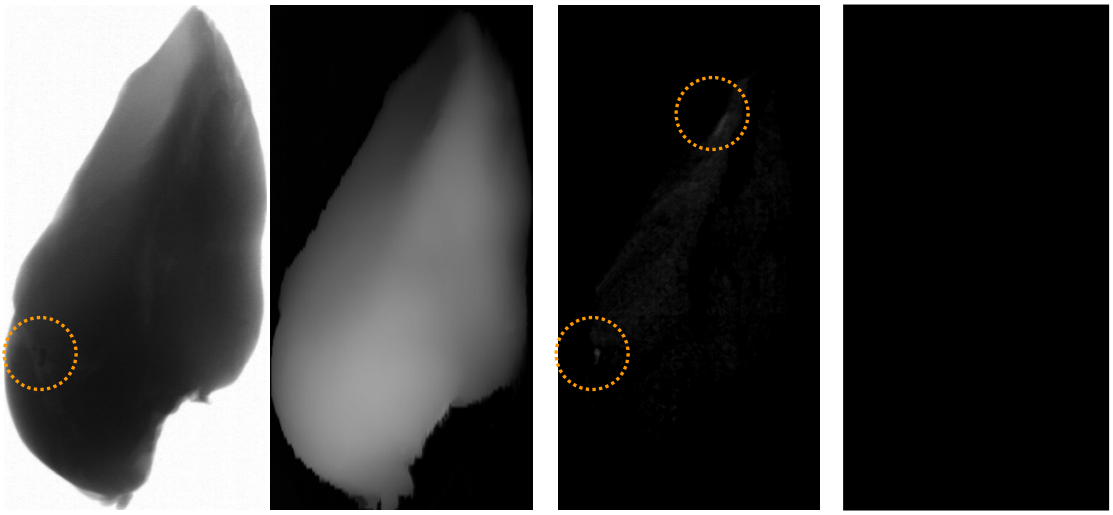

**(a)** **(b)** **(c)** **(d)**

**Figure 40. Thickness compensation by Laser 3D information (a) X-ray image, (b) Laser 3D image, (c) Combined image, (d) Detection result.**

Figure 40 (a) gives an X-ray image with a true, but tiny bone fragment indicated by the dotted circle. After compensating for thickness by Laser 3D image, Figure 40 (c) shows a very weak signal corresponding to the bone fragment. In addition, a suspicious region on the top of the image also shows similar intensity as the bone

fragment. On the final result in Figure 40 (d), both weak signals in (c) are excluded. Considering the ground truth, the tiny bone fragment is missed by the single threshold method. To solve this problem, instead of using only one specific threshold, suppose a set of consecutive thresholds are applied to the combined image (Figure 40 (c)), the respective results are given in Figure 41. It is obvious that any single threshold from (a) to (d) can not get the correct result indicated in Figure 41 (e). Furthermore, when the threshold value greater than the one used in Figure (d) is applied, all the suspicious areas will be removed, and hence no foreign materials will be detected, which is the case in Figure 40.

**(a)** **(b)** **(c)** **(d)** **(e)**

**Figure 41. Detection results under a set of consecutive thresholds (a) Th = 5, (b) Th = 6, (c) Th = 7, (d) Th = 8, (e) True result.**

However, if size change of each suspicious region along with change of threshold is considered, an interesting phenomenon can be found, and demonstrated in Figure 42. It is clear that, both false alarms have a higher rate of change in region size in comparison to that of the real bone fragment. This can be anticipated since noise is usually very sensitive to the change of threshold, while the real bone fragments only

change slowly under the change of thresholds. This is because most pixels of real bone fragment have the same or similar intensities; therefore, any threshold value below such intensity won't cause dramatic change in detected bone size.

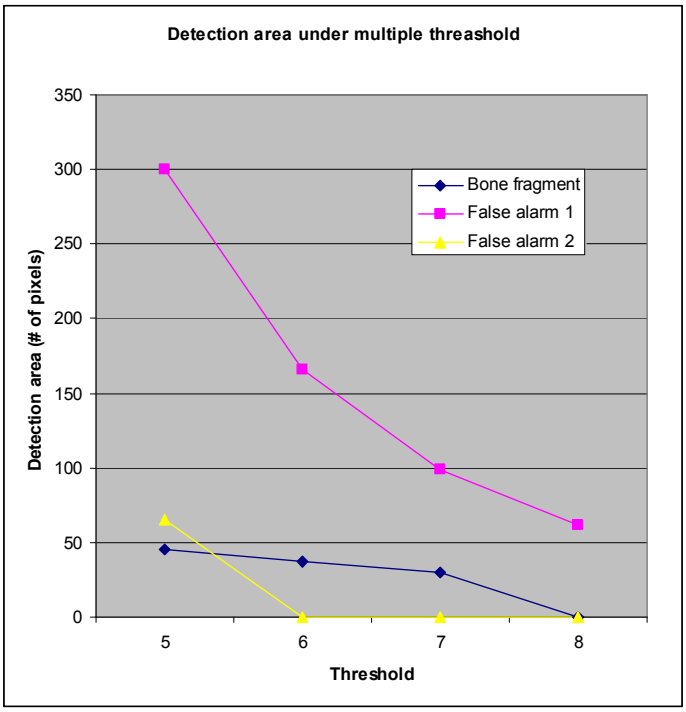


**Figure 42. Detection area change of suspicious objects with change of threshold**

To further illustrate the idea of dynamic thresholding, the area ratio change under multiple thresholds for typical bone fragments and false alarm regions are plotted in Figure 43 and 44, respectively. Shown in Figure 43, most bone fragments have a very slow size change when the threshold increases. More specifically, an approximately 10% reduction in detection size of bone fragments can be observed along the increment of threshold. This shows the insensitivity of real bone size change to the change of threshold. On the other hand, in Figure 44, a dramatic change of size can be seen when the threshold increases. A high inconsistency between change of size and

threshold is present. The above findings agree with our previous statement that bone fragment size change under multiple thresholds is slower and more consistent than false alarm regions.

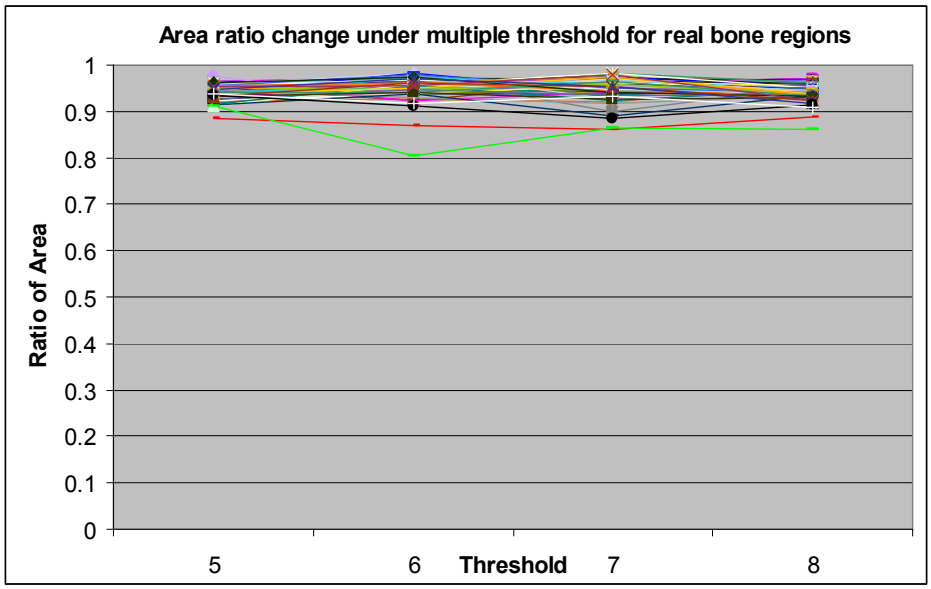


**Figure 43. Area ratio change with the change of threshold for real bone fragments (Each line represents one bone fragment)**

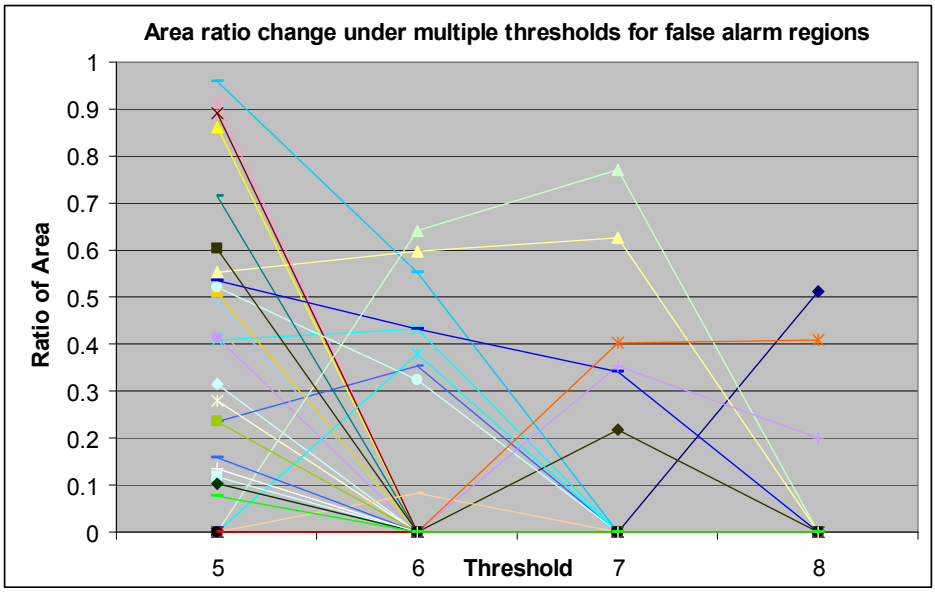


**Figure 44. Area ratio change with the change of threshold for false alarms (Each line represents one false alarm)**

According to above facts, the dynamic thresholding, which evaluates the response of combined image under a set of consecutive threshold values, was developed during this study, and showed great improvement in the performance compared to the original single threshold method. The related statistics are shown in Figure 45 and 46 to show the value of dynamic thresholding method.

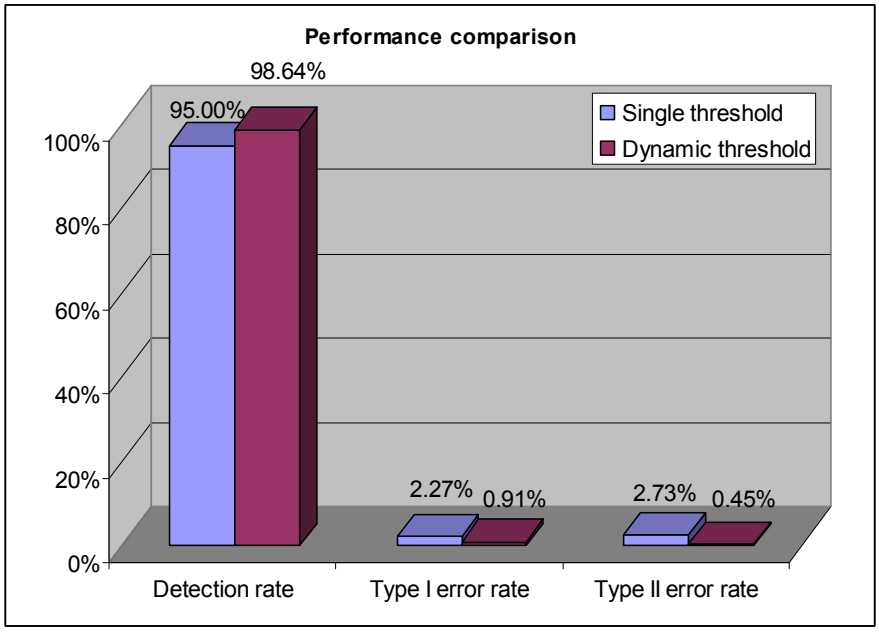


**Figure 45. Overall performance comparison between original single threshold and dynamic thresholding approaches**

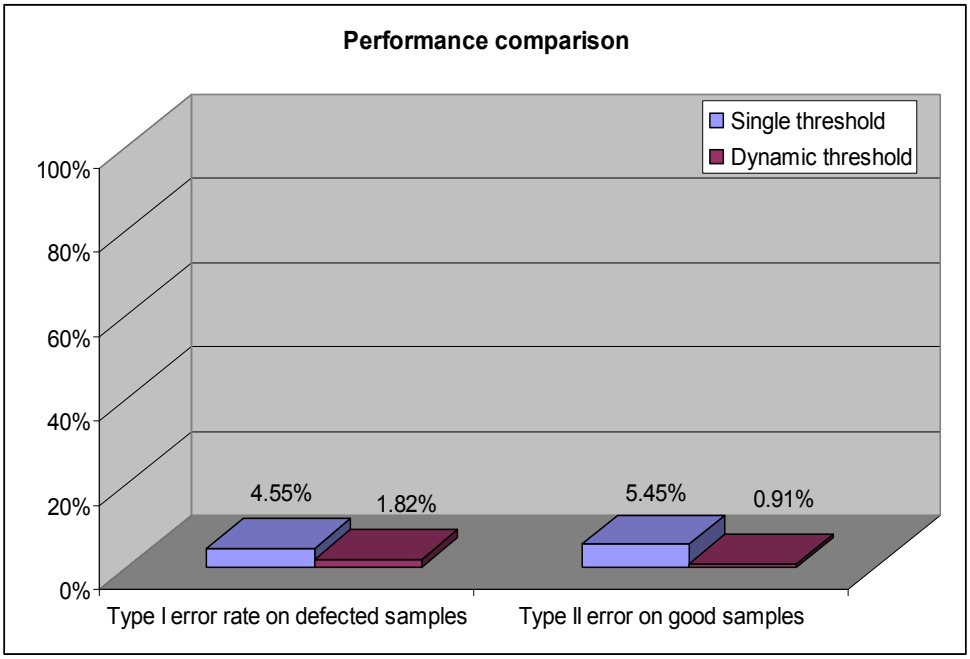


**Figure 46. Performance comparison based on two test criterions between original single threshold and dynamic thresholding approaches**

The overall comparison is illustrated in Figure 45. The proposed dynamic thresholding method has higher overall detection rate (98.64%) than the single threshold approach (95.00%). In addition, both type I and type II error of the proposed method are much lower than the original one. To further evaluate the dynamic thresholding method, Type I error on only defected 110 samples as well as Type II error on only good 110 samples are also analyzed and shown in Figure 46. The proposed method appears to be better than the original single threshold approach in both test criterions.

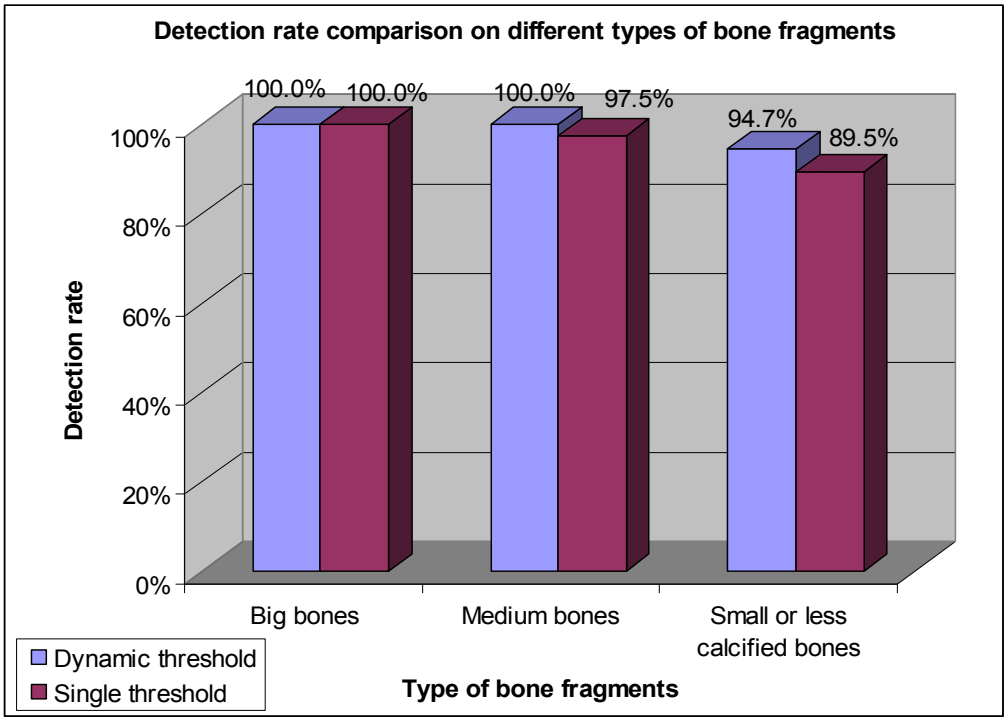


**Figure 47. Detection rate comparison based on different bone fragments categories**

A detailed statistical analysis based on three bone fragment categories was also conducted. The results are shown in Figure 47. Both proposed and original methods have perfect detection rate on large size bone fragments. However, the performance of the single threshold method drops significantly when the bone size becomes smaller and smaller. This is expected because small size bone fragments make the single threshold approach more vulnerable to the noise, and hence cause either miss-classification or false alarm. On the contrary, the dynamic thresholding approach considers responses in the region of interest under a set of thresholds, and has better noise resistance compared to the single threshold method. All the statistics above show the improvement of dynamic thresholding method in the chicken bone fragments detection compared to the original single threshold method. The dynamic

thresholding approach was fully integrated into the combined X-ray and Laser imaging system. The overall processing time of the system is 30 cm/sec.

## *6.4 Conclusions*

An improved Laser 3D range imaging sub-system was developed to recover the 3D depth information for the X-ray image compensation. Several important issues were addressed such as laser profile extraction, data flow design, memory management, parallel-programming. The original experimental Laser 3D imaging system was also extended to a two-lane, four-camera system, which doubled the system processing capacity. The overall improvement could be seen in both image resolution and computation time. On the X-ray imaging part, a novel dynamic thresholding approach was introduced to overcome the disadvantages of original single threshold method. Because of noise and error encountered during data calibration, 3D reconstruction and system integration, using a single threshold might not be sufficient to identify bones while suppressing the noise at the same time. The dynamic thresholding method utilizes more information under a set of consecutive thresholds. By checking the size change of suspicious regions under each threshold value, a better overall detection rate was achieved (98.64%) compared to the single threshold approach (95.00%). This showed the effectiveness of the proposed dynamic thresholding algorithm.

# CHAPTER 7 CONCLUSIONS AND FUTURE STUDY

In this dissertation, statistical pattern recognition approaches as well as 3D machine vision technologies for food quality and safety inspection have been explored. This research mainly focused on apple and poultry products since both of them are popular foods in the US.

In the automated apple defects detection, Gabor-wavelet based kernel principal component analysis approach was introduced. This approach freed the need of local feature segmentation by using Gabor feature decomposition for the whole apple NIR images. Given extracted global Gabor features, a high-dimensional space was obtained through the polynomial kernel function. Once apple Gabor features were mapped into this hyper-space, the PCA method could be used to linearly separate defective and good apple samples. An overall 90.6% detection rate was achieved using the proposed method.

For the automated apple stem-end/calyx identification, a novel 3D data enhancement/analysis approach was developed. Unlike traditional approaches, the proposed 3D based method took advantage of the full image information. Every pixel value contributed to the reconstructed 3D map, which meant a more detailed 3D description was obtained. For proposed methods, there was no additional light source required in the system: normal visible white light plus a NIR filter was enough. Given successfully recovered 3D depth data, two 3D processing approaches were presented

to identify the apple stem-end/calyx based on their unique 3D properties. Both algorithms were stem-end/calyx position independent, which made them suitable for different apple orientations. They were also robust to noisy data caused by alternate scanning of the camera, and even incomplete data. An overall detection rates above 90% were achieved by both methods.

For the automated chicken bone fragments detection, an improved Laser 3D range imaging sub-system was developed. Overall system throughput, accuracy and processing speed have been improved with the contribution of the Laser 3D imaging sub-system. To further improve detection performance while suppressing the noise, a novel dynamic thresholding approach was introduced. This method utilized more information from a set of consecutive thresholds by checking the size change of suspicious regions under each threshold value. A better overall detection rate was achieved (98.64%) compared to the single threshold approach (95.00%).

Future research can be conducted in the following areas:

1). Global features other than decomposed Gabor-wavelet can be explored for the apple defects classification;

2). More complex surface models can be studied in order to further improve the apple 3D surface reconstruction;

3). Apple defects and stem-end/calyx analysis can be extended to other similar fruits such as tomatoes, pears, etc.;

4). Real laser reflectance and scattering pattern on the bio-material surface can be studied to further improve the accuracy of 3D range imaging;

5). Real X-ray penetration pattern on the bio-materials can be explored to further improve the accuracy of 3D range imaging;

6). The noise model of entire fused X-ray/Laser imaging system can be studied in order to further improve the signal to noise ratio.

# PUBLICATIONS DURING THE PH. D. STUDY


[1] **Zhu, B.**, L. Jiang, and Y. Tao. 3D Shape Enhanced Transform for Automatic Apple Stem-End/Calyx Identification. Optical Engineering. Vol. 46(1):017201, 2007.

[2] **Zhu, B.**, L. Jiang, Y. Luo, and Y. Tao. Gabor Feature-Based Apple Quality Inspection Using Kernel Principal Component Analysis. J. of Food Engineering. Vol. 81(4):741-749, 2007.

[3] **Zhu, B.**, L. Jiang, F. Jin, L. Qin, and Y. Tao. ICA-kNN based Optimal Wavelength Selection and Walnuts Shell and Meat Differentiation under Fluorescence Hyperspectral Imagery. Sensing and Instrumentation for Food Quality and Safety. Vol. 1:123-131, 2007.

[4] **Zhu, B.**, L. Jiang, Y. Luo, Y. Tao, and X. Cheng. 3D Surface Reconstruction and Analysis in Automated Apple Stem-end/Calyx Identification. Trans. of ASABE. 2008 (Under revision).

[5] **Zhu, B.**, L. Jiang, X. Cheng, and Y. Tao. 3D surface reconstruction of apples from 2D NIR images. Proc. SPIE Optical East, Boston, Oct. 2005.

[6] **Zhu, B.**, L. Jiang, and Y. Tao. 3D Surface Reconstruction and Analysis of apple Near-Infrared data for the application of apple stem-end/calyx identification. ASABE 2007 Annual Meeting, Minnesota, Jun. 2007.

[7] Jiang, L., **B. Zhu**, X. Rao, G. Berney, and Y. Tao. Discrimination of Black Walnut Shell and Pulp in Hyperspectra1 Fluorescence Imagery using Gaussian Kernel Function Approach. J. of Food Engineering. Vol. 81(1): 108-117, 2007.

[8] Jiang, L., **B. Zhu**, H. Jing, X. Chen, X. Rao, and Y. Tao. Gaussian Mixture Model Based Walnut Shell and Meat Classification in Hyperspectral Fluorescence Imagery. Trans. of ASABE. Vol.50 (1): 153-160, 2007.

[9] Jin, F., L. Qin, L. Jiang**, B. Zhu**, and Y. Tao. Novel separation method of black walnut meat from shell using invariant features and a supervised self-organizing map. J. of Food Engineering, Vol. 88 (1): 75-85, 2008.

# BIBLIOGRAPHY


Aleixos, N., J. Blasco, F. Navarrón, and E. Moltó. 2002. Multispectral inspection of citrus in real-time using machine vision and digital signal processors. *Computers and Electronics in Agriculture*. 32(2): 121-137.

Alonso, M., L. Palou, M. Á. del Río, and J.-A. Jacas. 2007. Effect of X-ray irradiation on fruit quality of clementine mandarin cv. "Clemenules". *Radiation Physics and Chemistry* 76(10): 1631-1635.

Ariana, D., D. E. Guyer, and B. Shrestha. 2006. Integrating multispectral reflectance and fluorescence imaging for defect detection on apples. *Comput. Electron. Agric.* 50: 148-161.

Ávila, M. M., M. L. Durán, T. Antequera, R. Palacios, and M. Luquero. 2007. 3D Reconstruction on MRI to Analyse Marbling and Fat Level in Iberian Loin. *Lecture Notes in Computer Science* 4477: 145-152.

Baker, Gregory A. 1999. Consumer Preferences for Food Safety Attribute in Fresh Apples: Market Segments, Consumer Characteristics, and Marketing Opportunities. *Journal of Agricultural and Resource Economics* 21(1): 80-97.

Barton, F. E. 2002. Theory and principles of near infrared spectroscopy. *Spectroscopy Europe* 14(1): 12-18.

Belhumeur, P., J. Hespanha, and D. Kriegman. 1997. Eigenfaces vs. Fisherfaces: Recognition Using Class Specific Linear Projection. *IEEE Transactions on PAMI*. 19: 711-720.

Bennedsen, B. S., D. L. Peterson, and A. Tabb. 2005. Identifying defects in images of rotating apples. *Comput. Electron. Agric.* 48: 92-102.

Besl, P. J. and R. C. Jain. 1985. Three-dimensional object recognition. *ACM Computing Surveys (CSUR)* 17(1): 75-145.

Besl, P. J. and R. C. Jain. 1988. Segmentation through variable-order surface fitting. *IEEE Trans. PAMI.* 10(2): 167-192.

Blane, M. M., Z. Lei, H. Civi, and D. B. Cooper. 2000. The 3L Algorithm for Fitting Implicit Polynomial Curves and Surfaces to Data. *IEEE Trans. PAMI.* 22(3): 298-313.

Brown, G. K., L. J. Segerlind, and R. Summit. 1974. Near-infrared reflectance of bruised apples. *Trans. ASAE* 17(1): 17-19.

Cadavid, S. and M. Abdel-Mottaleb. 2007. Human Identification Based On 3d Ear Models. *First IEEE International Conference on Biometrics: Theory, Applications, and Systems, 2007.* Washington DC.

CDC (U. S. Centers for Disease Control and Prevention). 2008. Food-Related Diseases. [On-line]. Available: WWW: Http://www.cdc.gov/ncidod/diseases/food/

Chao, K., Y. R. Chen, and D. E. Chan. 2003. Analysis of Vis/NIR spectral variations of wholesome, septicemia, and cadaver chicken samples. *Applied Engineering in Agriculture.* 19(4): 453-458.

Chen, X. 2003. Detection of physical hazards in boneless poultry product using combined x-ray and laser range imaging technologies. *Ph. D. Thesis* University of Maryland, College Park.

Chen, X., H. Jing, Y. Tao, and X. Cheng. 2008. Real-Time Image Analysis for Nondestructive Detection of Metal Slivers in Packed Food. *Trans. ASAE.* 51(1): 303-309.

Chen, X., H. Jing, Y. Tao, L. Carr, and F. Wheaton. 2003. Real-Time Detection of Physical Hazards in De-Bonded Poultry Using High-Resolution X-Ray Imaging. *Paper number 033084*. 2003 ASAE Annual Meeting.

Cheng, X. 2004. Hyperspectral Imaging and Pattern Recognition Technologies for Real Time Fruit Safety and Quality Inspection. *Ph.D. Thesis* University of Maryland, College Park.

Cheng, X., Y. Chen, Y. Tao, C. Wang, M. Kim, and A. Lefcourt. 2004. A Novel Integrated PCA and FLD Method on Hyperspectral Image Feature Extraction for Cucumber Chilling Damage Inspection. *Trans. ASAE* 47(4): 1313-1320.

Cheng, X., Y. Tao, and Y. R. Chen. 2003. NIR/MIR dual-sensor machine vision system for on-line apple stem-end/calyx recognition. *Trans. ASAE*. 46(2): 551-558.

Corner, B., R. Narayanan, and S. Reichenbach. 1999. Principal component analysis of multisensor remote sensing imagery: Effects of additive and multiplicative noise. *Proc. SPIE 44th Annual Meeting* 3808: 183-191. Denver, Colorado.

Cortes, C. and V. Vapnik. 1995. Support vector networks. *Machine Learning* 20: 273-297.

Crouzil, A., X. Descombes, and J-D. Durou. 2003. A Multiresolution Approach for Shape from Shading Coupling Deterministic and Stochastic Optimization. *IEEE Transactions on PAMI.* 25(11): 1416-1421.

Daley, W., D. Britton, C. Usher, M. Diao, and K. Ruffin. 2005. 3D sensing for machine guidance in meat cutting applications. *Proc. SPIE* 5996: 59960D.

Duda, R., P. Hart, and D. Stork. 2001. *Pattern Classification* (2nd ed.). Wiley Interscience.

Franck, J. 1926. Elementary processes of photochemical reactions. *Transactions of the Faraday Society* 21: 536-542.

Gabor wavelet. 2008. [On-line]. Available: WWW: http://www.brains-minds-media.org/archive/290

Gleason, S.S., M.J. Paulus, and J.A. Mullens. 2002. Automatic detection of bone fragments in poultry using multi-energy x-rays. U.S. Patent No. 6370223.

Good Fruit Growers. 1993. MERLIN electronic color sorter. 3/15.

Guo, G., S. Z. Li, and K. Chan. 2000. Face Recognition by support vector machines. *Proc. 4th IEEE International Conference on Automatic Face and Gesture Recognition* 196-201. Grenoble, France.

Haff, R. P. and D. C. Slaughter. 2004. Real-Time X-Ray Inspection of Wheat for Infestation by the Granary Weevil, Sitophilus granarius (L.). *Trans. ASAE.* 47(2): 531-537.

Haralick, R. M. 1983. Ridges and valleys on digital images. *Comput. Vision Graph. Image Processing* 22: 28-38.

Haralick, R. M. 1984. Digital step edges from zero crossing of second directional derivatives. *IEEE Trans. PAMI.* 6(1): 58-68.

Haralick, R. M. and L. Watson. 1981. A facet model for image data. *Comput. Graphics Image Processing* 15: 113-129.

Hartman, L. R. 2001. X-ray inspection boosts confidence through the pipeline. *Packaging digest* 2001:54.

Hayes, Dermot J., Jason Shogren, Seung Youll Shin, and James Kliebenstein. 1995. Valuing Food Safety in Experimental Auction Markets. *American Journal of Agricultural Economics* 77(1): 40-53.

Haykin, S. 1999. *Neural Networks – A Comprehensive Foundation* (2nd ed.). Prentice Hall.

Hebert, M., K. Ikeuchi, and H. Delingette. 1995. A spherical representation for recognition of free-form surfaces. *IEEE Trans. PAMI.* 17(7): 681-690.

Herschel, F. W. 1800. *Phil. Trans. Roy. Soc.* (London) 90: 255.

Horn, B. K. P. 1970. Shape from shading: A method for obtaining the shape of a smooth opaque object from one view. *PhD thesis* Massachusetts Inst. of Technology, MA.

Ji, Q. and R. M. Haralick. 2002. Efficient facet edge detection and quantitative performance evaluation. *Pattern Recognition* 35: 689-700.

Jiang, H., R. A. Robb, H. Tainter, and S. Kerrie. 1992. New approach to 3-D registration of multimodality medical images by surface matching. *Proc. SPIE 1808* 196-213.

Jiang, J.-A., H.-Y. Chang, K.-H. Wu, C.-S. Ouyang, M.-M. Yang, E.-C. Yang, T.-W. Chen, and T.-T. Lin. 2008. An adaptive image segmentation algorithm for X-ray quarantine inspection of selected fruits. *Computers and Electronics in Agriculture* 60(2): 190-200.

Jiménez, A. R., R. Ceres, and J.L. Pons. 2000. A vision system based on a laser range-finder applied to robotic fruit harvesting. *Machine Vision and Applications* 11(6): 321-329.

Jing, H. 2003. Dynamic 3-D Laser Range Imaging for Poultry Products. *Ph. D. Thesis* University of Maryland, College Park.

Jing, H., X. Chen, and Y. Tao. 2003. Geometrical Calibration and Integration of Laser 3D and X-ray Dual Systems. *Paper number 033085*. 2003 ASAE Annual Meeting.

Jing, H., X. Chen, Y. Tao, B. Zhu, and F. Jin. 2005. Sub-Pixel Accuracy Thickness Calculation of Poultry Fillets from Scattered Laser Profiles. *Proc. SPIE 6000* 188-196.

Jones, J. P. and L. A. Palmer. 1987. An Evaluation of the Two-Dimensional Gabor Filter Model of Simple Receptive Fields in Cat Striate Cortex. *J. Neurophysiol.* 58: 1233-1258.

Kawasaki, M., S. Kawamura, M. Tsukahara, S. Morita, M. Komiya, and M. Natsuga. 2008. Near-infrared spectroscopic sensing system for on-line milk quality assessment in a milking robot. *Computers and Electronics in Agriculture*. 63(1): 22-27.

Kimmel, R. and J. A. Sethian. 2001. Optimal Algorithm for Shape from Shading and Path Planning. *Journal of Mathematical Imaging and Vision* 14(3): 237-244.

Koch, J. and A. G. Fowler. 1998. Bone detector. U. S. Patent No. 5847382.

Kotwaliwale, N., J. Subbiah, P. R. Weckler, G. H. Brusewitz, and G. A. Kranzler. 2007. Calibration of a Soft X-Ray Digital Imaging System for Biological Materials. *Trans. ASABE* 50(2): 661-666.

Kröger, C., C.M. Bartle, J.G. West, R.W. Purchas, and C.E. Devine. 2006. Meat tenderness evaluation using dual energy X-ray absorptiometry (DEXA). *Computers and Electronics in Agriculture* 54(2): 93-100.

Kumar, P. A. and S. Bal. 2007. Automatic Unhulled Rice Grain Crack Detection by X-Ray Imaging. *Trans. ASAE.* 50(5): 1907-1911.

Lades, M., J. C. Vorbruggen, J. Buhmann, J. Lange, C. von der Malsburg, R. P. Wurtz, and W. Konen. 1993. Distortion Invariant Object Recognition in the Dynamic Link Architecture. *IEEE Trans. on Computers* 42(3): 300-311.

Lammertyn, J., T. Dresselaers, P. V. Hecke, P. Jancsók, M. Wevers, and B. M. Nicolaï. 2003. Analysis of the time course of core breakdown in "Conference" pears by means of MRI and X-ray CT. *Postharvest Biology and Technology* 29(1): 19-28.

Leemans, V., H. Magein, and M. –F. Destain. 1999. Defect segmentation on "Jonagold" apples using color vision and a Bayesian classification method. *Comput. Electron. Agric.* 23: 43-53.

Leemans, V., H. Magein, and M. –F. Destain. 2002. On-line Fruit Grading according to their External Quality using Machine Vision. *Biosystems Engineering* 83: 397-404.

Li, Q., M. Wang, and W. Gu. 2002. Computer vision based system for apple surface defect detection. *Comput. Electron. Agric.* 36: 215-223.

Lim, K. S. and M. Barigou. 2004. X-ray micro-computed tomography of cellular food products. *Food Research International* 37(10): 1001-1012.

Lin, M., A. G. Cavinato, Y. Huang, and B. A. Rasco. 2003. Predicting sodium chloride content in commercial king (Oncorhynchus tshawytscha) and chum (O. keta) hot smoked salmon fillet portions by short-wavelength near-infrared (SW-NIR) spectroscopy. *Food Research International*. 36(8): 761-766.

Lin, Ta-Te, Hsiang-Yun Chang, Ke-Han Wu, Joe-Air Jiang, and Cheng-Shiou Ouyang. 2005. An Adaptive Image Segmentation Algorithm for X-Ray Quarantine Inspection of Selected Fruits. *Paper number 053123*. 2005 ASAE Annual Meeting.

Liu, C. 2004. Gabor-Based Kernel PCA with Fractional Power Polynomial Models for Face Recognition. *IEEE Trans. on PAMI* 26: 572-581.

Liu, C. and H. Wechsler. 2002. Gabor Feature Based Classification Using the Enhanced Fisher Linear Discriminant Model for Face Recognition. *IEEE Trans. on Image Processing* 11(4): 467-476.

Lu, R. 2001. Predicting firmness and sugar content of sweet cherries using near-infrared diffuse reflectance spectroscopy. *Trans. ASAE*. 44(5): 1265-1271.

Lu, R. 2003. Detection of bruises on apples using near-infrared hyperspectral imaging. *Trans. ASAE* 46(2): 523-530.

Lukács, G., R. Martin, and D. Marshall. 1998. Faithful Least-Squares Fitting of Spheres, Cylinders, Cones and Tori for Reliable Segmentation. *Lecture Notes in Computer Science* 1406: 671.

Lyman, O. 2001. *An Introduction to Statistical Methods and Data Analysis* (5th ed.). Michael Longnecker.

McFarlane, N. J. B., R. D. Speller, C. R. Bull, and R. D. Tillett. 2003. Detection of Bone Fragments in Chicken Meat using X-ray Backscatter. *Biosystems Engineering* 85(2): 185-199.

Moore, Gordon E. 1965. Cramming more components onto integrated circuits. *Electronics* 38(8).

Müller, W. D., I. Dederer, and S. J. Linn. 2005. Use of X-ray technology for the determination of fat content by meat sorting. *Fleischwirtschaft* 85(3): 128-131.

Nagata, M., J. G. Tallada, and T. Kobayashi. 2006. Bruise Detection using NIR Hyperspectral Imaging for Strawberry (Fragaria *x* ananassa Duch.). *Environment Control in Biology*. 44(2): 133-142.

Nakano, K. 1997. Application of Neural Networks to the Color Grading of Apples. *Comput. Electron. Agric*. 18: 105-116.

National Electrical Manufacturers Association (NEMA). 2008. Enclosures for Electrical Equipment. [On-line]. Available: WWW: http://www.nema.org/stds/250.cfm

Neethirajan, S., D.S. Jayas, and N.D.G. White. 2007. Detection of sprouted wheat kernels using soft X-ray image analysis. *Journal of Food Engineering* 81(3): 509-513.

Norris, K. H. 1964. Simple spectroradiometer for 0.4-1.2 micron region. *Trans. ASAE.* 7: 240-242.

Ogawa, Y., K. Morita, S. Tanaka, M. Setoguchi, and C. N. Thai. 1998. Application of X-Ray CT for Detection of Physical Foreign Materials in Foods. *Trans. ASAE* 41(1): 157-162.

Osuna, E., R. Freund, and F. Girosi. 1997. Training Support Vector Machines: an Application to Face Detection. *Proc. of CVPR'97*. Puerto Rico.

Park, B., Y. R. Chen, W. R. Hruschka, S. D. Shackelford, and M. Koohmaraie. 2001. Principal component regression of near–infrared reflectance spectra for beef tenderness prediction. *Trans. ASAE.* 44(3): 609-615.

Park, T. S., Y. M. Bae, H. S. Seo, T. J. Park, K. H. Seol, D. K. Lim, M. Lee, and S. I. Cho. 2008. Evaluation of Pork Loin Freshness Using Absorbance Characteristic of Near-Infrared. *Trans. ASAE.* 1(2): 173-180.

Pearson, K. 1901. On Lines and Planes of Closest Fit to Systems of Points in Space. *Philosophical Magazine* 2(6): 559-572.

Pedroa, A. M. K. and M. M.C. Ferreira. 2007. Simultaneously calibrating solids, sugars and acidity of tomato products using PLS2 and NIR spectroscopy. *Analytica Chimica Acta*. 595(1-2): 221-227.

Penman, D. W. 2001. Determination of stem and calyx location on apples using automatic visual inspection. *Comput. Electron. Agric.* 33: 7-18.

Pentland, A. P. 1982. Finding the illuminant direction. *J. Opt. Soc. Amer. A* 72(4): 448-455.

Pentland, A. P. 1989. Shape information from shading: A theory about human perception. *Spatial Vision* 4(2/3): 165-182.

Plunkett Research, Ltd. 2007. Food Industry Overview. [On-line]. Available: WWW: http://www.plunkettresearch.com/Industries/FoodBeverageTobacco/FoodBeverageTobaccoStatistics/tabid/248/Default.aspx

Pournaras, A. V., M. I. Prodromidis, A. P. Katsoulidis, A. V. Badeka, D. Georgantelis, and M. G. Kontominas. 2008. Evaluation of lacquered tinplated cans containing octopus in brine by employing X-ray microanalysis and electrochemical impedance spectroscopy. *Journal of Food Engineering* 86(3): 460-464.

Prados, E. and O. Faugeras. 2003. "Perspective shape from shading" and viscosity solutions. *Proceedings of Ninth IEEE International Conference on Computer Vision* 2: 826-831.

Prados, E., O. Faugeras, and E. Rouy. 2002. Shape from Shading and Viscosity Solutions. *Proceedings of European Conference on Computer Vision* 2: 790-804.

Prieto, N., S. Andrés, F.J. Giráldez, A.R. Mantecón, and P. Lavín. 2008. Discrimination of adult steers (oxen) and young cattle ground meat samples by near infrared reflectance spectroscopy (NIRS). *Meat Science*. 79(1): 198-201.

Sarker, N., and R. R. Wolfe. 1985. Computer vision based system for quality separation of fresh market tomatoes. *Trans. ASAE* 28(5): 1714-1718.

Schölkopf, B., A. Smola, and K. Müller. 1998. Nonlinear Component Analysis as a Kernel Eigenvalue Problem. *Neural Computation* 10: 1299-1319.

Scott, A. M., H. Macapinlac, J. Zhang, F. Daghighian, N. Montemayor, H. Kalaigian, G. Sgouros, M. C. Graham, K. Kolbert, S. D.J. Yeh, E. Lai, S. J. Goldsmith, and

S. M. Larson. 1995. Image Registration of SPECT and CT Images Using an External Fiduciary Band and Three-Dimensional Surface Fitting in Metastatic Thyroid Cancer. *The Journal of Nuclear Medicine* 36(1): 100-103.

Shahin, M. A., E. W. Tollner, R. W. McClendon, and H. R. Arabnia. 2002. Apple Classification Based on Surface Bruises Using Image Processing and Neural Networks. *Trans. ASAE* 45(5): 1619-1627.

Shawe-Taylor, J. and N. Cristianini. 2004. *Kernel Methods for Pattern Analysis*. Cambridge University Press.

Shen, L. and L. Bai. 2004. Gabor Feature Based Face Recognition Using Kernel Methods. *6th IEEE International Conference on Automatic Face and Gesture Recognition* 170-176. Seoul, Korea.

Sivakumar, M., M. Annamalai, D. S. Jayas, J. Paliwal, and N. D.G. White. 2007. Near-Infrared Hyperspectral Imaging to Differentiate Wheat Classes. *ASABE Paper No: 072835*. Minneapolis, MN: ASABE annual meeting.

Tankus, A., N. Sochen, and Y. Yeshurun. 2004. Perspective Shape-from-Shading by Fast Marching. *Proceedings of Computer Vision and Pattern Recognition'04*.

Tao, Y. 1996. Spherical transform of fruit images for on-line defect extraction of mass objects. *Opt. Eng.* 35(2): 344-350.

Tao, Y., and J. G. Ibarra. 2000. Thickness-compensated X-ray imaging detection of bone fragments in deboned poultry-model analysis. *Trans ASAE* 43(2): 453-459.

Tao, Y., and Z. Wen. 1999. An adaptive spherical image transform for high-speed fruit defect detection. *Trans. ASAE* 42(1): 241-246.

Tao, Y., L. Chance, and B. Liu. 1995. Full-scale fruit vision sorting system design – factors and considerations. *In Food Processing Automation IV*. ASAE Publication.

Tao, Y., Z. Chen, H. Jing, and J. Walker. 2001. Internal Inspection of Deboned Poultry Using X–Ray Imaging and Adaptive Thresholding. *Trans. ASAE* 44(4): 1005-1009.

Throop, J. A., D. J. Aneshansley, and B. Anger. 1999. Multispectral images for detecting defects on apples in real time. *ASAE Paper No.993205*. St. Joseph, Mich.: ASAE.

Throop, J. A., D. J. Aneshansley, B. L. Upchurch, and B. Anger. 2001. Apple orientation on two conveyors: performance and predictability based on fruit shape characteristics. *Trans. ASAE* 44(1): 99-109.

Throop, J. A., D. J. Aneshansley, B. L. Upchurch, and B. Anger. 2001. Apple orientation on two conveyors: performance and predictability based on fruit shape characteristics. *Trans. ASAE* 44(1): 99-109.

Turk, M. and A. Pentland. 1991. Eigenfaces for Recognition. *J. Cognitive Neuroscience* 3: 72-86.

Unay, D., and B. Gosselin. 2003. A Study on Quality Grading of Jonagold Apples. *Proc. of the 3rd IEEE International Symposium on Signal Processing and Information Technology (IEEE ISSPIT 2003)*. Germany.

Unay, D., and B. Gosselin. 2004. An approach for recognizing stem-end/calyx regions in apple quality sorting. *ACIVS 2004 Conference*. Brussels, Belgium.

Unay, D., and B. Gosselin. 2005. Artificial Neural Network-based Segmentation and Apple Grading by Machine Vision. *Proc. of IEEE ICIP 2005*. Italy.

USDA (U. S. Department of Agriculture). 2007a. National Agricultural Statistics Service. [On-line]. Available: WWW: http://usda.mannlib.cornell.edu/usda/current/CropProd/CropProd-08-10-2007.pdf

USDA. 2002. Profiling Food Consumption in America. [On-line]. Available: WWW: http://www.usda.gov/factbook/chapter2.htm

USDA. 2007b. National Agricultural Statistics Service. [On-line]. Available: WWW: http://usda.mannlib.cornell.edu/usda/current/PoulProdVa/PoulProdVa-04-27-2007_revision.pdf

Wen, Z., and Y. Tao. 1998. Fuzzy-based determination of model and parameters of dual-wavelength vision system for on-line apple sorting. *Opt. Eng.* 37(1): 293-299.

Wen, Z., and Y. Tao. 1999. Building a rule-based machine-vision system for defect inspection on apple sorting and packing lines. *Expert Sys. Appl.* 16: 307-313.

Wen, Z., and Y. Tao. 2000. Dual-camera NIR/MIR imaging for stem-end/calyx identification in apple defect sorting. *Trans. ASAE* 43(2): 449-452.

Wheatstone, C. 1838. Contributions to the Physiology of Vision. -Part the First. On some remarkable, and hitherto unobserved, Phenomena of Binocular Vision. [On-line]. Available: WWW: http://www.stereoscopy.com/library/wheatstone-paper1838.html

WHO (World Health Organization). 2008. Food safety. [On-line]. Available: WWW: http://www.who.int/foodsafety/en/

Wikipedia. 2008a. Franck-Condon principle. [On-line]. Available: WWW: http://en.wikipedia.org/wiki/Franck-Condon_principle

Wikipedia. 2008b. Near infrared spectroscopy. [On-line]. Available: WWW: http://en.wikipedia.org/wiki/Near_infrared_spectroscopy

Wikipedia. 2008c. Wilhelm Conrad Röntgen. [On-line]. Available: WWW: http://en.wikipedia.org/wiki/Wilhelm_Conrad_R%C3%B6ntgen

Wikipedia. 2008d. X-ray tube. [On-line]. Available: WWW: http://en.wikipedia.org/wiki/X-ray_tube

Wikipedia. 2008e. X-ray. [On-line]. Available: WWW: http://en.wikipedia.org/wiki/X-ray

Wikipedia. 2008f. Structure from motion. [On-line]. Available: WWW: http://en.wikipedia.org/wiki/Structure_from_motion

Wikipedia. 2008g. IP Code. [On-line]. Available: WWW: http://en.wikipedia.org/wiki/IP_Code

Windham, W. R., K. C. Lawrence, B. Park, and R. J. Buhr. 2003. Visible/NIR spectroscopy for characterizing fecal contamination of chicken carcasses. *Trans. ASAE*. 46(3): 747-751.

Woock, P., F. Pagel, M. Grinberg, D. Willersinn. 2007. Odometry-Based Structure from Motion. *Proceedings of the 2007 IEEE Intelligent Vehicles Symposium* 1112-1117.

Wu, Q., J. Ben-Arie. 2007. Hybrid PCA based Shape from Shading for 3D Head Reconstruction. *IEEE Electro/Information Technology 2007 Proceedings*. 407-411.

Wyngaerd, J. V. and L. V. Gool. 2002. Coarse Registration of Surface Patches with Local Symmetries. *Lecture Notes in Computer Science* 2351: 572.

Yang, Q. 1996. Apple stem and calyx identification with machine vision. *J. Agric. Engng Res.* 63: 229-236.

Yang, Q., and J. A. Marchant. 1996. Accurate blemish detection with active contour models. *Comput. Electron. Agric.* 14: 77-89.

Yoon, S. C., K. C. Lawrence, D. P. Smith, B. Park, and W. R. Windham. 2006. Bone Fragment Detection in Chicken Breast Fillets using Back-Illuminated Structured Light. *Paper number 063017.* 2006 ASAE Annual Meeting.

Zhang, R., P. –S. Tsai, J. E. Cryer, and M. Shah. 1999. Shape from shading: A survey. *IEEE Trans. PAMI.* 21(8): 690-706.

Zion, B., P. Chen, and M. J. McCarthy. 1995. Detection of bruises in magnetic resonance images of apples. *Comput. Electron. Agric.* 13: 289-299.